BROAD-BAND AND SCALABLE CIRCUIT-LEVEL MODEL OF MSM PD FOR CO-DESIGN WITH PREAMPLIFIER IN FRONT-END RECEIVER APPLICATIONS

A Dissertation
Presented to
The Academic Faculty

By

Cheolung Cha

In Partial Fulfillment
Of the Requirements for the Degree
Doctor of Philosophy in
Electrical and Computer Engineering

Georgia Institute of Technology

March, 2004

DEDICATION

I would like to dedicate this work to my family and my fiancé
for their continuous love and belief in me.

ACKNOWLEDGEMENT

I would like to thank my thesis advisor, Dr. Martin A. Brooke, for his constant support, flexibility, flow of ideas, and patience during this research program. He has allowed me to explore new ideas, but has constantly helped me stay focused on the main objectives of the research work. His strong affiliations with other research groups have allowed me to interact with and gain insight from student members and faculty from those areas. I would especially like to thank Dr. Nan M. Jokerst, her group members, and my group members for their assistance in the use of high speed optic test equipment and device fabrications, which has been fundamental to the verification of this work. I also would like to thank Dr. William T. Rhodes, Dr. Gee-Kung Chang, Dr. Paul E. Hasler, and Dr. Paul A. Kohl for serving on my committees and their suggestions and criticisms of my work. Last but not least, I would like to thank my family and fiancé for their constant support and encouragement during this research program.

TABLE OF CONTENTS

LIST OF TABLES

LIST OF FIGURES

SUMMARY

An accurate and fast behavior modeling procedure is presented for codesign of active optical device with circuitry. The developed method is based upon defining partial elements (PEs) and their measurement-based partial element equivalent circuits (M-PEEC), associating design rules with them, and characterizing them through the use of test structures. The test structures are designed such that they can include only sensitive combinations of predefined building blocks, and they are measured over a wide band of frequencies using network analysis techniques. Measurement-based partial element equivalent circuits of the building blocks are derived from the measured s-parameters of the test structures by nonlinear optimization methods.

The method has been experimentally verified using metal-semiconductor-metal photodetectors. The method has also been verified with circuits using simulations, with good results obtained.

CHAPTER I

INTRODUCTION

The remarkable advances of the integrated circuit (IC) and fabrication technology have made it possible that on-chip frequencies are at the multi-GHz level in commercial products. However, due to the parasitic effects of electrical interconnect lines on the printed circuit board (PCB), off-chip and board-level signal speeds are still at a low aggregate data rates compared to on chip signaling. This is becoming a bottleneck to data flow in system designs and, the electronics industry is considering many solutions, one of which is optical interconnect at the board level. Historically applications of optoelectronics to data transport have been limited to long haul telecommunication, but optoelectronic technology has greatly evolved in the last two decades, penetrating all areas of modern telecommunication networks. Today's applications of optoelectronics are spreading to the backbone of metro networks and LAN networks, and even now to board-level interconnects.

As the speed of communications and interconnects increases, accurate simulation of the electromagnetic (EM) behavior of monolithically or hybrid integrated devices in chips and boards is becoming more and more important. For this purpose, accurate and fast device models are inevitable in device and circuit designing process. As a result, much research has been performed on modeling methodology. Device modeling process is important and provides a base for all modern circuit design. To efficiently utilize any

new fabrication technology for design work, good physical and behavior models of the various components involved are very important. In integrated circuit design, for example, good models for transistors are crucial for obtaining fabricated circuits that match design specifications. In the same manner, accurate, frequency-dependent, and wide band models of optical devices are also very important for successful high-speed optoelectronic integrated circuit (OEIC) design.

If a predictive electromagnetic model of an optoelectronic device can be formulated as an equivalent circuit with parameters that can be changed to reflect physical variations in the devices manufacture (such as area), then model this will facilitate the combined analysis and optimization of the optoelectronic device and an associated integrated circuit (such as a transimpedance amplifier). This codesign and cooptimization of the optoelectronic device and integrated circuit will enable circuit designers to achieve performance superior to that obtained when the integrated circuit is optimized independent of the optoelectronic device or with only one fixed device as is currently common practice.

In this research, the partial element equivalent circuit (PEEC) based models are the fundamental circuit-level representation used to model devices as equivalent circuits. Originally, the partial element equivalent circuit (PEEC) models came from Maxwell's electric field integral equation (EFIE)-based modeling method, which is a finite element electromagnetic full wave method [76].

In this thesis, several modeling methodologies are investigated and compared for use in codesign, and a novel hybrid predictive device modeling methodology is

introduced and applied to optical active device modeling through the use of a measurement-based partial element equivalent circuit (M-PEEC) models. The method is hybrid because, whereas scaleable partial element equivalent circuit (PEEC) based models (built from PEEC building blocks) were originally intended for numerically-based simulation methods, the new method uses measurements to set the parameters of the partial elements of the models. It will be demonstrated that the measurement-based modeling methodology overcomes the inaccuracy problems of both finite element and equation-based models (since all material properties and parasitic effects are automatically included in the measurements), and can overcome the slow simulation time of finite element (FE) methods (because much more compact models result from this approach).

Because it uses a scalable partial elements approach to construct the device models the new measurement-based modeling technique can be applied to arbitrary geometry structures, including multi-port devices. In addition since measurements automatically take into account processing effects such as non-uniform dielectric thickness, roughness in width and surface of conductors, processing fluctuations, and non-ideal material properties, the method is very accurate which is very difficult to achieve with any other methods. Users can also incorporate statistical information in the models by repeatedly fabricating test structures and extracting a statistically significant set of partial elements models [4-5]. The main limitation of this method is that it is not arbitrarily predictive, by this is meant that a modeling method can be used in designing the all the different dimensions of the device without limitations, as is promised with both

the equation and finite element-based methods. However, it is demonstrated that sufficient flexibility in device construction is possible to significantly enhance the ability of circuit designers to optimize the co-designed circuits.

Recently this type of modeling has been demonstrated for passive circuit devices (Resisters, Inductors and Capacitors). In this thesis the method used will be extended for the first time to active (optoelectronic) devices. The measurement-based modeling methodology will be developed and demonstrated experimentally to predict the behavior of different sized photodetectors at frequencies into the tens of GHz in the chapter VI.

1.1. Thesis Organization

In this dissertation, a measurement-based modeling method will be presented, with passive and active optical device modeling in detail. The first part (Chapter I, II, III, and IV) of this dissertation is dedicated to the modeling methodologies, especially, PEEC models, the proposed M-PEEC models, and the background of front-end of optical receiver. The second part (Chapter V) shows the fabrication of test structures, calibration methods, deembedding techniques, and measurements for the application of the proposed method to the predictive modeling of the active optical devices such as metal-semiconductor-metal photodetectors (MSM PDs). Detailed procedures and results are also shown in chapter VI. A brief chapter-by-chapter outline of the thesis is given below.

Chapter II discusses the background and origin of the problem on device modeling methods, and presents some of the major work already performed in this area.

Especially, the partial element equivalent circuit models are investigated and derived mathematically in this chapter. As will be seen, most of the work is originated from the microwave engineering arena. Chapter III presents M-PEEC models that are proposed and demonstrated through a case study. Chapter VI provides the background of the front-end of optical receiver, especially metal-semiconductor-metal photodetector and preamplifier. In this chapter, several simulation results and improved physical models are also presented. Chapter V covers a detailed description on the test structure fabrication, calibration methods, deembedding techniques, and measurements procedures. Chapter VI shows an application of the method to the modeling of active optical device such as metal-semiconductor-metal photodetectors, and detailed modeling procedures are also presented. The results are compared to measurements and verified up to multi-GHz frequency range. Chapter VII draws conclusions regarding this work and provides a summary. Several appendices are also included which document some measured data of the structures studied under this research work.

CHAPTER II

MODELING METHODOLOGY

2.1. Introduction

Modeling provides a base for electrical and optical simulation. Good models allow a device's parameters are varied, without having to fabricate actual devices every time to see if they will operate as desired. Thus, unlimited designs of devices and circuits can be performed using various modeling algorithms and optimized designs can be selected for actual fabrication and testing. However, only accurate models of components can guarantee successful design and fabrication high performance systems that utilize those devices.

The dimension shrinkage of individual active and passive components allows more components on a single die and board. This makes possible remarkable integration density increasing in chip and board-scale. This also causes cost-reduction and high-speed performance. However, as the feature size of devices reaches the nanometer-scale realm, the device behavior modeling becomes increasingly complicated and unexpected because of new physical phenomena such as quantum mechanical interference. As a result, the traditional and classical modeling methods can be partly used or cannot be used to predict the models. This chapter presents an overview of the different approaches

employed today for the development of an electromagnetic modeling and simulation framework that can effectively tackle the complexity of the device characterization and facilitate its design.

2.2. Modeling Methods

Device modeling techniques mainly fall into three categories that are shown in Fig. 2.1.1: analytical (physical equation-based), numerical (electromagnetic full wave-based), and empirical (measurement-based) methods. The same modeling methodologies can be applied to both the frequency and time domain.

Analytical modeling methods use fundamental physical principles to derive models. However, most analytical models resort to numerical simulation or tables to address complex geometrical structures. Typically as device speed increases the modeling of parasitic elements like fringing capacitance and RF coupling between parts of a device become important. These are notoriously difficult to model and often lead to accuracy problems at high frequency for analytical models. Consequently, analytical models tend to be best used as empirical models, when a specific device is measured and the unknown or difficult to predict parts of the model are fit to the specific device. This leads to a non-scalable device model that cannot predict accurately how the device works if it is changed dimensionally [90-92].

Empirical methods mainly depend on measurements. Network analysis is used for the frequency domain applications, and time domain reflectometry (TDR) and impulse

response measurements are taken to characterize the device under test (DUT) in the time domain analysis. In network analysis, scattering parameters are obtained over a wide band of frequencies, while for TDR and impulse response analysis a time domain voltage profile that is reflected or transmitted is obtained, with peaks, valleys, oscillations, and relaxations representing capacitive, inductive, resistive, and some combined discontinuities within the structure. Since measurements are in time domain, the relative position of the discontinuity can be determined using the propagation velocity in a material [4,74].

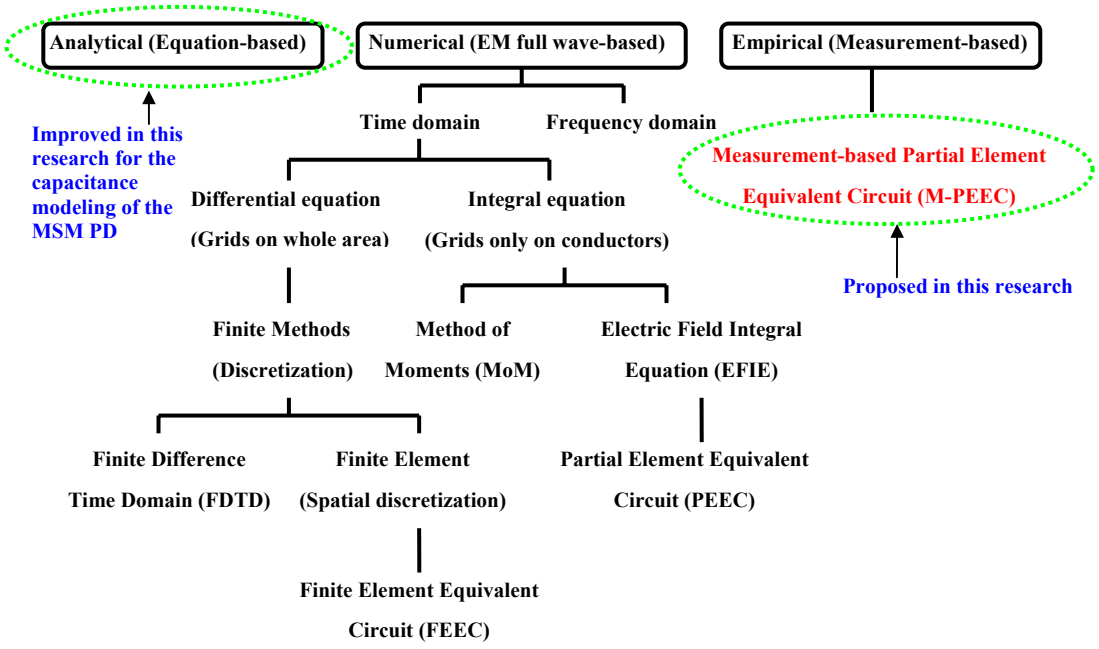

Figure 2.1.1 Modeling methodology tree

Measurement-based models have many advantages such that it can be applied to any arbitrary structure and it can takes into account unexpected processing effects, for

example, non-uniform dielectric thicknesses and uneven metal depositions, which would be very difficult to achieve with any other methods. However, measurement-based models are not predictive and scalable because DUT should be fabricated and measured at every time for each dimension of device.

Numerical modeling methods are mainly focused on electromagnetic full wave analysis by applying Maxwell's equations to an arbitrary geometry structure and computing electric and magnetic field patterns on the structure. These models are undoubtedly more scalable, predictive, and general than other modeling methods. The methods generally use segmenting and discretization on the structure into many small pieces, and solving Maxwell's equations on each piece and boundary to obtain the total solution of the whole structure. Memory resource and computation time of CPU are directly proportional to the number of grid cells and frequency points. There are several different numerical methods that have been used for EM full wave analysis in Fig. 2.2.1. The similar methods can be applied to a frequency domain analysis. However, the frequency domain finite element method requires the vector field calculation and this causes increment of the number of unknowns, thus EM full wave analysis is usually done in the time domain [75].

All EM full wave based modeling techniques can be categorized as either differential equation (DE) or integral equation (IE) based. There are two prevalent modeling methods in the finite methods (FM) of the differential equation based: the finite difference time domain (FDTD) and the finite element method (FEM) techniques. These methods are based on the direct discretization. The finite element uses the spatial

discretization, which results in a localized electromagnetic fields coupling between only a few local cells of the whole grid structures. The FEM uses interpolation functions of local support, which resulting in sparse FEM matrix, to represent electromagnetic fields. These local functions are nonzero only over a few elements in the FEM grid. The same functions are used as weighting functions for the testing of the functional in a Galerkin sense. While in the case of FDTD, Maxwell's equations are solved at each node of the whole grid cells. The utilization of a Cartesian grid for a discretization of the target structure makes the FDTD simple and effective. The discretization procedure results in a state-space equation of the discrete electromagnetic problem with state variables. The staggering unknowns are known as Yee lattice, which was originally introduced for the electromagnetic case by Yee [75, 76].

Compared to differential equation-based methods, which discretize the entire structure and solve for the electric and/or magnetic field everywhere, the matrices of integral equation-based are smaller in size and dense since integral equation-based models only apply discretization of the electric currents and charges in or on the conducting parts of the structure. Although integral equation-based methods have smaller size matrices, integral equation-based solutions are more expensive than those of differential equation-based because the integral equation-based matrices are dense. The integral equation-based models consider partial and global coupling, however DE-based models consider finite and local coupling [86-89].

In order to find solutions, first, the integral equation-based methods generate integral statement equations that are the most appropriate for the specific problem. The second

step is a development of the discrete form of the integral statement equations. According to the integral statement equations, integral equation-based method can be classified into two methods: the method of moments (MoM) by Harrington [75] and electric field integral equation (EFIE) based methods [76].

The MoM is a popular method of simulation based on the Dyadic Green's function. The MoM is a 2 ½-dimensional method by assuming the thickness of conductor as zero, so this method is inaccurate than full 3-D methods [4, 85].

The EFIE models can be interpreted in terms of the capacitive, resistive, inductive components, and their couplings [79]. The EFIE methods can construct a complete distributed equivalent-circuit model by using RLC elements. The resulting circuits are called partial element equivalent circuits (PEEC) and will be covered in detail in the next section.

2.3. Partial Element Equivalent Circuit (PEEC) Model

The three dimensional partial element equivalent circuit (PEEC) models have been developed and successfully applied to model the electromagnetic properties of electrical device and interconnect since 1974. The original application was high-speed interconnect modeling [78, 84]. The PEEC method is based on an integral equation description of the geometry that is interpreted in terms of circuit elements. Namely, a target device is modeled as a resistance, inductance, and capacitance circuit with dependent source that are derived from the quasi-static (If retardation is neglected)

integral Maxwell's equations. The PEEC method has advantage over other modeling methods because

1. The output of the PEEC analysis is spice-like equivalent-circuit model, so it can be easily integrated with other circuit models such as transistor models into an input circuit for a conventional circuit simulation tools such as SPICE.
2. The PEEC models work equally well in the time and frequency domains.
3. The PEEC analysis can reduce simulation time by using integral Maxwell's equation.
4. Unlike Maxwell's differential equation RLC lumped models, the PEEC models include cross coupling terms.

The behavior of charges, currents, and electromagnetic fields can be completely described by the Maxwell's equations.

The Maxwell's equation is

$$\nabla \times \overline{H}\left(\bar{r}, t\right) - \frac{\partial \overline{D}\left(\bar{r}, t\right)}{\partial t} = \overline{J}\left(\bar{r}, t\right) \qquad (2.3.1)$$

$$\nabla \times \overline{E}\left(\bar{r}, t\right) + \frac{\partial \overline{B}\left(\bar{r}, t\right)}{\partial t} = 0 \tag{2.3.2}$$

$$\nabla \cdot \overline{D}\left(\bar{r}, t\right) = \rho\left(\bar{r}, t\right) \tag{2.3.3}$$

$$\nabla \cdot \overline{B}\left(\bar{r}, t\right) = 0 \tag{2.3.4}$$

where $\overline{E}$ is the electric field intensity, $\overline{H}$ is the magnetic field intensity, $\overline{D}$ is the electric flux density, $\overline{B}$ is the magnetic flux density, $\overline{J}$ is the current density, and ρ is the charge density [56]. If the medium is isotropic, this can be rewritten as

$$\overline{D}\left(\bar{r}, t\right) = \varepsilon \overline{E}\left(\bar{r}, t\right) \text{ and } \overline{B}\left(\bar{r}, t\right) = \mu \overline{H}\left(\bar{r}, t\right) \tag{2.3.5}$$

where ε is the dielectric constant of the medium and μ is the magnetic permeability. The vector potential $\overline{A}$ and scalar potential ϕ can be used to express the electric and magnetic fields, and the electric field and the current density are directly related by Ohm's law in case of a conductor

$$\overline{B}\left(\bar{r}, t\right) = \nabla \times \overline{A}\left(\bar{r}, t\right) \tag{2.3.6}$$

$$\overline{E}\left(\bar{r}, t\right) = \frac{\partial \overline{A}\left(\bar{r}, t\right)}{\partial t} - \nabla \phi\left(\bar{r}, t\right) \tag{2.3.7}$$

$$\overline{J}\left(\bar{r}, t\right) = \sigma(\bar{r})\, \overline{E}\left(\bar{r}, t\right) \tag{2.3.8}$$

where $\sigma(\bar{r})$ is conductivity of a conductor.

First, from (2.3.7) and (2.3.8), the Electric Field Integral Equation (EFIE) can be obtained

$$\frac{\overline{J}\left(\bar{r},\, t\right)}{\sigma}+\frac{\partial \overline{A}\left(\bar{r},\, t\right)}{\partial t}+\nabla\Phi\left(\bar{r},\, t\right)=0\,. \tag{2.3.9}$$

From the Lorentz gauge condition, the Maxwell equations can be expressed as a set of wave equations

$$\nabla\cdot\overline{A}\left(\bar{r},\, t\right)+\frac{1}{c^2}\frac{\partial\phi\left(\bar{r},\, t\right)}{\partial t}=0 \tag{2.3.10}$$

$$\nabla^2\overline{A}\left(\bar{r},\, t\right)-\frac{1}{c^2}\frac{\partial^2\overline{A}\left(\bar{r},\, t\right)}{\partial t^2}=-\mu\overline{J}\left(\bar{r},\, t\right) \tag{2.3.11}$$

$$\nabla^2\phi\left(\bar{r},\, t\right)-\frac{1}{c^2}\frac{\partial^2\phi\left(\bar{r},\, t\right)}{\partial t^2}=-\varepsilon\rho\left(\bar{r},\, t\right). \tag{2.3.12}$$

The solution of wave equation (2.3.13) and (2.3.14) are obtained and can be coupled through the continuity equation (2.3.15)

$$\overline{A}\left(\bar{r},\, t\right)=\mu\int\overline{G}\left(\bar{r},\, t,\bar{r}',\, t'\right)\overline{J}\left(\bar{r}',\, t'\right)d^3\,\bar{r}'dt' \tag{2.3.13}$$

$$\phi\left(\bar{r},\, t\right)=\frac{1}{\varepsilon}\int\overline{G}\left(\bar{r},\, t,\bar{r}',\, t'\right)\rho\left(\bar{r}',\, t'\right)d^3\,\bar{r}'dt' \tag{2.3.14}$$

$$\nabla\cdot\overline{J}\left(\bar{r},\, t\right)+\frac{\partial\rho\left(\bar{r},\, t\right)}{\partial t}=0\,. \tag{2.3.15}$$

The Green function for the solution of wave equation is given by

$$\overline{G}\left(\overline{r}, t, \overline{r}', t'\right) = \frac{\delta\left(t - t' - \frac{|\overline{r} - \overline{r}'|}{c}\right)}{4\pi|\overline{r} - \overline{r}'|} \cong \frac{1}{4\pi|\overline{r} - \overline{r}'|} \tag{2.3.16}$$

where δ is the Dirac delta function that is the result of the finite light speed and results in a time delay and if retardation is neglected, simple expression can be obtained [76]. The solution of wave equation can be rewritten as

$$\overline{A}\left(\overline{r}, t\right) = \mu \int \overline{G}\left(\overline{r}, t, \overline{r}', t'\right) \overline{J}\left(\overline{r}', t'\right) d^3 \overline{r}' dt' \cong \frac{\mu}{4\pi} \int \frac{\overline{J}\left(\overline{r}', t'\right)}{|\overline{r} - \overline{r}'|} d^3 \overline{r}' \tag{2.3.17}$$

$$\phi\left(\overline{r}, t\right) = \frac{1}{\varepsilon} \int \overline{G}\left(\overline{r}, t, \overline{r}', t'\right) \rho\left(\overline{r}', t'\right) d^3 \overline{r}' dt' \cong \frac{1}{4\pi\varepsilon} \int \frac{\rho\left(\overline{r}', t'\right)}{|\overline{r} - \overline{r}'|} d^3 \overline{r}'. \tag{2.3.18}$$

Using obtained (2.3.17) and (2.3.18), the equation can be rewritten as [82, 83]

$$\frac{\overline{J}\left(\overline{r}, t\right)}{\sigma} + \frac{\mu}{4\pi} \int \frac{\partial \overline{J}\left(\overline{r}', t'\right)}{\partial t'} \frac{1}{|\overline{r} - \overline{r}'|} d^3 \overline{r}' + \frac{1}{4\pi\varepsilon} \nabla \int \frac{\rho\left(\overline{r}', t'\right)}{|\overline{r} - \overline{r}'|} d^3 \overline{r}' = 0. \tag{2.3.19}$$

To derive a PEEC model, a primitive structure, which is partitioned into three capacitive cells (solid line) and two inductive cells (dashed line), is proposed in Figure 2.3.1.

At first glance, the suggested structure looks too simple to have generality but all complex structures can be subdivided into this simple primitive cell. Uniform current flow in the positive x-axis on the inductive cells and no retardation are assumed for this simple model for convenience. The equation (2.3.19) can be expressed as

$$\frac{\overline{J}(x,t)}{\sigma}+\frac{\mu}{4\pi}\int\frac{\partial\overline{J}(x',t)}{\partial t}\frac{1}{|x-x'|}d^3x'+\frac{1}{4\pi\varepsilon}\nabla\int\frac{\rho(x',t)}{|x-x'|}d^3x'=0. \qquad (2.3.20)$$

The unknowns in the derived Maxwell's integral equation are the charges or potentials on the capacitive cells and the current on the inductive cells. The capacitive cells have potential $\Phi_1(t), \Phi_2(t)$, and $\Phi_3(t)$ and charge $q_1(t)$, $q_2(t)$,and $q_3(t)$, while the inductive cells have uniform current $i_2(t)$ and $i_4(t)$ [78, 80,81].

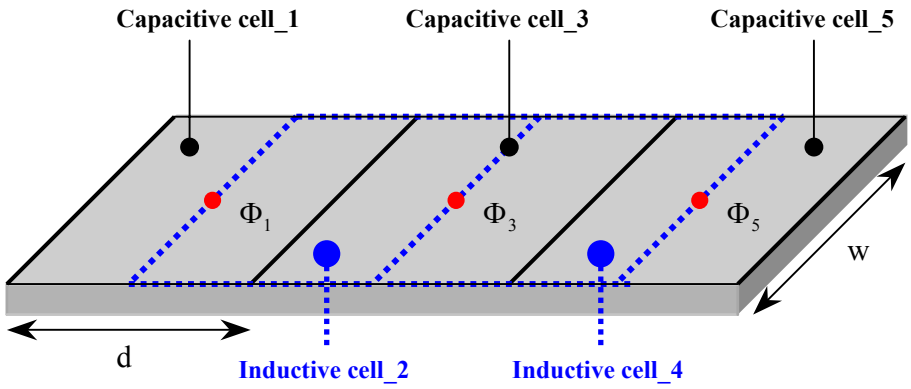

Figure 2.3.1 A primitive and simple structure: a flat metal conductor subdivided into three capacitive cells (solid line) and two inductive cells (dashed line)

First, the first term integration of the equation (2.3.9) is used to derive an expression for the resistance elements in the PEEC model. For example, the resistance of inductive cell2 and cell4 can be obtained by

$$\int_{cell2} \frac{\overline{J}(x_2,t)}{\sigma} d^2x_2 = i_2(t)\frac{d}{\sigma} = i_2(t)\,wR_{22}$$

$$\int_{cell4} \frac{\overline{J}(x_4,t)}{\sigma} d^2x_4 = i_4(t)\frac{d}{\sigma} = i_4(t)\,wR_{44} \tag{2.3.21}$$

where R_{22} is the partial resistance of inductive cell2.

The second term integration of the equation (2.3.9) is used to derive an expression for the inductance elements in the PEEC model. For example, the inductance of inductive cell2 and cell4 can be obtained by integrating the second term of the equation (2.3.9) in cell2 and cell4

$$\begin{aligned}
&\int_{cell2} \frac{\partial \overline{A}(x_2,t)}{\partial t} d^2x_2 \\
&= \frac{\mu}{4\pi}\frac{1}{w}\left[\frac{\partial i_2(t)}{\partial t}\int_{cell2} d^2x_2 \int_{cell2} \frac{1}{|x_2 - x'_2|} d^2x'_2 + \frac{\partial i_4(t)}{\partial t}\int_{cell2} d^2x_2 \int_{cell4} \frac{1}{|x_2 - x'_4|} d^2x'_4\right] \\
&= w\left[L_{p22}\frac{\partial i_2(t)}{\partial t} + L_{p24}\frac{\partial i_4(t)}{\partial t}\right]
\end{aligned} \tag{2.3.22}$$

$$\begin{aligned}
&\int_{cell4} \frac{\partial \overline{A}(x_4,t)}{\partial t} d^2x_4 \\
&= \frac{\mu}{4\pi}\frac{1}{w}\left[\frac{\partial i_4(t)}{\partial t}\int_{cell4} d^2x_4 \int_{cell4} \frac{1}{|x_4 - x'_4|} d^2x'_4 + \frac{\partial i_2(t)}{\partial t}\int_{cell4} d^2x_4 \int_{cell2} \frac{1}{|x_4 - x'_2|} d^2x'_2\right] \\
&= w\left[L_{p44}\frac{\partial i_2(t)}{\partial t} + L_{p24}\frac{\partial i_2(t)}{\partial t}\right]
\end{aligned}$$

where L_{p22} and L_{p24} are the self and mutual partial inductance between cell2 and cell4, respectively.

In the same manner, the partial capacitance can be derived by integrating the third term of the equation (2.3.9) in cell2 and cell4

$$\int_{cell2} \frac{\partial \Phi\ (x_2,t)}{\partial x} d^2x_2 = \frac{1}{d}\left[\int_{cell3} \Phi(x_3,t)\, d^2x_3 - \int_{cell1} \Phi(x_1,t)\, d^2x_1 \right] = w\left[\Phi_3(t) - \Phi_1(t)\right]$$

$$\int_{cell4} \frac{\partial \Phi\ (x_4,t)}{\partial x} d^2x_4 = \frac{1}{d}\left[\int_{cell5} \Phi(x_5,t)\, d^2x_5 - \int_{cell3} \Phi(x_3,t)\, d^2x_3 \right] = w\left[\Phi_5(t) - \Phi_3(t)\right]. \tag{2.3.23}$$

$$\begin{bmatrix} c_{11} & c_{13} & c_{15} \\ c_{13} & c_{33} & c_{35} \\ c_{15} & c_{35} & c_{55} \end{bmatrix} \begin{bmatrix} \Phi_1(t) \\ \Phi_3(t) \\ \Phi_5(t) \end{bmatrix} = \begin{bmatrix} q_1(t) \\ q_3(t) \\ q_5(t) \end{bmatrix} \tag{2.3.24}$$

Combining equation (2.3.21), (2.3.22), (2.3.23), and (2.3.24) resulting in

$$i_2(t)R_{22} + L_{p22}\frac{\partial i_2(t)}{\partial t} + L_{p24}\frac{\partial i_4(t)}{\partial t} + \Phi_3(t) - \Phi_1(t) = 0$$

$$i_4(t)R_{44} + L_{p24}\frac{\partial i_2(t)}{\partial t} + L_{p44}\frac{\partial i_4(t)}{\partial t} + \Phi_4(t) - \Phi_3(t) = 0\,. \tag{2.3.25}$$

In the general case, the i_{th} circuit equations of n inductive and m capacitive cells are

$$i_i(t)\,R_{22} + \sum_{j=1}^{n} L_{pij}\frac{\partial i_j(t)}{\partial t} + \left[\Phi_{l(i)}(t) - \Phi_{k(i)}(t)\right] = 0$$

$$\Phi_i(t) = \sum_{j=1}^{m} C_{ij}^{-1}\, Q_j(t) \tag{2.3.26}$$

where $l(i)$ and $k(i)$ are the index of the capacitive cells connected to inductive cell i.

The corresponding PEEC model of the primitive structure is shown in Figure 2.3.2 [76, 78].

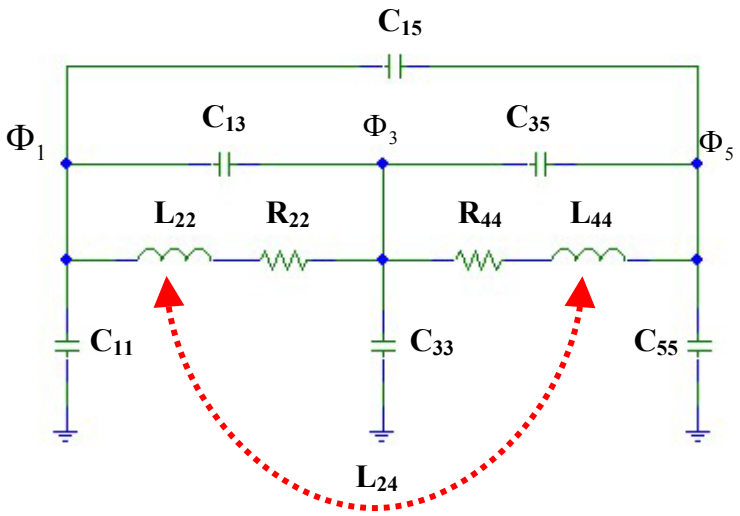

Figure 2.3.2. The PEEC model of the proposed primitive structure.

CHAPTER III

MEASUREMENT-BASED PEEC (M-PEEC) MODEL

3.1. Introduction

In the previous section, RLC components of the PEEC model are derived from numerical analysis of Maxwell's equations. In this section, a measurement-based partial element equivalent circuit (M-PEEC) model will be proposed and demonstrated through a simple example. The proposed measurement-based modeling method generates the equivalent-circuit models of target structures that are constructed from the M-PEEC models of partial elements (PEs). The M-PEEC models have these advantages:

1. The M-PEEC models are accurate because they are derived from test structures and measurements, which automatically include unexpected processing effects such as processing fluctuations, uneven depositions, and non-ideal material properties.
2. The M-PEEC models can be generated easily and simulated very quickly in a standard and conventional circuit simulator.
3. The M-PEEC models can be applicable to both electrical and optical devices (passive and active devices) and interconnects modeling which are electrically long and short structures. In case of optical devices modeling, iterative and

inconvenient interface between optical device and electrical circuit simulators can be overcome.

4. The M-PEEC models are independent of technology or the process in which the structures are fabricated because changed and modified factors are automatically taken into account in the measurements.
5. The M-PEEC models are scalable and predictive since equivalent-circuit models of different size devices can be constructed from obtained several M-PEEC models.
6. The M-PEEC models can take into account statistical information to the models.

In the last section of this chapter, a straight line modeling will be demonstrated and compared to measured data as a case study using two methods: MoM and M-PEEC models.

3.2. Modeling Procedure

The entire modeling procedure is described in Fig. 3.2.1. The first step of the modeling procedure is to identify "What is the target structure? ". And then, primitive cells or partial elements (PEs) can be defined to minimize modeling cost and to maximize accuracy from the target structures. With predefined PEs, test structures are to be designed and fabricated followed by calibration and measurement of the test structures in

order to generate M-PEEC models. The measured data is used to determine the initial guess values of the M-PEEC components and then used to set up optimizations to extract M-PEEC models. Using obtained M-PEEC models, design rules that are associated with the M-PEEC models can be developed. Once a library is constructed, a circuit designer can use it to perform codesign, which means that the circuit designer can choose device specifications according to his or her circuit specifications. If the check fails, then the designer can either redesign the device until it is compliant, or can attempt to define new PEs to satisfy the target performance [4].

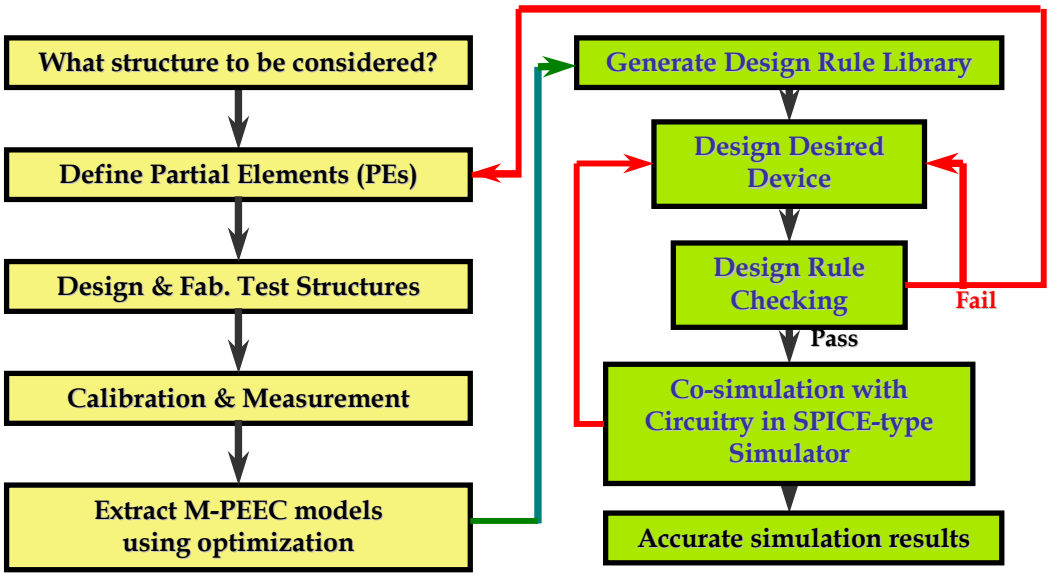

Figure 3.2.1. Modeling Flow chart

3.3. Partial Elements and Test Structures

The basic concept of the proposed modeling method is that any target structures are composed of several key geometrical primitive cells, which is called partial elements (PEs). Accuracy of the whole equivalent-circuit models mainly depends on the accuracy of the measurement-based partial element equivalent-circuit (M-PEEC) models of their partial elements (PEs). Only accurate models for each of the partial elements along with interaction can guarantee the accuracy of any arbitrary geometry structure comprised of those partial elements. In order to effectively use the proposed modeling method, well and properly defined partial elements for the target structures are inevitable.

For example, let's consider a simple straight conductor line with microwave pads in Fig. 3.3.1. This straight line consists of two partial elements: one is the pad and the other is the conductor square partial elements. M-PEEC models are extracted by the use of test structures through optimization process. In the example, straight conductor line is the test structure, which is composed of square and pad partial elements (PEs), and their equivalent-circuit models (M-PEEC) are also shown in the Figure 3.3.1. If a structure is not arbitrary, any structures can be subdivided into several PEs. At first glance, this assumption may seem to be strict, but only several geometrical variations of device shape are available and implementable in most commercial integrated circuit design tools. Even with a small set of partial elements, various geometrical structures can be designed. Moreover, the allowable geometries can easily be added by defining new partial elements and fabricating test structures, and hence the method is highly expandable and scalable.

Once partial elements are determined, test structures that are comprised of those set of the identified partial elements are designed and manufactured in the process of interest.

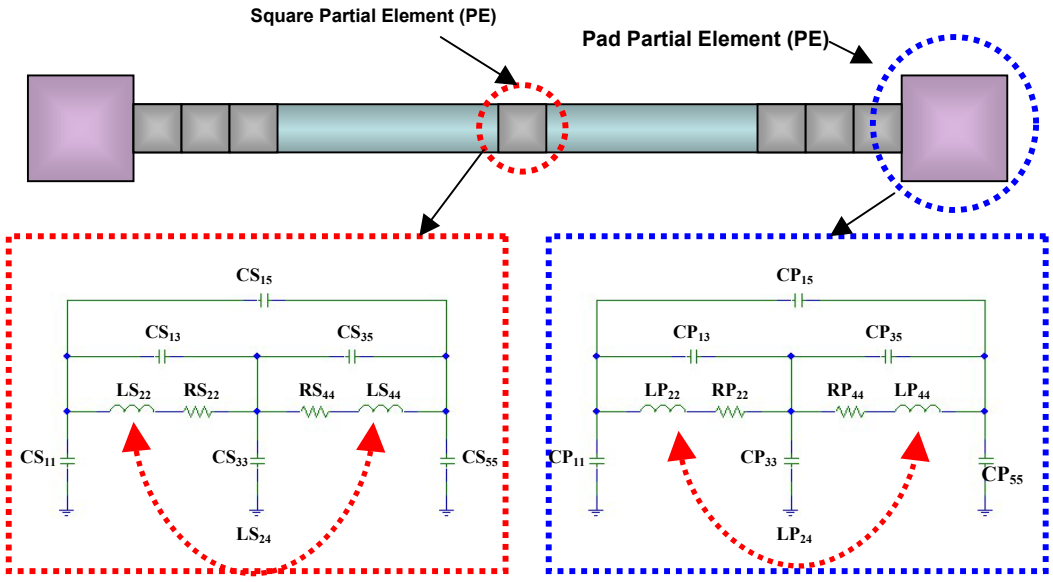

Figure 3.3.1 Test structure (straight line), partial elements (PEs), and their circuit models (M-PEECs)

When the test structures are designed, all the predefined PEs must be sensitive to the overall response of the test structures with respect to frequency. This means that each partial elements should contribute to the overall response of the test structures.

3.4. Measurement-based PEEC (M-PEEC) Model

In case of numerical EM full wave PEEC models, a large and complex geometry structure is broken down into many pieces, partial elements, by segmenting the target

structure. This causes a large simulation time and memory resource. However, the measurement-based partial element equivalent circuit (M-PEEC) models do not need to segment the target structures into a large number of small pieces in order to obtain accurate results. The proposed M-PEEC method uses relatively large pieces compared to finite element and conventional PEEC models. This is because that basis functions are used for discretization procedure in the finite element and conventional PEEC models. In M-PEEC methods no basis functions are assumed on the each partial element, and thus individual behavior of each PE can be directly derived from measurements of test structures. Therefore, the size of the PE has no effect on accuracy, and thus it can be chosen to be relatively large compared to finite element and conventional PEEC models.

The measurement-based PEEC models have advantages. The measured data can take into account unexpected processing fluctuations, variations in materials, and uneven etchings and depositions that came from limits of other technologies. Especially, those properties are important in high-frequency applications. This makes the modeling procedure entirely process independent. The M-PEEC methods can also include statistical information on the process of interest in the models. Many repeatable measurements can be done on the same device under test (DUT) and the same design of device on different runs of a process, and then statistical information can be added to the models.

From the obtained M-PEEC models of the partial elements in the test structures, behavior of other structures comprised of those partial elements can be predicted, resulting in SPICE compatible models. The M-PEEC models can be generated using the

measured data. Using the measured data, generation initial guess values of parameters, optimization for curve fitting, and extraction routines are performed in order to extract RLC models for each of the partial elements. The circuit level modeling approach is powerful since it works well in any standard SPICE compatible circuit simulator.

The equivalency of the PEEC model to Maxwell's Equations already has been proven for small pieces of conductor in section 2.3. The complexity of the M-PEEC directly related to the level of coupling in the model. To consider higher order coupling effects, additional couplings can be easily added to the M-PEEC models. If global interaction and retardation effects are included in the M-PEEC models, more accurate models also can be acquired.

3.5. Case study: Straight line modeling

In this section, a straight line is modeled through two modeling methods: one is method of moment (MoM) that is one of the representative numerical-based EM full wave methods and the other is the proposed method in this thesis. First, the straight line is simulated using MoM in ADS. Second, the test structure is fabricated and measured, and their M-PEEC model of the each partial element (PE) is extracted through optimization procedure. Finally, those two obtained results are compared to measured data.

Fig. 3.5.1 shows the physical layout of the straight line that is meshed into 20 partial elements. For accurate comparison, 20 meshes are used for both methods. The width and

length of the straight line are 25 um and 500 um, respectively. The simulation time is more than one hour for this structure by the MoM in ADS.

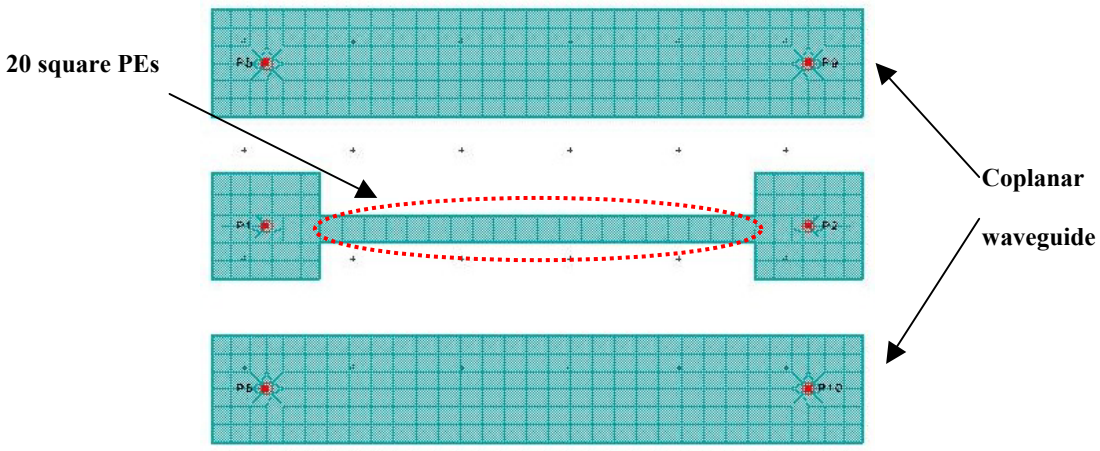

Figure 3.5.1. Straight line that is meshed into 20 square PEs and pads by commercial EM simulator (Mom in ADS)

This test structure was fabricated and measured up to 20GHz for the proposed modeling method. First, the straight line is partitioned into 20 square and 2 pad partial elements (PEs), and then their M-PEEC models are obtained through optimization procedure as shown in Fig. 3.5.2. Their parameter values and results are also shown in Fig. 3.5.3 and Fig. 3.5.4. The obtained M-PEEC models show good agreements with measured data compared to MoM.

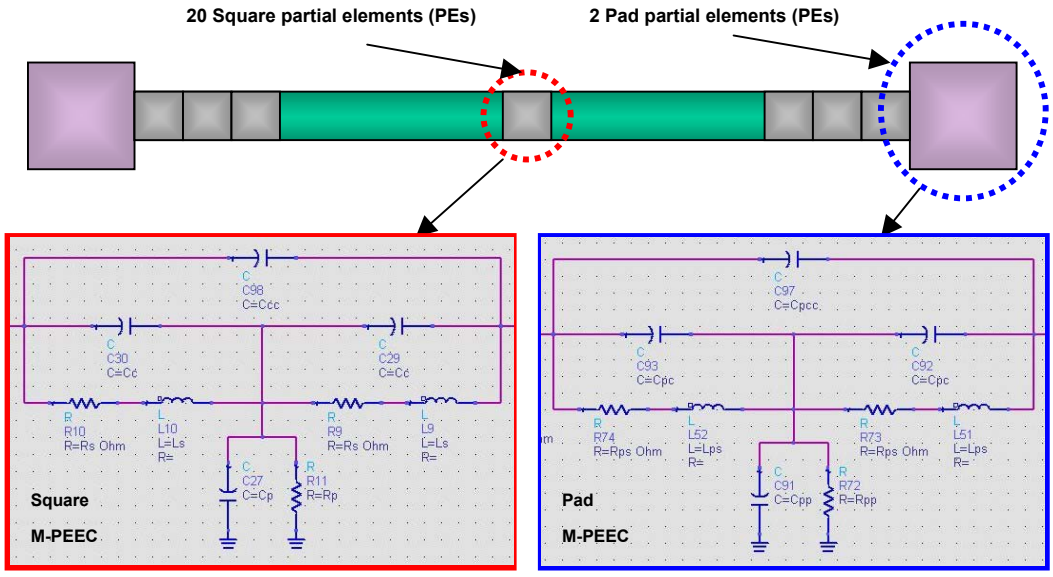

Figure 3.5.2. Straight line that is meshed into 20 square and 2 pads PEs and their M-PEEC models.

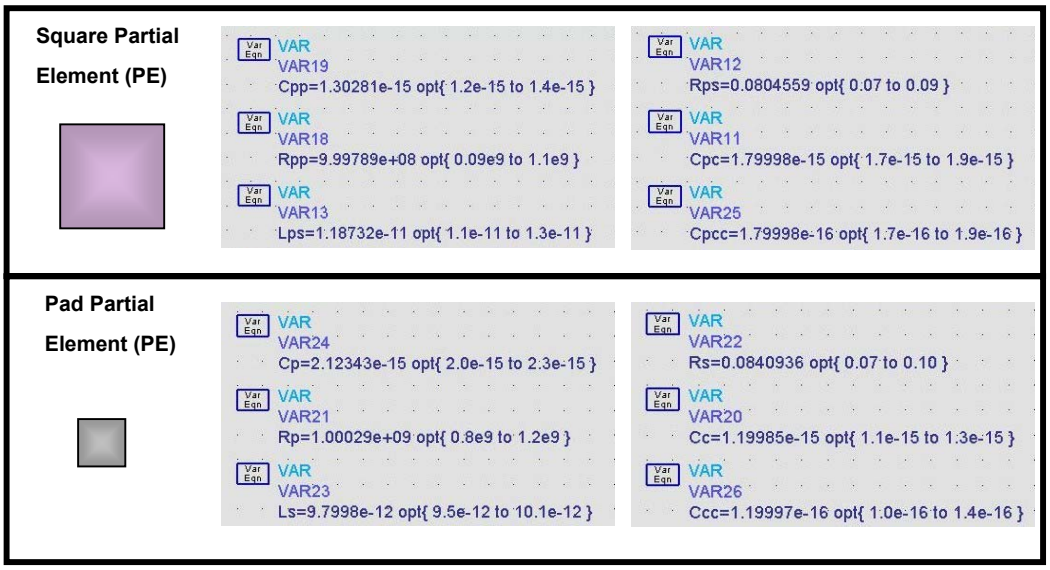

Figure 3.5.3. Two partial elements and their parameter values.

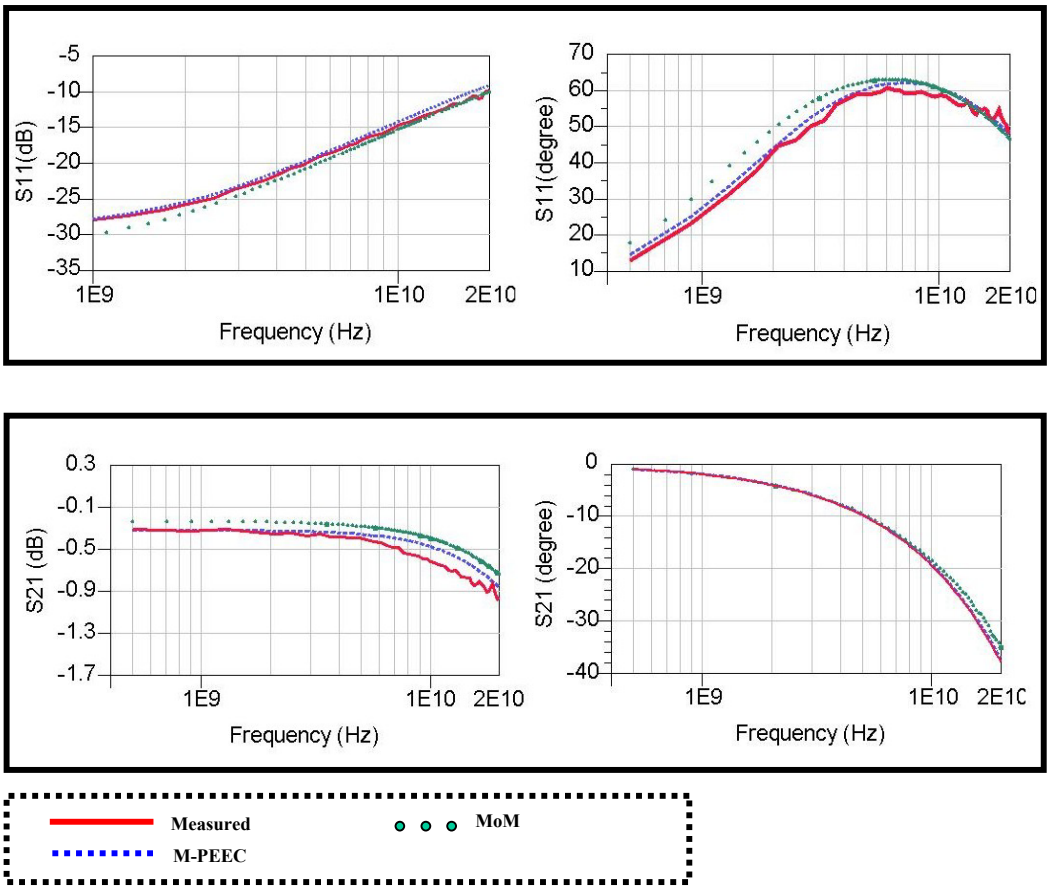

Figure 3.5.4 S11 and S21 comparison: measured data, simulated data of Mom, and simulated data of the proposed method.

CHAPTER IV

FRONT-END OF OPTICAL RECEIVER

4.1. Introduction

Optical communication technology has greatly evolved in the last decades, penetrating all areas of modern telecommunication networks. The initial application of optoelectronics was limited to the long-haul telecommunication segments, but today's application of optoelectronics is spreading to the backbone of metro networks and LAN networks. An optical interconnect and communication system consists of a transmitter (Tx), a data transmission media or channel (usually optical fiber, waveguide, and free space), and a receiver (Rx). The transmitter is comprised of a laser and laser driver circuitry, and the Rx is comprised of a photodiode that is monolithically or hybrid integrated with a low noise preamplifier. Fig. 2.1.1 shows a general optical communication or interconnect system [1, 6].

As the areas of application increase, the demand for higher speed and broader bandwidth in optical communications and interconnects will require high-performance front-end of optical receivers (Rx) in the systems. These requirements emphasize the need to design a photodetector with a preamplifier to acquire the best performance of an optical Rx. The front-end is the main component of an Rx and it is composed of a

preamplifier and a photodiode or photodetector (PD) [1].

Metal-Semiconductor-Metal (MSM) PDs have many advantages such as low capacitance, broad bandwidth, ease of monolithic integration with field effect transistors (FETs), and low dark current [2, 3]. Such properties make MSM PD a promising candidate in optoelectronic integrated circuits (OEIC).

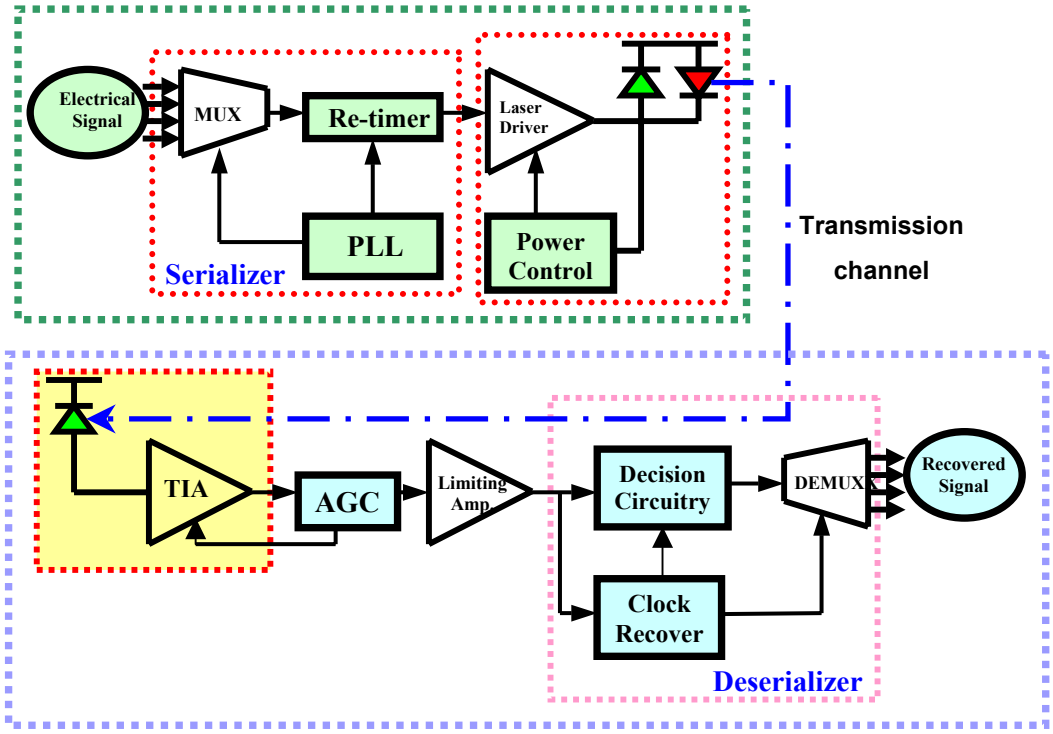

Figure 4.1.1. General optical communications or interconnects system.

Figure 4.1.2 shows applications of the MSM PD. In this chapter, a review of MSM PD and preamplifier will be covered in detail and new complete capacitance and noise model will be presented.

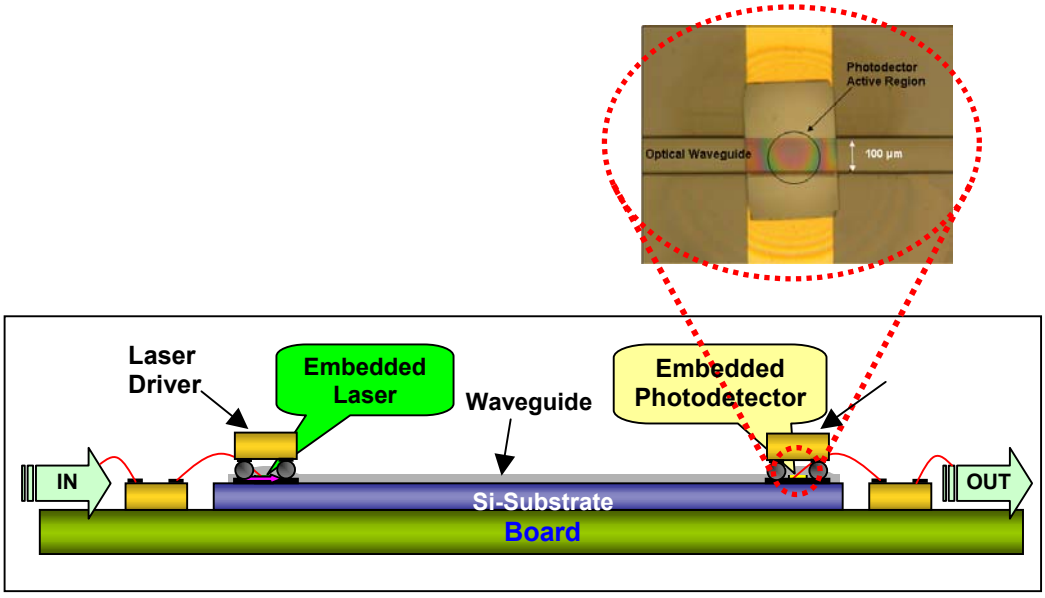

(a) Thin film I-MSM PD in an optical waveguide

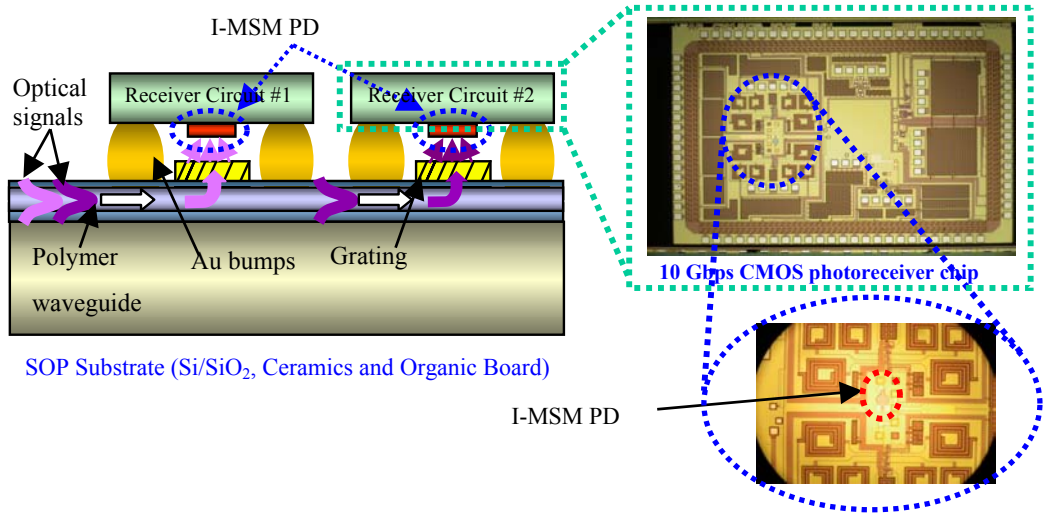

(b) Thin film I-MSM PD in a CMOS optical receiver

4.2. Metal-Semiconductor-Metal Photodiode (MSM PD)

4.2.1. Structure and Physics of MSM PD

An MSM PD is comprised of back-to-back Schottky diodes that use an interdigitated electrode configuration on an undoped semiconductor layer, as shown in Fig. 4.2.1.1. When light with energy hv > Eg is incident, the light that hits the semiconductor surface is absorbed and creates electron-hole pairs (EHs) within the active region, and then one set of electrodes acts as a cathode and the other as an anode. The holes drift toward the negative electrodes, and electrons travel to the positive electrodes under the influence of an electric field by an applied reverse bias voltage [7, 8]. The holes and electrons first slowly diffuse to the junction edge. When the carriers reach the electric field lines created by the applied voltage, the carriers then drift at the saturation velocity toward the electrodes [9]. The wavelengths the semiconductor is sensitive are called the spectral range of the photodetector and the MSM photodetector uses a layer of semiconductor material that is sensitive to the wavelength of interest [10].

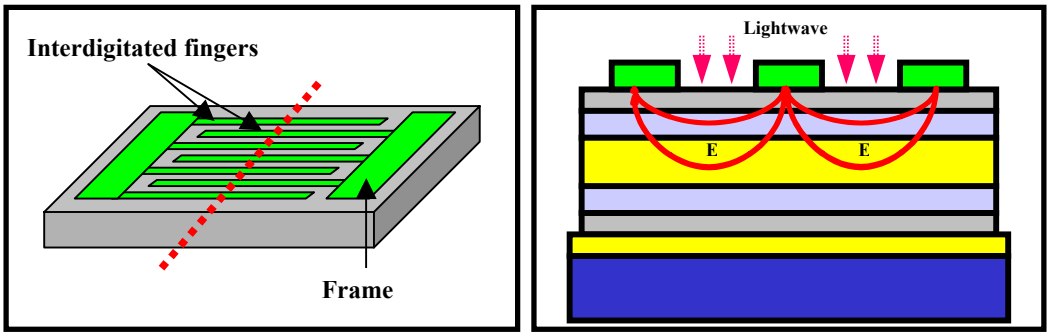

Figure 4.2.1.1. Top view and side view of an MSM PD.

4.2.2. Capacitance

The major parasitic component of the MSM PD is the capacitance. Since the saturation velocity of electrons is faster than that of holes, electrons will be collected first. Then, the holes will be accumulated by the reverse bias. This accumulation of charge slows down the response, adding a much large capacitance component. The capacitance of an MSM is three times smaller than that of a PIN photodetector, and the low capacitance allows large detection area, which resulting in ease of alignment with fiber and optical waveguide. This makes easy coupling to single mode fibers without sacrificing bandwidth and sensitivity [11-13].

A gap capacitance is the capacitance between two adjacent electrodes per unit length and can be expressed as

$$C_o = \varepsilon_o (1+\varepsilon_r)\frac{K(k)}{K(k')} \tag{4.2.2.1}$$

where ε_r is the dielectric constant of the semiconductor, ε_o is the dielectric constant of free space (8.854x10-14 F/cm). K is the complete elliptic integral of the first kind and is defined as

$$K(k) = \int_0^{\frac{\pi}{2}} \frac{d\phi}{\sqrt{1-k^2\sin^2\phi}} \text{ and}$$

$$k = \tan^2\left(\frac{\pi w}{4(s+w)}\right) \text{ and } \quad k' = \sqrt{(1-k^2)} \tag{4.2.2.2}$$

where s is the spacing between electrodes and w is the width of electrode [8,14].

The capacitance of MSM PD is

$$C_{fingers} = (n-1)\,C_o\,l \tag{4.2.2.3}$$

where l is the length of electrode and n is the number of electrodes [11].

Approximated formulas can be used for convenience.

$$\frac{K(k)}{K(k')} = \frac{\pi}{\ln\left[2\frac{1+\sqrt{k'}}{1-\sqrt{k'}}\right]} \quad \text{for} \quad 0 \le \frac{K(k)}{K(k')} \le 1 \text{ and } 0 \le k \le 1/\sqrt{2}$$

$$\frac{K(k)}{K(k')} = \frac{1}{\pi}\ln\left[2\frac{1+\sqrt{k}}{1-\sqrt{k}}\right] \quad \text{for} \quad 0 \le \frac{K(k)}{K(k')} \le \infty \text{ and } 1/\sqrt{2} \le k \le 1 \tag{4.2.2.4}$$

This formula was originated from Lim and Moore's paper and is widely used for characterization of the MSM PD's capacitance, but the effects of the frames of electrodes and light are not included in this formula. Fig. 4.2.2.1 shows a simulated capacitance of the MSM PDs with respect to shape, size, and finger width and spacing.

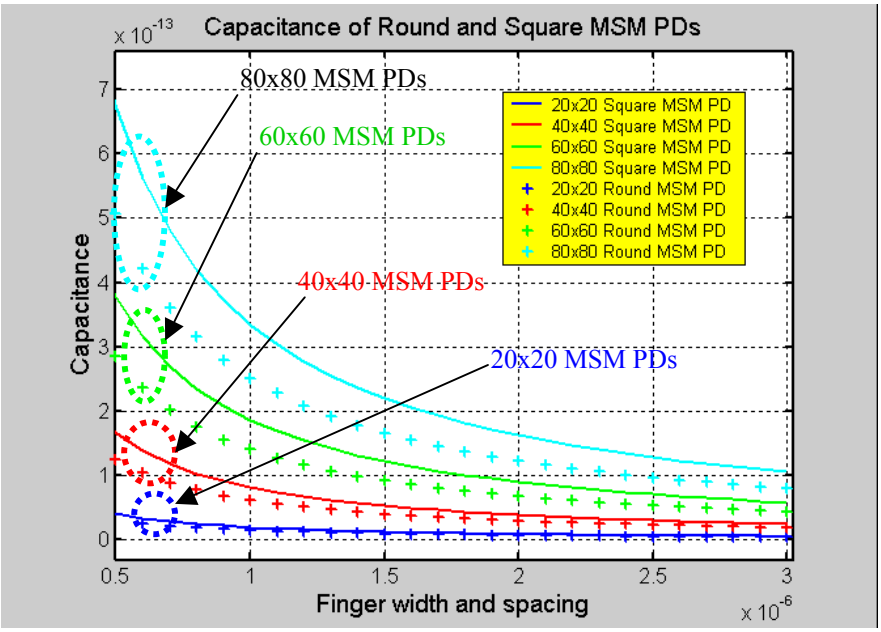

4.2.3. Proposed Complete Capacitance Model

The overall performance and sensitivity of the optical receiver is mainly determined by the front-end performance of the optical Rx. In front-end design, the biggest issue is the reduction in bandwidth because of the additional parasitic capacitances introduced by the PD and pads to the capacitance sensitive preamplifier. Exact characterization of parasitic capacitances of the MSM PD can address limitations on interfacing between MSM PD and preamplifier circuitry for multi-gigabit interconnect and telecommunication applications. Much work has been done and various formulas have been derived to characterize the parasitic capacitance of the MSM PD. Unfortunately, many of these formulas are incorrect because these formulas are directly

quoted from microwave and circuit theory. For example, Lim and Moore proposed a conformal mapping theory to solve the property of periodic interdigitated electrodes in microwave engineering and this theory has been widely used [4]. When they proposed the capacitance formula for interdigitated structures, the effect of frames on both sides that are connected to separate electrodes was not considered. Moreover, this classic formula has been employed by optoelectronic arena directly without considering the illumination effect of light. These two shortcomings cause deviation between theoretical calculation of capacitance and measurements. Although the formula itself is errorless, the usage of the formula has been wrong. Even measurement-based modeling in other papers uses the dark capacitance for their models.

In this section, complete capacitance model of the metal-semiconductor-metal photodiode has been derived and demonstrated through theoretical analysis and measurements. In this work the total capacitance of the MSM PD is calculated using the superposition of each part's contribution such as effects of interdigitated electrodes, frames of electrode, and illumination of light. These theoretical computations are verified with measurements. The results show good agreements between measurements and proposed analytical formulas. For this work, four S-parameters were measured: pad, frame, MSM PD under illumination, and MSM PD without illumination in Fig. 4.2.3.1 and measured results are shown in Fig. 4.2.3.2. Usually dark capacitance is used for the capacitance model of MSM PD but Fig. 4.2.3.3 shows discrepancy between dark capacitance and capacitance under illumination of light.

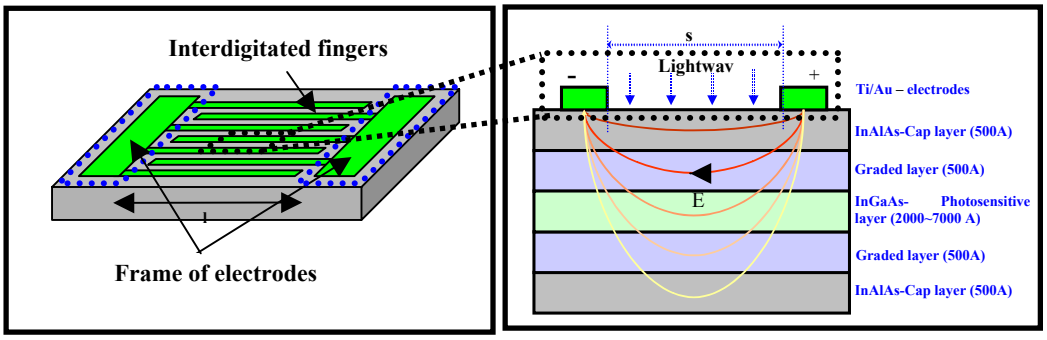

Figure 4.2.3.1. (a) Top view of the MSM PD (b) Side view of the MSM PD: five layers with plot of electric field in each layer

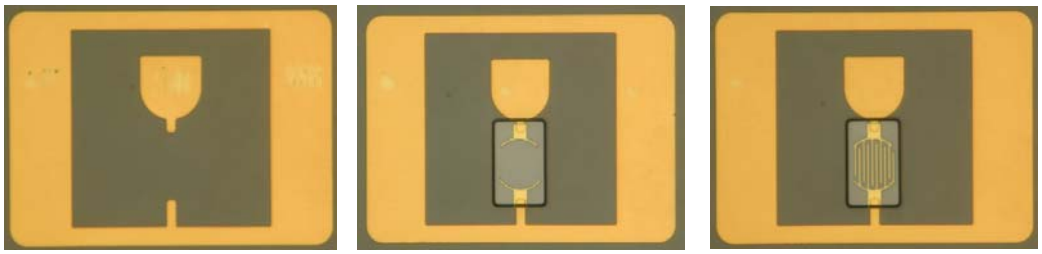

Figure 4.2.3.2. Test structures: (a) Pad (b) Frame of MSM PD (c) MSM PD on pad

First, Lim and Moore's formula in section 4.2.2 can be used for the interdigitated part of the MSM PD. The parasitic effects of frame can be derived using complete elliptic integral of the second kind. MSM PD has several layers besides the active layer (InGaAs) in Fig. 4.2.3.1 (b). The capacitance of the frames that contribute to total MSM PD's capacitance is parallel components. The distance between two frames (by electric field) in each layer can be calculated by a circumference of an ellipse. Each layer has different radius in the minor axis ($2b_x$) and the same radius (2a) in the major axis.

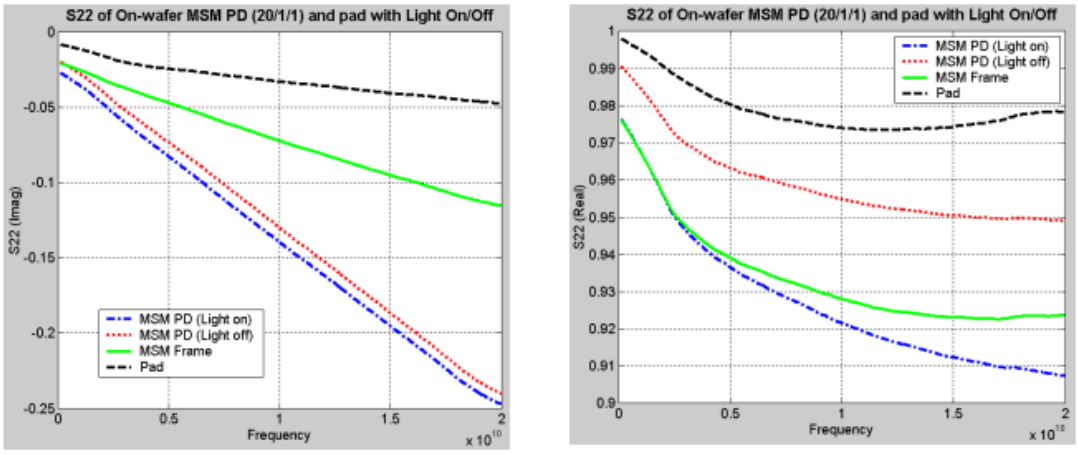

Figure 4.2.3.3. S22 (real and imaginary) of pad, frame, and MSM PD under or without illumination of light at 5V: (a) Imaginary part of the measured S22 (b) Real part of the measured S22

The ellipse's circumference of layer x can be obtained using complete elliptic integral of the second kind [12]

$$L_x = 2a\int_0^{\frac{\pi}{2}} \sqrt{1-e^2\sin^2(\theta)}\; d\theta\,. \tag{4.2.3.1}$$

The approximated formula can also be obtained using numerical analysis.

$$L_x = 2\pi\sqrt{\frac{a^2+b_x^2}{2}}\,. \tag{4.2.3.2}$$

The eccentricity e is defined by

$$e = \frac{\sqrt{a^2-b_x^2}}{a},\quad 0 \le e < 1$$

where 2a is the length of the major axis and $2b_x$ is the length of the minor axis.

The capacitance between two frames is

$$C_x = \varepsilon_0 \varepsilon_r \frac{A}{L_x} \tag{4.2.3.3}$$

where ε_0 is the dielectric constant of air, ε_r is the dielectric constant of each layer, A is the area of frame, and L_x is the distance between two frames by electric field in each layer x.

The total capacitance of the frame is

$$C_{frame} = \sum_{x}^{n} C_x = C_1 + C_2 + C_3 + C_4 + C_5 + ... \tag{4.2.3.4}$$

The illumination effect of light can also be explained through simple theoretical analysis. The capacitance can be obtained by

$$C_{light} = \frac{Q}{V} \tag{4.2.3.5}$$

$$Q = q \cdot \eta_{ext} \left(\frac{AP_o \lambda}{hc} \right)$$

$$\eta_{ext} = \eta_i (1-\Gamma)(1-e^{-\alpha d}) \left(\frac{s}{s+w} \right) \tag{4.2.3.6}$$

where Q is the total charges that is created by illumination of the light, V is the applied bias voltage, and η_{ext} is the external quantum efficiency where q is the charge of electron, A is the area of active region, P_o is the input power, λ is the wave length of the light, h is the plank's constant, c is the speed of light, η_i is the internal quantum efficiency, Γ is the reflection coefficient, α is the absorption coefficient, d is the

distance from surface to the active region, s is the spacing between electrodes, and w is the width of the electrode [14-16].

The total capacitance can be obtained from equation (4.2.2.3), (4.2.3.4), and (4.2.3.5).

$$C_{Total} = C_{fingers} + C_{frame} + C_{light} \tag{4.2.3.7}$$

In this thesis, 5 layers, 1um of finger width and spacing, and 20 um of diameter MSM PD is used. Summary of analysis is given in Table 4.2.3.1. 10 fF of capacitance of interdigitated electrodes is calculated using "Conformal mapping theory" that is proposed by Lim and Moore in equations (4.2.2.1), (4.2.2.2), and (4.2.2.3). The measurement shows 18 fF for the same MSM PD. What makes this huge difference? The capacitance of frame is 5.5 fF that is theoretically derived using "complete elliptic integrals of the second kind" in equations (4.2.3.1), (4.2.3.2), (4.2.3.3), and (4.2.3.4). The measurement shows 6 fF. The capacitance from the effect of light illumination is about 2.7 fF in equations (4.2.3.5), (4.2.3.6). The measurement shows 3 fF. The theoretical total capacitance is 18.2 fF (10+5.5+2.7=18.2 fF) using the proposed capacitance model in equation (4.2.3.7). This shows a good agreement with the measurement (18 fF). This means that the existing formulas directly use RF and circuit capacitance expressions without considering effects of frame and light. This results in smaller capacitance than that of measurement.

Table 4.2.3.1. Summary of analysis for the example.

	Theory	**Measurement**
Capacitance of interdigitated electrodes	By conformal mapping 10 fF	NA
Capacitance of Frames	By the proposed formula 5.5 fF	6 fF
Capacitance from illumination of light	By the proposed formula 2.7 fF	3 fF
Superposition (Total)	18.2 fF	18 fF

4.2.4. Transit Time

It is simply a time for a carrier, created by a photon, to travel through the active region and be collected by the contacts. The transit time can be expressed as

$$\tau_{tr} = \frac{d}{v_{sat}} \tag{4.2.4.1}$$

where v_{sat} is the saturated carrier velocity and d is the distance of travel [17].

The electron and hole have different mobilities, and the disparity can be ten fold or more for direct band gap semiconductors such as GaAs, which collect and emit photons more efficiently than indirect semiconductors such as Si and Ge. Thus, holes take longer to

traverse in the deep active region, where the electric field is low, and therefore can cause a long tail in the impulse response and limit the speed [18, 19].

4.2.5. Bandwidth

There are two main factors that limit the speed of a photodetector. One is the capacitance and the other is the transit time of the hole. The bandwidth can be expressed as

$$f_{3dB} = \frac{1}{2\pi\sqrt{(RC_{Total})^2 + (\tau_{tr})^2}} \qquad (4.2.5.1)$$

where R is the input impedance of the pre-amplifier, C_{Total} is the total capacitance of the PD and contact pads, and τ_{tr} is the transit time of the photo-generated carriers [8, 22]. For example, if a 40x40 um MSM is assumed, the capacitance of the MSM is about 60 fF, resulting in 3 ps of RC time constant and the transit time of the hole is about 7.5 ps. Both capacitance and transit time have dominant effects on a 3-dB bandwidth frequency of the MSM photodetector. The 3-dB bandwidth is about 19.69GHz. Fig. 4.2.5.1 shows the simulated 3dB bandwidth of square MSM PDs with respect to size, finger width, and finger spacing.

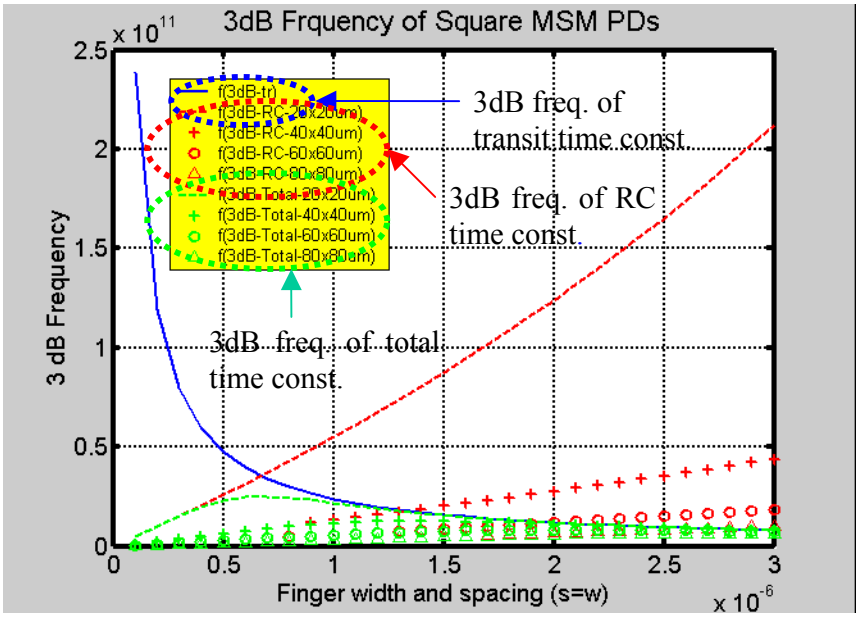

(a) Three time constants: transit, RC, and total time constants

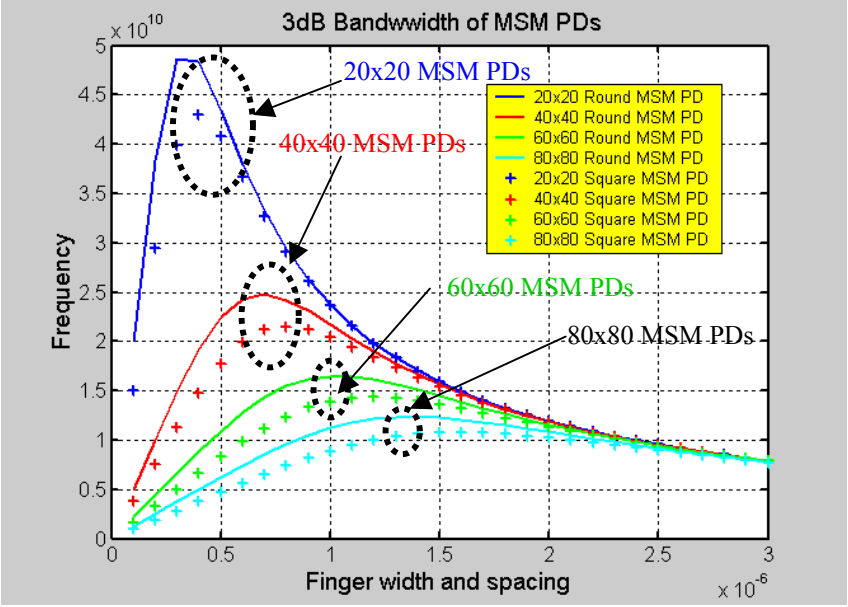

(b) 3 dB bandwidth of the total time constant.

Figure. 4.2.5.1. Simulation results of 3 dB bandwidth.

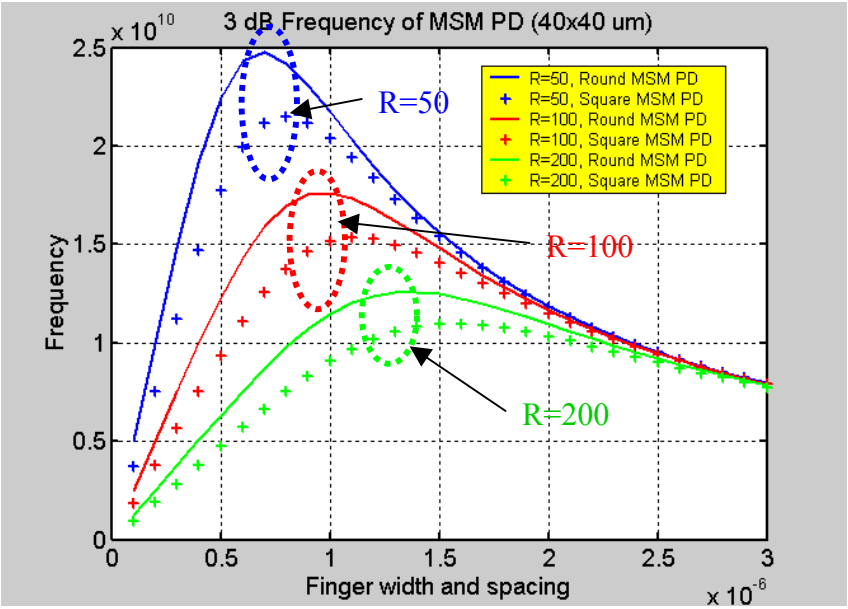

Figure. 4.2.5.2. Simulated 3 dB bandwidth with respect to input impedance.

4.2.6. Responsivity

The quantum efficiency is a degree of how many electron-hole pairs are created per incident photon and then collected by the electrodes to the external circuit. There are two quantum efficiencies. The first one is internal quantum efficiency, which is a ratio of the generated e-h pairs and collected e-h pairs by the contacts, whereas external quantum efficiency is a ratio of the incident photons and the collected photocurrent, thus including effects of surface reflection and the absorption constant of the semiconductor. Internal quantum efficiency generally exceeds 90%, but 30% of the incident light is reflected on the semiconductor surface because of the differences in index of refraction of the semiconductor and air [20-21]. This immediately limits external quantum efficiency below 70%. External quantum efficiency is

$$\eta_{ext} = \eta_i (1-\Gamma)\frac{s}{s+w}(1-e^{-\alpha d}) \tag{4.2.6.1}$$

where η_i is the internal quantum efficiency, Γ is the reflection coefficient at the air-semiconductor interface, s is the finger spacing, w is the finger width, d is the thickness of the absorption layer, and α is the absorption coefficient. The absorption coefficient α is defined as

$$\alpha = 4\pi k / \lambda \tag{4.2.6.2}$$

where k is the extinction coefficient. For $In_{0.53}Ga_{0.47}As$, the extinction coefficient is approximately 0.25 for the wavelength range from 1.3 μm to 1.55 μm [3]. The responsivity is given by

$$\Re = \eta_{ext}\frac{q}{h\gamma} \tag{4.2.6.3}$$

where q is the electric charge and $h\gamma$ is the photon energy.

4.2.7. Photocurrent and Dark current

When light with energy hv > Eg is incident, the light that hits the semiconductor surface is absorbed and creates EH pairs within the active region and this conduction mechanism creates photocurrent. Dark current is a background noise without illumination of light. There are two main mechanisms that control the dark current. One is the spontaneous stimulation of electrons that have sufficient energy to overcome the potential

barrier resulting from thermionic emission. The other is due to tunneling of thermally activated carriers through the barrier [22-24,27].

4.2.8. Proposed Noise Model

The amount of noise present in a receiver will be the primary factor that determines the sensitivity of the receiver. An optical receiver is composed of a photodetector, preamplifier, and post-amplifier stages. The noise factor of an amplifier is defined in equation (4.2.8.1) and overall noise factor of a multi-stage amplifier is described in equation (4.2.8.2).

$$F = \frac{SNR_{input}}{SNR_{output}} \tag{4.2.8.1}$$

$$F = F_1 + \frac{F_2 - 1}{G_1} + \frac{F_3 - 1}{G_1 G_2} + \cdots \tag{4.2.8.2}$$

If the gain (G1) of a preamplifier is large enough, the noise performance of cascaded post-amplifier stages can be neglected in equation (4.2.8.2). It tells us that the dominant factor determining the overall noise performance and sensitivity of the optical receiver is the front-end of the receiver. The noise performance of the front-end depends on the noise characteristic of a photodetector and preamplifier. Noise modeling of a photodiode is important since the photodetector generally appears to be a capacitive current source to the preamplifier in the front-end of optical receiver. There are three main noise components: thermal noise, shot noise, and flicker noise.

The random thermal motion of electrons and holes in a resistive material generates thermal noise, also called Johnson noise. The mean-square open circuit thermal noise voltage across a resistor and the mean-square short circuit thermal noise current is given by

$$\overline{v_t^2} = 4kTR\Delta f$$

$$\overline{i_t^2} = \frac{4kT\Delta f}{R} \tag{4.2.8.3}$$

where k is Boltzmann's constant, T is the absolute or Kelvin temperature, R is the resistance, and Δf is the bandwidth in Hz over which the noise is measured [74].

A simple equivalent circuit model of an MSM PD is a capacitor shunted by a resistor. The impedance is given by

$$Z = R \,||\, \frac{1}{j\omega C} = \frac{R}{1+(\omega RC)^2} - j\frac{\omega R^2 C}{1+(\omega RC)^2}. \tag{4.2.8.4}$$

$$\text{Real(Z)} = \frac{R}{1+(\omega RC)^2} \tag{4.2.8.5}$$

The mean-square thermal noise voltage and the mean-square thermal noise current of the MSM PD are

$$\overline{v_t^2} = \int_0^{\Delta f} 4kT\text{Real(Z)}df = \int_0^{\Delta f} \frac{4kTR}{1+(wRC)^2}df = \frac{2kT}{\pi C}\tan^{-1}(2\pi RC\Delta f) \tag{4.2.8.6}$$

$$\overline{i_t^2} = \int_0^{\Delta f} \frac{4kT}{(\text{Real}(Z))} df = \int_0^{\Delta f} \frac{4kT(1+(wRC)^2)}{R} df = \frac{4kT\Delta f}{R}\left\{1+\frac{(2\pi RC\Delta f)^2}{3}\right\}. \quad (4.2.8.7)$$

Shot noise is generated by the random emission of electrons or by the random passage of electrons and holes across a potential barrier. The shot noise generated in a device is modeled by a parallel noise current source. The mean-square shot noise current in the frequency band Δf is given by

$$\overline{i_{sh}^2} = 2qI\Delta f \quad (4.2.8.8)$$

where q is the electronic charge and I is the dc current flowing through the device. The spectral density of shot noise is flat; thus, shot noise is white noise. There are two noise current sources, dark current and photocurrent. The total shot noise of an MSM PD can be modeled as

$$\overline{i_{sh}^2} = \overline{i_{sh-d}^2} + \overline{i_{sh-ph}^2} = 2q(I_d + I_{ph})\Delta f \quad (4.2.8.9)$$

where I_d is the dc dark current and I_{ph} is the dc photocurrent of the MSM PD [1,3].

Flicker noise is a noise that has a spectral density proportional to 1/f. It is also called "one-over-f noise." Various explanations of its origins have been made, but it remains an ill-understood phenomenon. In resistive materials, its origin seems to be caused by a fluctuation of the mobility of the free charge carriers. In semiconductors, tunneling effects in the surface oxide layer of the material generates it. It is also generated by the imperfect contact between two conducting materials. In this case, it is called

contact noise. Flicker noise is modeled by a noise current source in parallel with a device. In general, the mean-square flicker noise current in the frequency band Δf is given by

$$\overline{i_f^2} = \frac{K_f I^m \Delta f}{f} \tag{4.2.8.10}$$

where I is the dc current, K_f is the flicker noise coefficient, and m is the flicker noise exponent. The flicked noise in an MSM PD can be modeled as

$$\overline{i_f^2} = \overline{i_{f-d}^2} + \overline{i_{f-ph}^2} = \frac{K_f (I_d^m + I_{ph}^m)\Delta f}{f} \tag{4.2.8.11}$$

where I_d is the dc dark current and I_{ph} is the dc photocurrent of the MSM PD.

The total mean-square noise and signal-to-noise ratio of an MSM PD is

$$\overline{i_{total}^2} = \overline{i_t^2} + \overline{i_{sh}^2} + \overline{i_f^2} = \frac{4kT\Delta f}{R}\left\{1 + \frac{(2\pi RC\Delta f)^2}{3}\right\} + 2q(I_d + I_{ph})\Delta f + \frac{K_f (I_d^m + I_{ph}^m)\Delta f}{f}$$

$$SNR = \frac{\overline{i_{ph}^2}}{\overline{i_{total}^2}} \tag{4.2.8.12}$$

The noise model of a front-end receiver is shown in Fig. 4.2.8.1. This noise model can be partitioned into three parts, photodetector, pad, and pre-amplifier, each with equivalent noise sources. The noise current i_{total} is obtained from the total equivalent current noise in equation (4.2.8.12). v_t comes from thermal noise in pad, v_{amp}, i_{amp}, and i_{corr} are the equivalent noise sources related to preamplifier [29].

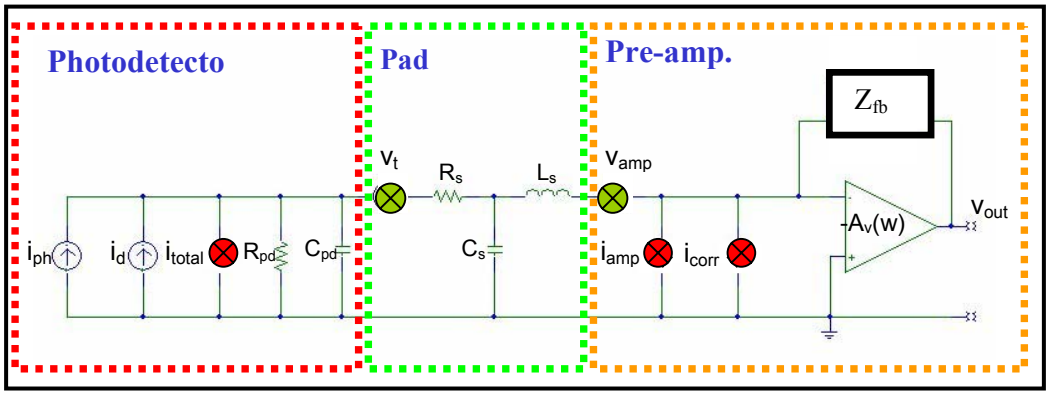

Figure 4.2.8.1. Noise model for the front-end of an optical receiver.

4.2.9. Lumped equivalent-circuit model of the MSM PD

Lots of work has been done for the modeling of the MSM PD. However previous modeling uses dark measurement in their models and only S22 has been modeled. In this section lumped equivalent-circuit model of the MSM PD that is based on physical analysis and measurements is presented. Fig. 4.3.9.1 shows the photograph of I-MSM PD with its circuit model. The test structure partitioned into two components: pad (from dotted line A to B) and MSM photodetector (from dotted line B to C). The results are shown in Fig. 4.3.9.2. Simulated S-parameter is compared to measured data up to 20GHz and eye-diagram is also simulated using the obtained equivalent-circuit model at 10, 20, and 40 Gbps.

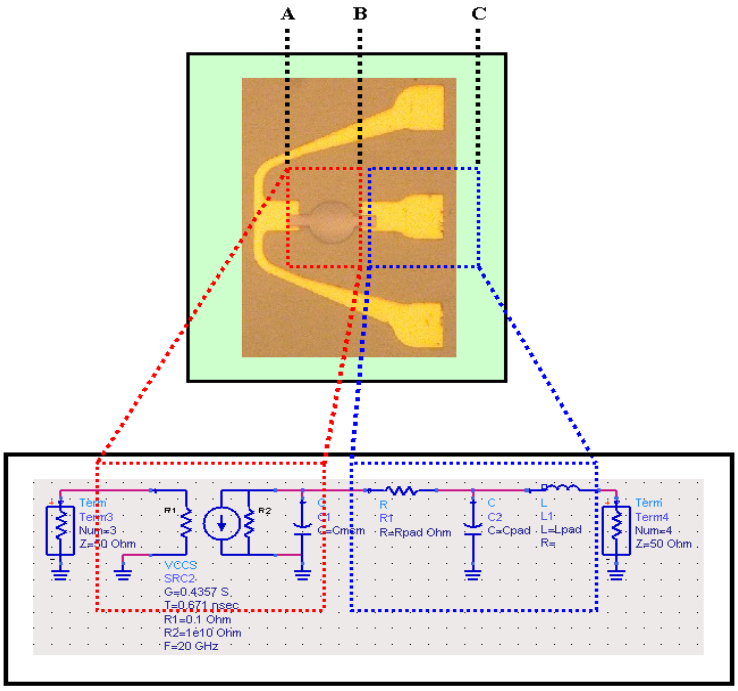

Figure 4.3.9.1. Equivalent circuit models of pad and MSM PD at 5V.

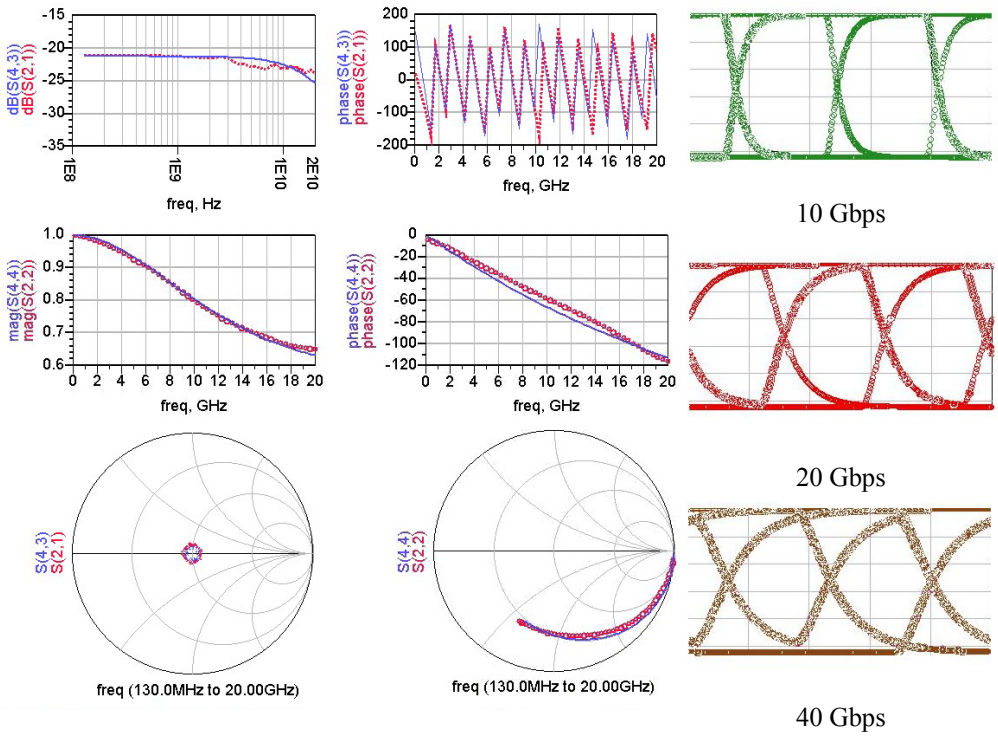

Figure 4.3.9.2. Simulated/measured S-parameters and eye patterns.

4.3. Preamplifier

The key performance metrics of a front-end receiver are bandwidth, gain, sensitivity, stability, noise level, and dynamic range. The preamplifier of the front-end has dominant effects on the bandwidth, noise performance, and sensitivity as shown in equations (4.2.8.1) and (4.2.8.2). To get higher bandwidth, a small input resistance is needed and to get good sensitivity, a large resistance is required in the signal path to minimize thermal noise [25]. Thus, the transimpedance architecture is the best candidate as a preamplifier since it provides a large bandwidth by synthesizing a small input resistance using a much larger feedback resistor. Transimpedance amplifiers (TIA) are used to convert low level photodiode currents to usable voltage signals. To stabilize the amplifier's transimpedance, the TIA hires shunt negative feedback [28]. Fig. 4.3.1 shows a measurement setup for eye-diagram measurement.

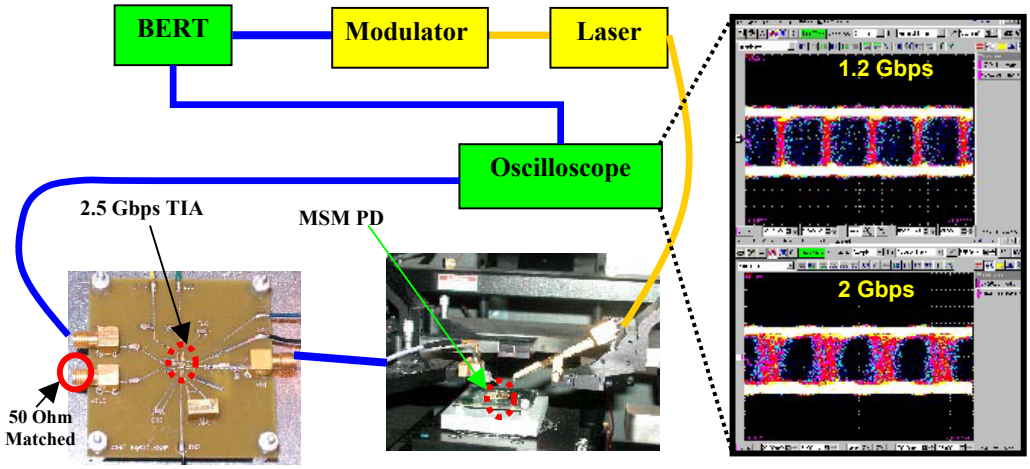

Figure 4.3.1. Measurement setup and measured eye-diagrams at 6V.

4.3.1. Feedback in Preamplifier

The main advantages of feedback are desensitizing gain to process parameter variation, extending the bandwidth, reducing nonlinear distortion, reducing the effects of noise, and controlling the input and output impedance levels. Fig. 4.3.1.1 describes a general feedback system [29, 71-73]].

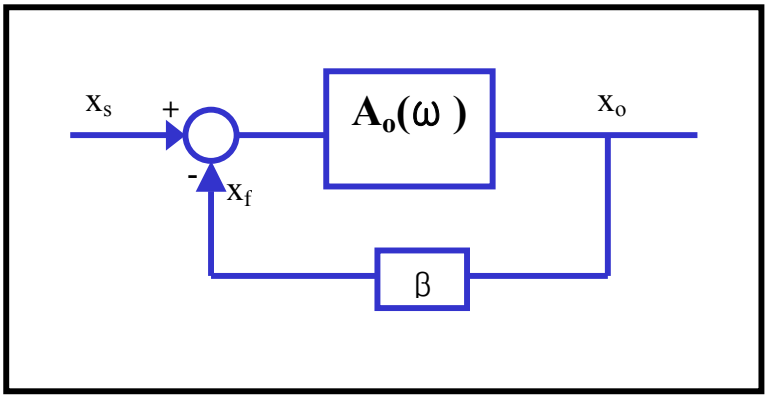

Figure 4.3.1.1. General structure of the feedback amplifier.

The open-loop gain is $A_o(\omega)$ and closed-loop gain is

$$A_C(\omega) = \frac{A_o(\omega)}{1 + A_o(\omega)\beta} \cong \frac{1}{\beta} \tag{4.3.1.1}$$

If the value of the open-loop gain, $A_o(\omega)$, becomes large, then the closed-loop gain approaches $\frac{1}{\beta}$.

4.3.2. Common Source (CS) Preamplifier

Fig. 4.3.2.1 shows a single-ended and differential common source (CS) pre-amplifier with feedback and its equivalent small-signal models. Large value of feedback resistor is usually used to perform several important functions. The voltage at the drain will be equal to the gate voltage, since there is no DC current flowing path through the feedback resistor when the input is AC coupled at DC. This ensures that the transistor is always in saturation and provides biasing without other components [1, 33-35].

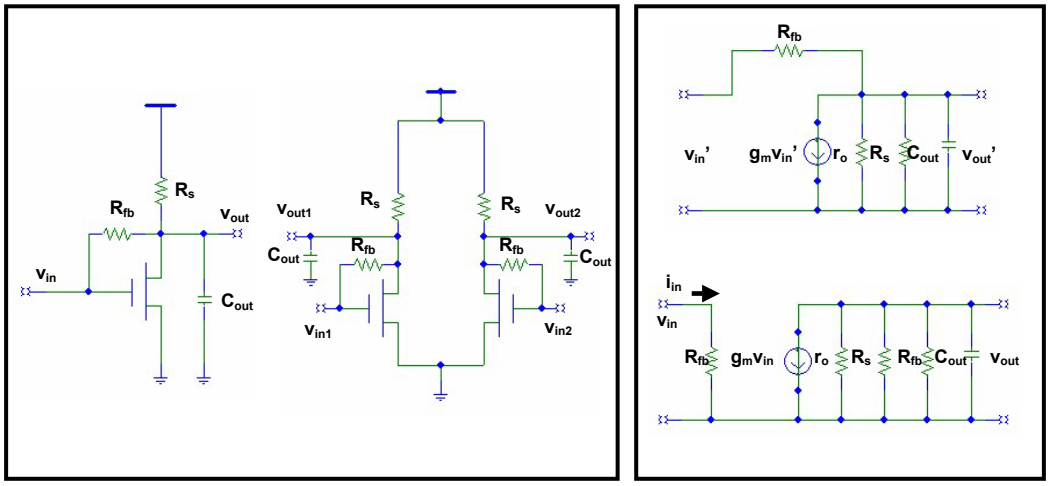

(a) Single-ended and differential topology (b) Small-signal models

Figure 4.3.2.1. Basic common source (CS) preamplifier.

The open-loop gain can be calculated by

$$A_o = \frac{v_{out}}{i_{in}} = \frac{v_{out}}{v_{in}} \frac{v_{in}}{i_{in}} = [-g_m (r_o \parallel R_s \parallel R_{fb} \parallel \frac{1}{j\omega C_{out}})]R_{fb}. \qquad (4.3.2.1)$$

The input impedance, output impedance, and feedback gain are

$$Z_{in} = R_{fb} \tag{4.3.2.2}$$

$$Z_{out} = r_o \parallel R_s \parallel R_{fb} \parallel \frac{1}{j\omega C_{out}} = R_{eq} \parallel \frac{1}{j\omega C_{out}} \tag{4.3.2.3}$$

$$\beta = \frac{-1}{R_{fb}} \tag{4.3.2.4}$$

$$R_{eq} = r_o \parallel R_s \parallel R_{fb}\,.$$

Using equation (4.3.2.1), the closed-loop gain becomes

$$A_C = \frac{A_o(\omega)}{1 + A_o(\omega)\beta} = \frac{-g_m R_{fb} Z_{out}}{1 + g_m Z_{out}} = \frac{-R_{fb}}{1 + \dfrac{(1 + j\omega R_{eq} C_{out})}{g_m R_{eq}}}\,. \tag{4.3.2.5}$$

Fig. 4.3.2.2 shows simulation results with respect to different input capacitance at 10Gbps. The preamplifier is quite sensitive to parasitic input capacitance that mainly comes from photodetector and pad.

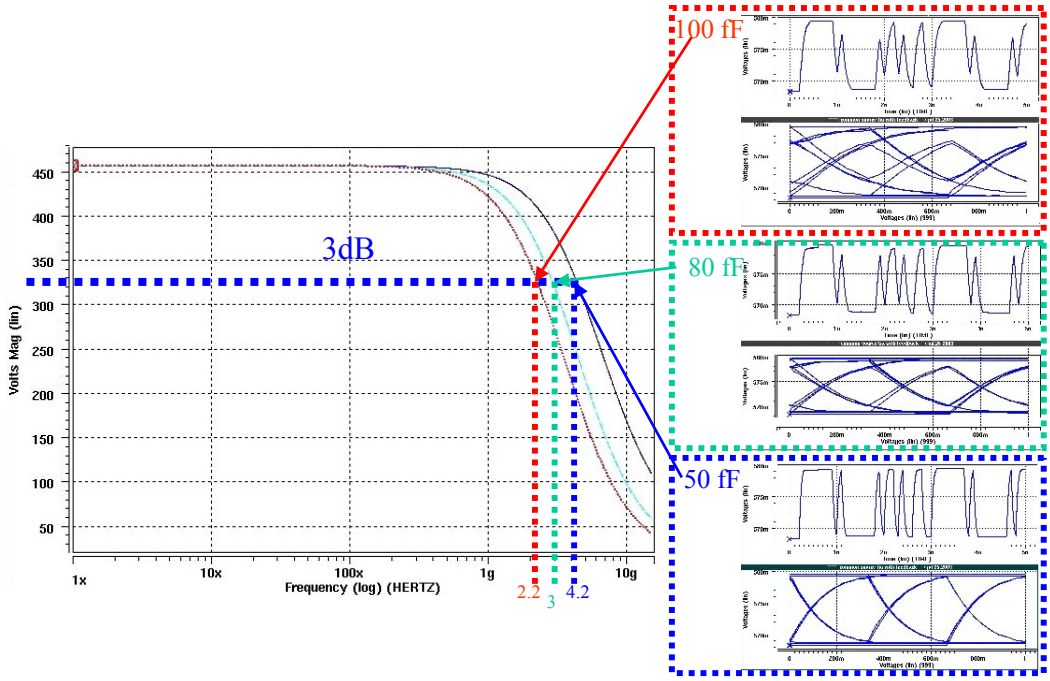

Figure 4.3.2.2. Simulation results with respect to different input capacitance at 10Gbps.

4.3.3. Shunt Peaking in Common Source Preamplifier

To enhance bandwidth, inductors are commonly used in narrow-band applications. They are also can be used in broad-band circuits. Especially, on-chip inductors can improve the bandwidth by shunt peaking in the frequency response. An attractive advantage of this enhancement technique is a 30% increase in the transimpedance with no additional power dissipation. Fig. 4.3.3.1 illustrates a single and differential CS amplifier with shunt peaking and its equivalent circuit models [30-32, 71].

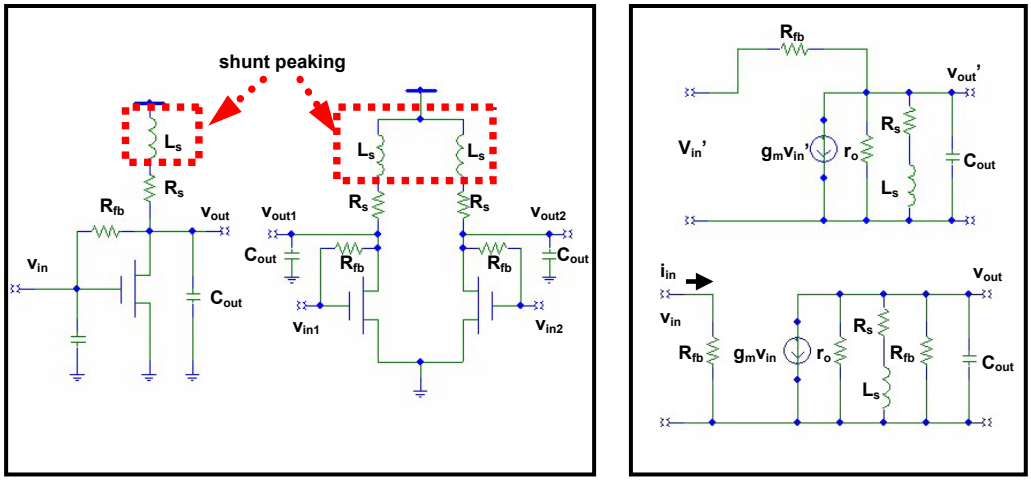

(a) Shunt peaking in single-ended and differential CS preamplifier with feedback

(b) Small-signal models

Figure 4.3.3.1. Shunt peaking circuit in common source preamplifier.

The open-loop gain can be calculated by

$$A_o = \frac{v_{out}}{i_{in}} = \frac{v_{out}}{v_{in}}\frac{v_{in}}{i_{in}} = [-g_m(r_o \parallel (R_s + j\omega L_s) \parallel R_{fb} \parallel \frac{1}{j\omega C_{out}})]R_{fb}. \tag{4.3.3.1}$$

The input impedance, output impedance, and feedback gain are

$$Z_{in} = R_{fb} \tag{4.3.3.2}$$

$$Z_{out} = r_o \parallel (R_s + j\omega L_s) \parallel R_{fb} \parallel \frac{1}{j\omega C_{out}} \tag{4.3.3.3}$$

$$\beta = \frac{-1}{R_{fb}}. \tag{4.3.3.4}$$

Using equation (4.3.3.1), the closed-loop gain becomes

$$A_C = \frac{A_o(\omega)}{1 + A_o(\omega)\beta} = \frac{-g_m R_{fb} Z_{out}}{1 + g_m Z_{out}} \tag{4.3.3.5}$$

$$= \frac{-R_{fb} g_m (r_o \parallel R_{fb})(R_s + J\omega L_s)}{[R_s + (r_o \parallel R_{fb})(1 + R_s) + g_m R_a R_s] + j\omega[L_s + L_s g_m (r_o \parallel R_{fb}) + C_{out} R_s (r_o \parallel R_{fb})] - \omega^2 (r_o \parallel R_{fb}) C_{out} L_s}$$

A single pole is obtained from the small-signal frequency response of the CS pre-amplifier in equation (4.3.3.1). An insertion of inductance in series with the resistance enhances the bandwidth of the amplifier by transforming the frequency response from that of a single pole to that of two poles and a zero in equation (4.3.3.5). The zero is determined solely by the time constant of R_s and L_s and is primarily responsible for the bandwidth enhancement [32, 68-70]]. Fig 4.3.3.2 shows a simulation results of different circuit topology such as single-ended common source, feedback, and shunt peaking in the preamplifier. Eye diagrams that were simulated at 5Gbps and 10 Gbps are also presented in Fig. 4.3.3.3.

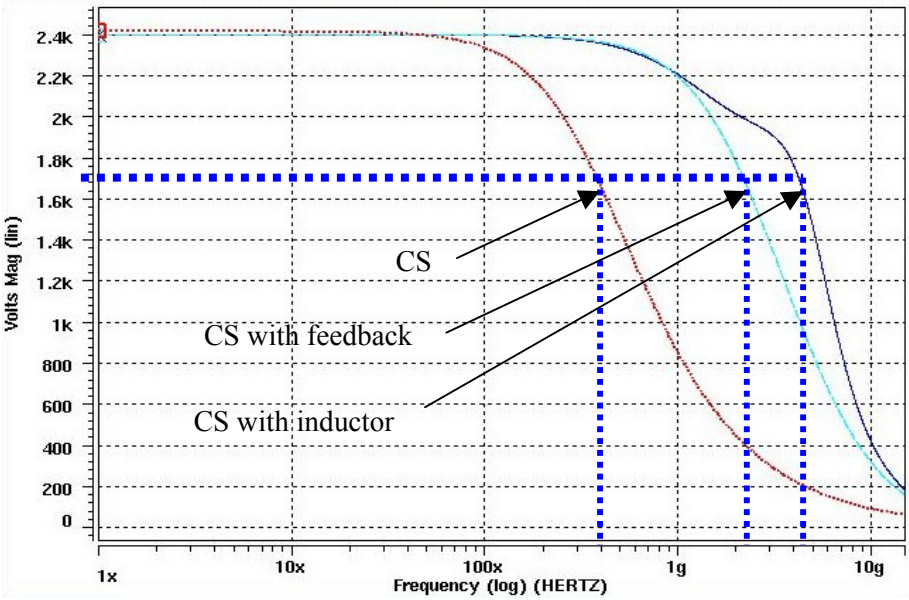

Figure 4.3.3.2. Simulation results of different circuit topology: single-ended common source, feedback, and shunt peaking.

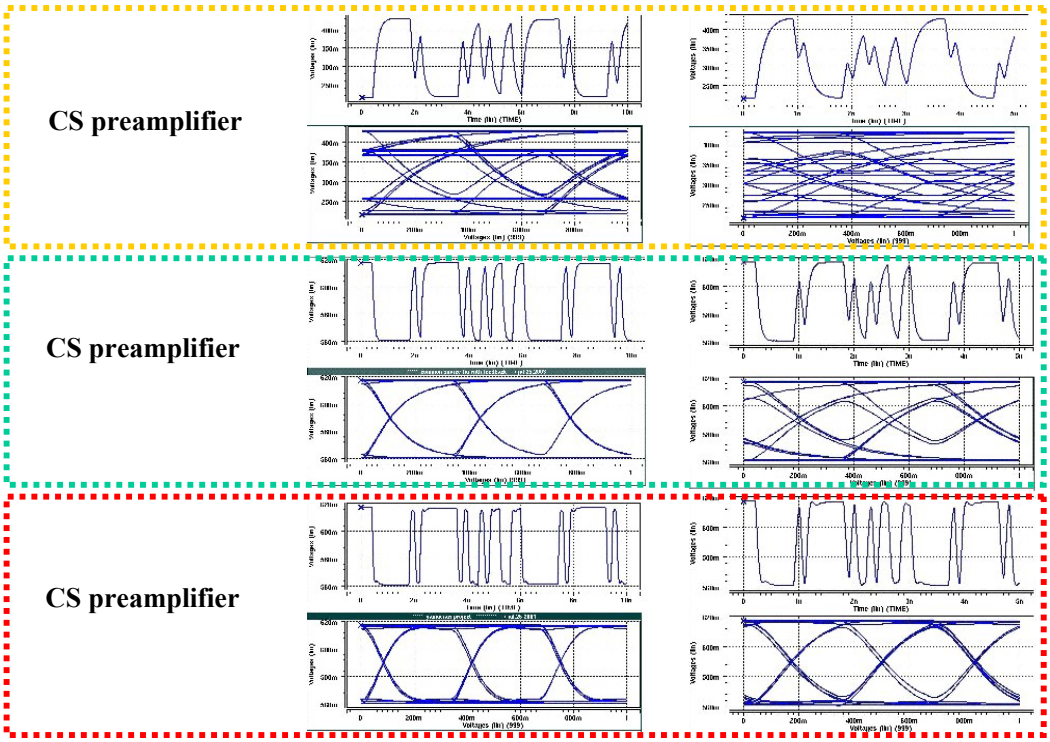

Figure 4.3.3.3. Simulated eye diagrams that were simulated at two different speeds: 5 Gbps and 10 Gbps.

4.3.4. Cascode in Common Source Preamplifier

The cascode eliminates the bandwidth degradation resulting from the Miller gate-drain capacitance of the common source stage. This degradation is particularly significant in CMOS circuits, where the gate-drain capacitance can be as high as one third of the gate-source capacitance. The cascode also enhances the overall gain by increasing the stage's output impedance. The dominant pole in the amplifier occurs at the drain of the cascode transistor. The bandwidth of the amplifier is improved by applying shunt peaking at this node [2, 29,37-40,67].

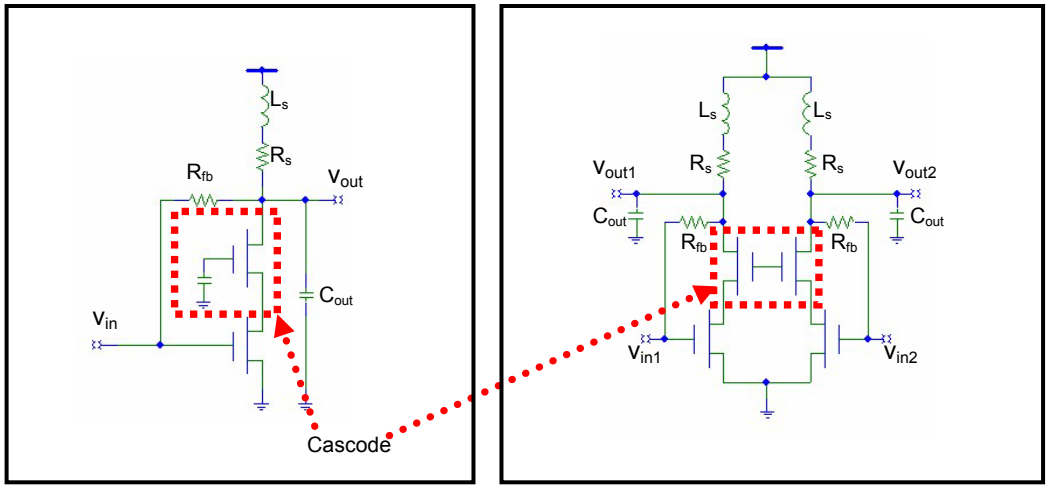

4.3.5. Decoupling Preamplifier from Photodiode

If a photodiode is directly connected to a transimpedance amplifier stage, the best sensitivity can be achieved at a given input power level. However, such an direct connection requires the known parasitic impedance of the photodiode so that the transimpedance stage can be designed for optimal performance. Employing the common gate (CG) stage offers an additional degree of freedom for the designer and permits stable operation over a wider range of photodiode capacitances by decoupling TIA from the photodiode in Fig. 4.3.5.1. The drawback of the common gate is the degradation in the high-frequency noise performance resulting from the source junction capacitance of the common-gate transistor and low sensitivity [33].

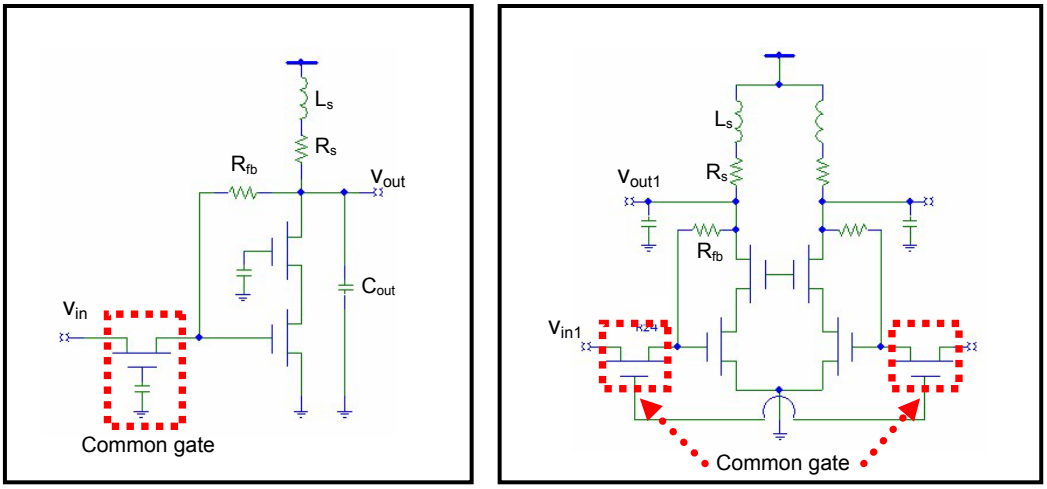

Figure 4.3.5.1. Decoupling TIA from PD using CG stage for single-ended and differential amplifier.

Although single-ended architectures are simple, consuming less power, and saving chip area, they become unstable easily and have worse noise performance from parasitic feedback paths. Differential architectures overcome these disadvantages by providing good common mode rejection. These topologies can improve noise performance in systems where the integration of the analog and digital functions is required. A fully differential structure provides complementary outputs, which is a necessity for clock recovery circuitry operating in differential mode. Fig. 4.3.5.2 shows the schematic of the differential preamplifier. The common gate (CG) stage is followed by the common-source (CS) transimpedance stage, whose output goes to a source follower that buffers the output driver. The output driver is needed only for testing purposes [32, 34, 35].

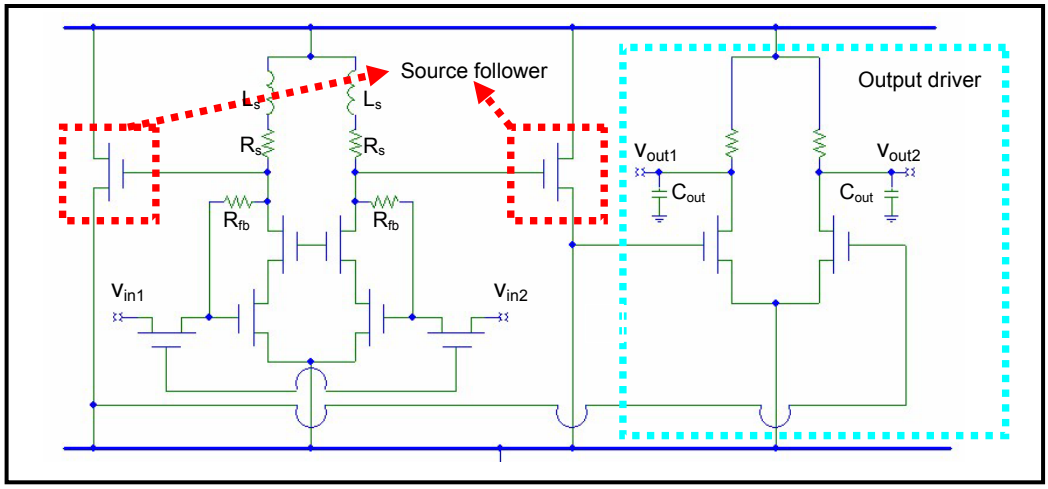

Figure 4.3.5.2. Differential pre-amplifier followed by source follower and output driver.

CHAPTER V

FABRICATION AND MEASUREMENT

5.1. Introduction

There are several fabrication steps to make the test structures. Those test structures are: on-wafer MSM photodetectors, inverted-MSM photodetectors, and on-wafer calibration structures (impedance standard substrate). All structures were fabricated in the Microelectronics Research Center cleanroom of Georgia Institute of Technology by Dr. Nan M. Jokerst's group.

In case of measurement-based modeling methodology, the accuracy of the M-PEEC models mainly depends on the accuracy of the measurements. The high-frequency measurements are very difficult and challenging because small environmental changes such as small bending of cables and small damage of connectors can cause unexpected effects on the measured data. Two measurements were done: S-parameters in the frequency domain and impulse response in the time domain.

5.2. Fabrication

5.2.1. On-wafer MSM PD

The main fabrication steps of on-wafer MSM PDs are: metallization, benzocyclobutene (BCB) coating, BCB patterning, and probing pads deposition.

Probe pads on the photosensitive material result in big parasitic capacitance because size of the pads is much larger than that of MDM PDs. To avoid such a situation, an isolation layer (BCB, 1.0- 3.0 μm) that has very low dielectric constant is spin-coated on the photosensitive layer, and then a window mask is used to make a window through an isolation layer where electron hole pairs are only generated at this region. The reactive ion etching (RIE) is used to male a window using SF_6 and O_2. This can avoid electron hole pair generation under the probe pads. The final thickness of the BCB after RIE etching is about 1.1 μ m. After those procedures, the metal electrodes (fingers) and probe pads are made by direct deposition. As a metal layer Ti/Pt/Au (300 Å/400 Å/2500 Å) is used. During a curing procedure (220 to 245 C), Au diffuses into a compound semiconductor material. The diffused Au into semiconductor causes an ohmic contact or a leaky Schottky contact in stead of high-barrier Schottky contact, which results in large dark current. To prevent this, Pt layer is used. The curing step is done in a nitrogen flow oven for one hour. Fig. 5.2.1.1 shows the fabricated on-wafer MSM PDs.

Figure 5.2.1.1. The fabricated on-wafer MSM photodetectors with different shape: round and square.

5.2.2. Thin Film I-MSM PD

The fabrication and integration of the thin film inverted-MSM PDs includes negative photolithography to define the fingers and contact pads of MSM PDs, e-beam evaporation and lift-off for metalization, mesa etch to separate the MSM devices, substrate removal to realize thin film devices, and transferring and bonding of devices to host substrates. Fig. 5.2.2.1 shows the fabrication and integration procedures. Ti (300 Å)/Pt (350 ~500 Å)/Au (2500 ~3000 Å) are used as a metal layer for the interdigitated electrodes and probe pads. To improve adhesion, Ti is used between other metal materials and semiconductor. As described earlier, Pt is used to prevent Au from diffusion into a compound semiconductor material during curing step.

On-wafer MSM photodetectors can be individualized or separated through a mesa etching using Citric acid and H_2O_2 (10:1). InGaAs is used to stop the mesa etching. To remove substrate, a sample is coated with Apiezon W for protection, and then the substrate (InP) is removed by wet etching using HCl or HCl: H3PO4 (3:1) followed by etching process of step etch layer (InGaAs) using citric acid and H_2O_2 (1:1) for around 2

minutes, which results in about 1 μ m thickness thin film MSM PD.

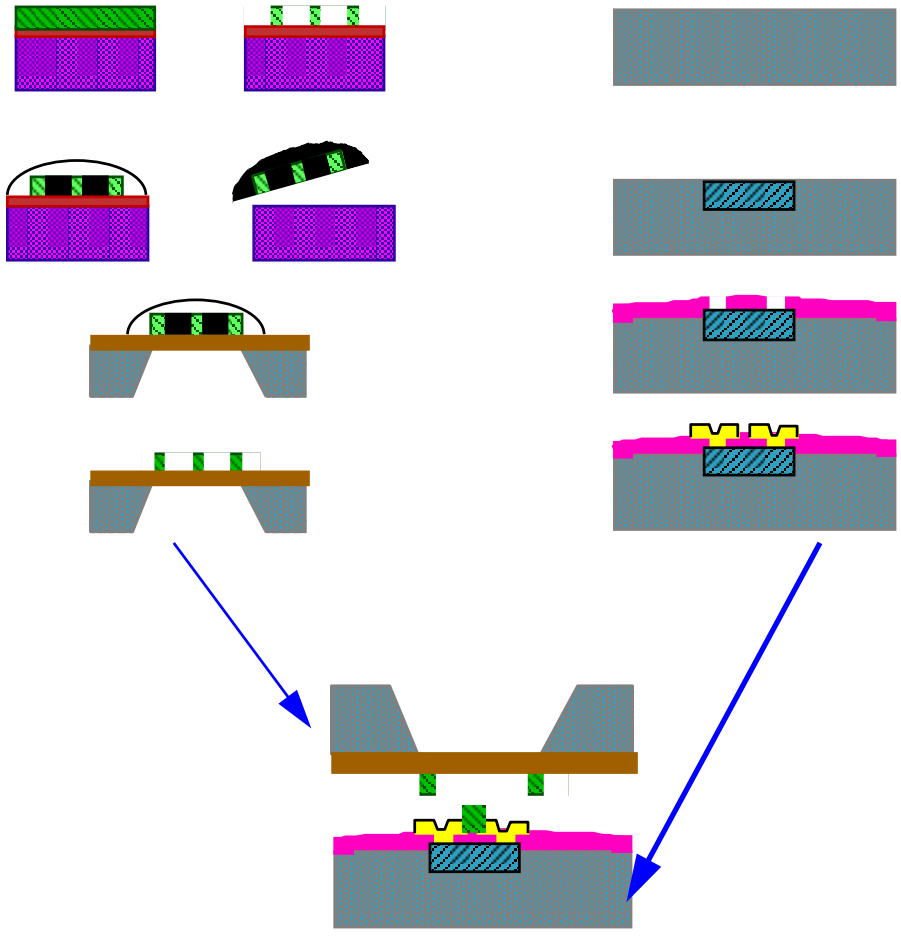

Figure 5.2.2.1. The fabrication and integration procedures.

Finally, the thin film MSM PD is bonded onto a tight thin Mylar® polymer sheet, and then the Apiezon W is removed using TCE. Now, the obtained thin film MDM PD is inverted to avoid shadowing effect, and then integrated onto a host substrate.

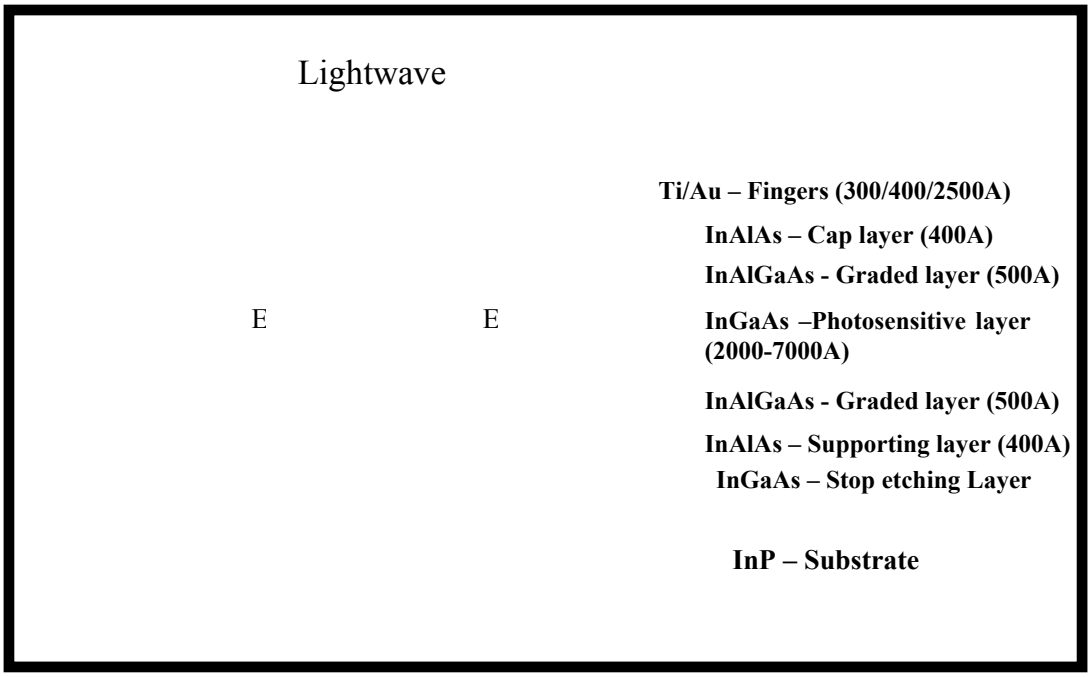

Figure 5.2.2.2. Side view of MSM PD.

5.2.3. Calibration Structures: Impedance Standard Substrate (ISS)

The fabrication of calibration structure includes negative photolithography and e-beam evaporation. First, to make a 50 Ω load, Ni/Cr (2000 Å) is deposited onto a substrate that has on-wafer or thin-film MDM PDs using Ni/Cr. The sheet resistance of Ni/Cr resistor is about 10 to 400 Ωdepending on the thickness of Ni/Cr. After that step, Ti/Au probe pads are e-beam deposited onto the Ni/Cr resistor, as shown in Fig. 5.2.3.1. To make the exact 50 Ω load, laser-trimming is performed on the original Ni/Cr resistors. Other calibration structures such as open, short, thru, and lines except load can be made through metal deposition procedure [42].

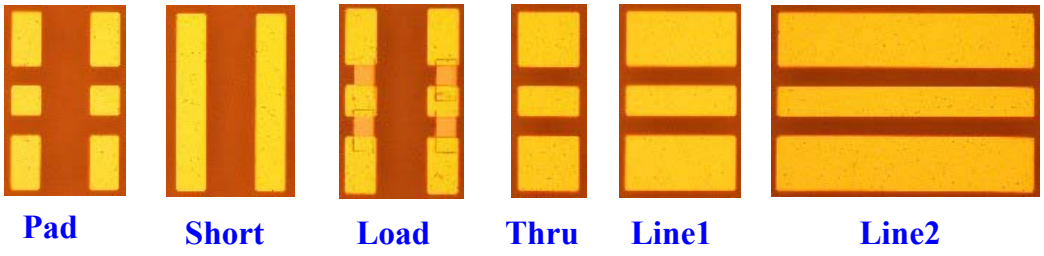

Figure 5.2.3.1. The fabricated calibration structures: open, short, load, thru, and lines.

5.3. Calibration

The advancement of high-speed integrated circuit (IC) design and processes was hampered by an inability to measure and characterize high-frequency characteristic of IC and its elements. On-wafer measurements make it possible and improve the development and production process by replacing the costly packaging for testing. The microwave wafer probing techniques are a key technology for the advanced high-speed silicon (Si) and gallium arsenide (GaAs) integrated circuits and devices. In order to acquire exact measured data, calibration is the most important step in advance [43].

Calibration enhances an accuracy of the measured data and effectively removes the system environment errors that cause uncertainty in measuring a device under test (DUT). These imperfections not only include the non-ideal nature of cables and probes, but also the internal characteristics of the vector network analyzer (VNA) itself. Calibration usually has been considered as a procedure that has to be done once a year to keep the instrument operating within certain errors. This is true for DC and low-frequency range, but this is not true for high-frequency measurements, which are

extremely sensitive to small changes of environments such as small wear of connectors and small bending of cables. As a result calibration must be done right before each set of measurements. The main purpose of the calibration is defining exactly where the measurement system ends and the DUT begins [44-48].

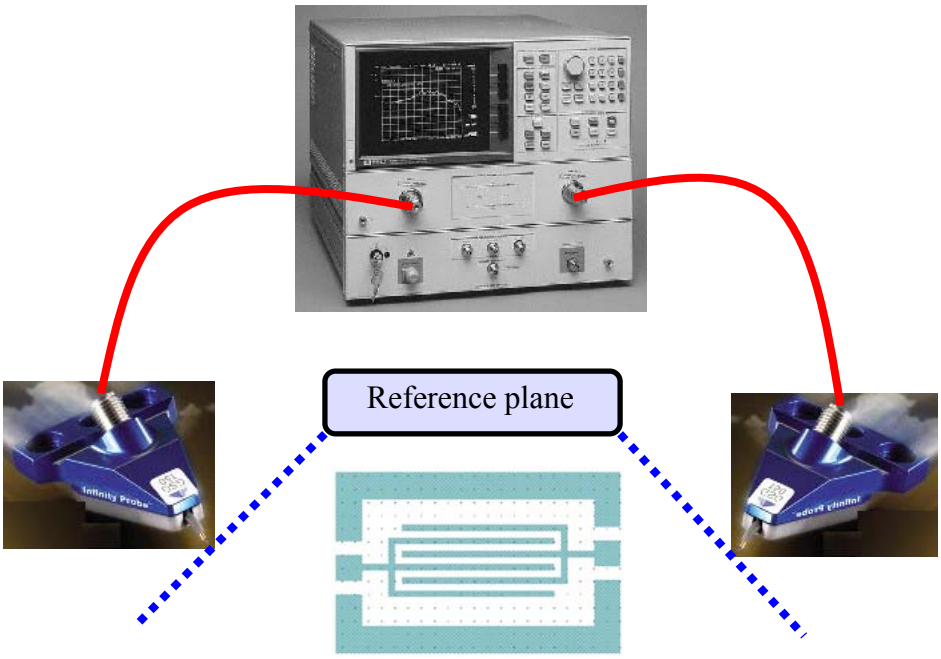

Figure 5.3.1. The reference (calibration) plane.

This boundary is known as the “reference plane” of the measurement and will often be located at the end of the probe tips. The reference plane is shown in Fig.5.3.1.

The degree of accuracy is mainly determined by the completeness of the error model used and the accuracy of the calibration standards. And also, physical placement accuracy of probe tips is important to accuracy of a calibration since the inductance values are dependent on probe placement on the standards.

Calibration can be performed by measuring standard devices that are known or partly known. There are several calibration methods. The five most commonly used calibration techniques are: Short-Open-Load-Thru (SOLT), Short-Open-Reciprocal -Load (SORL), Line-Reflect-Match (LRM), Line-Reflect-Reflect-Match (LRRM), and Thru-Reflect-Line (TRL). Table 5.3.1 shows the summary of calibration methods [49-52].

Table 5.3.1. Summary of calibration methods.

	Zo Reference	**Accuracy**
SOLT	Load	Good
SORL	Load	Good
TRL	Thru	Poor
NIST TRL	Thru	Best
LRM	Load	Good
LRRM	Load	Very Good

Calibration is usually done using commercial impedance standard substrate (ISS) that is provided from some manufacturer such as Cascade Microtech. This commercial calibration kit is quite well designed and optimized but calibration structures are fabricated on different substrate with different thickness and different processing environment. In order to circumvent this limitation, on-wafer calibration standard structures were fabricated on a same substrate of the MSM PDs in this research.

5.3.1. On-wafer Calibration

On-wafer calibration standard structures were fabricated with MSM PDs on the same substrate for exact characterization. Short, open, and load (SOL) calibration was used in this proposed research. Fig. 5.3.1.1 shows the fabricated calibration structures: short, load, and pads for probing. In case of load, NiCr resistors were designed and laser-trimmed to make it 50 Ω. The original value of the load structure was about 30 Ω. Through laser-trimming accurate 50 Ω load was obtained. The calibration results of laser-trimmed/untrimmed load, open, and short are shown in Fig. 5.3.1.2 and Fig. 5.3.1.3. In order to make sure the uniformity of the laser-trimmed load with respect to frequency changes, the load is measured at two different frequency points at 1GHz (49.971 Ω) and 20 GHz (50.010 Ω).

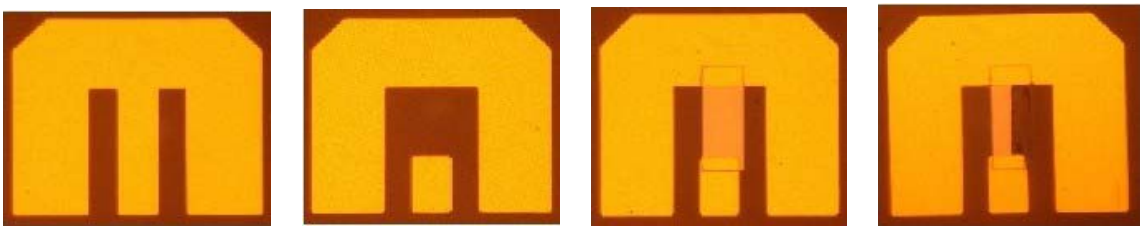

(a) Short (b) Pad (c) The original load (d) The laser-trimmed load

Figure 5.3.1.1. The fabricated calibration structures: short, pad, untrimmed load, and laser-trimmed load.

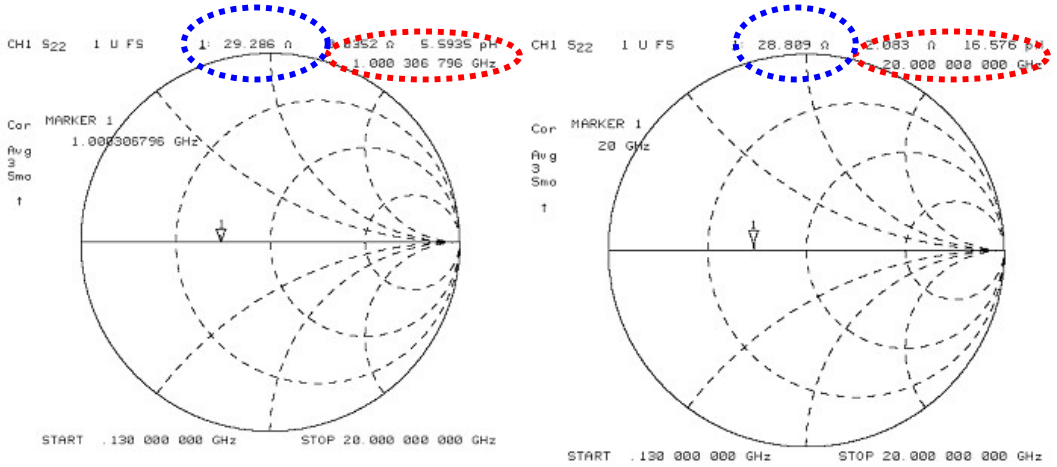

(a) Untrimmed 29 Ω load at 1 GHz and 20 GHz.

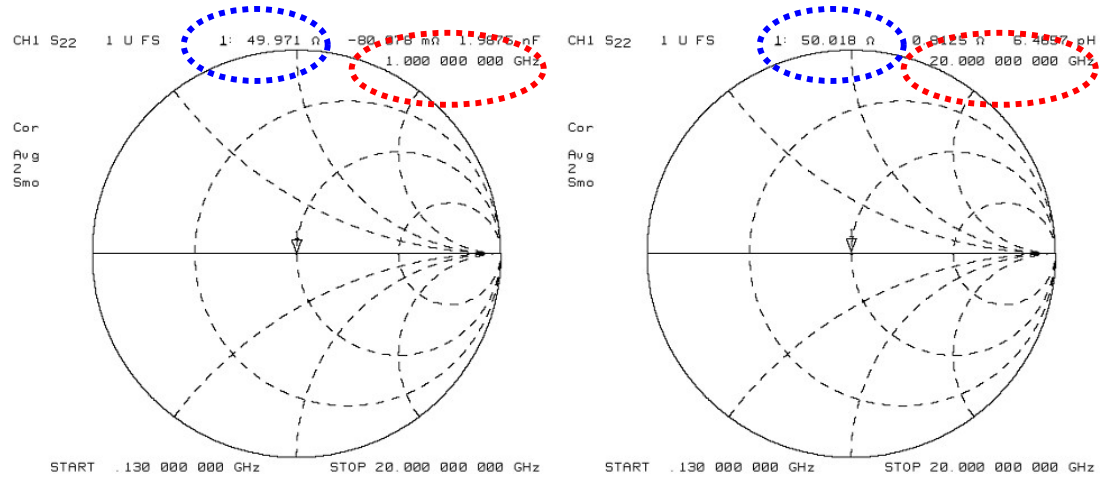

(b) Laser-trimmed 50 Ω load at 1 GHz and 20 GHz.

Figure 5.3.1.2. The results of original 29 Ω load and laser-trimmed 50 Ω load.

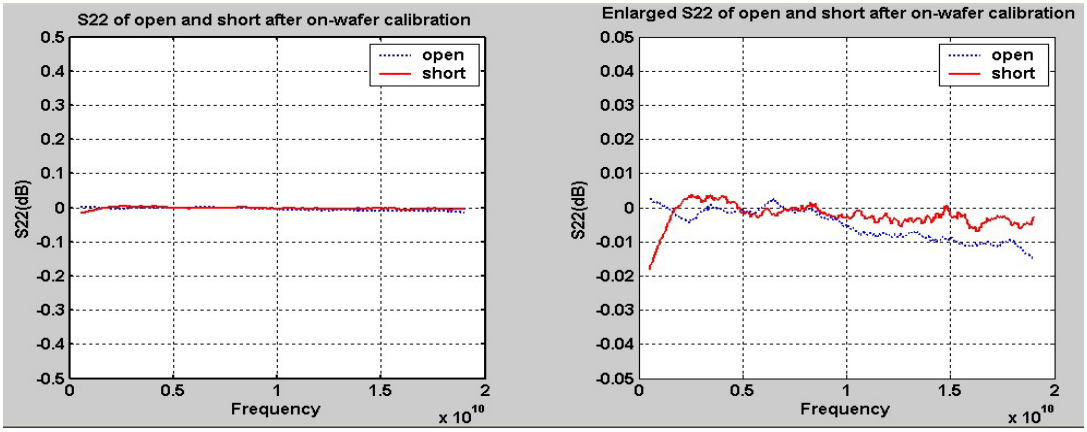

Figure 5.3.1.3. S22 of open and short calibration structures after calibration.

5.3.2. Verification of the Calibration

Calibration results should be verified to guarantee an accurate measurement after calibration. The following tips can be used for the verification [53-55].

- The open measurement does not have any contact issues and can be used as a reference.
- The measurement of the short standard will show an ideally 180 degree phase shift.
- The measured reflections will normally be reduced by more than 10 dB when the load is in contact.
- The reflection coefficient of the long open circuit should exhibit a smooth monotonic inward spiral on the Smith chart.

- The thru line standard is a useful verification element for an SOLR calibration (Excess line length beyond the probe contacts will act like capacitive stubs that resulting in increased attenuation at higher frequencies).
- Probe tip alignment patterns are useful for accurate alignments on the calibration elements
- An oxide layer will grow on the pad surface when left in air. This leads to possible contact resistance and variable contact resistance as time goes on. Multiple touch-downs are required to remove the oxide layer from the pad. A tungsten tips are superior because it is very hard and rugged, so it performs a self-cleaning action when contact is made on to the bare substrate to clean the oxide.

5.4. Measurements

5.4.1. DC Measurements

The dark current, the photocurrent, and the responsivity of the MSM PDs were measured in the DC measurements. A Keithley 236 source measure unit (SMU) was used to measure the current-voltage (I-V) characteristic of the MSM photodetectors. For the illumination, a single mode lensed fiber that has minimum spot size of 5 μ m was used by vertical illumination at wavelengths of 1.3 μ m and 1.55 μm [65-66].

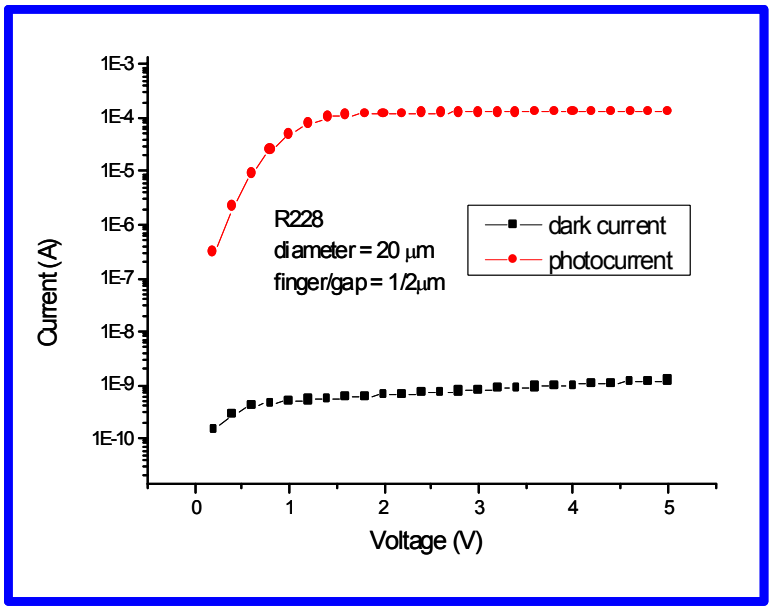

Figure 5.4.1.1. Dark current and photocurrent of the MSM PD.

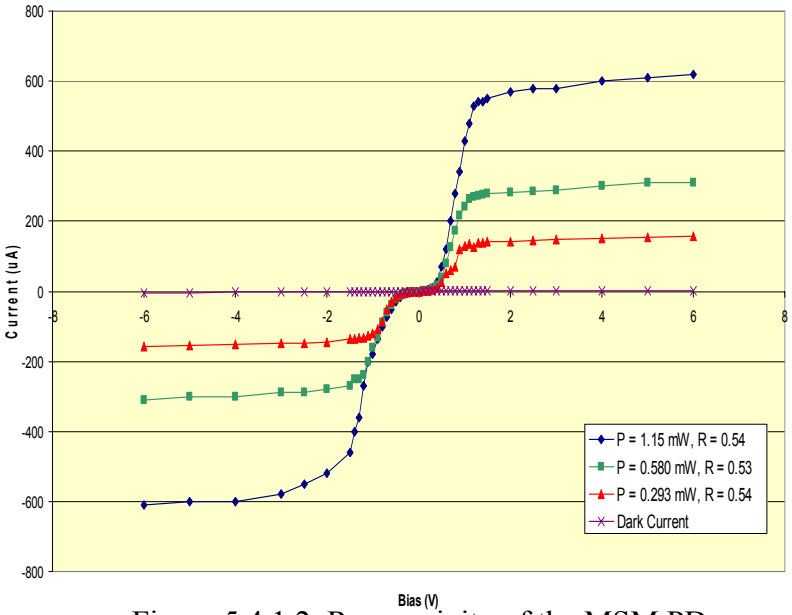

Figure 5.4.1.2. Responsivity of the MSM PD.

5.4.2. S-parameters Measurement

For high-frequency measurements, a lightwave component analyzer (LCA) or vector network analyzer (VNA) was used in conjunction with a Cascade Microtech probe station and ground-signal-ground (GSG) configuration microwave probes. S-parameters were obtained as a measured data. Single mode lensed fiber was used for the better coupling of light to the MSM PD because misalignment of the fiber to the MSM PDs will result in power loss and significant frequency response degradation.

S-parameters are just one type of network representation used for linear, small-signal, AC analysis. S-parameters can be used for only a single mode of propagation at device terminals is assumed. Situations that violate this assumption, such as using waveguides that can propagate multiple modes, radiation, or parasitic coupling between networks other than at the device terminals, are not properly handled [10].

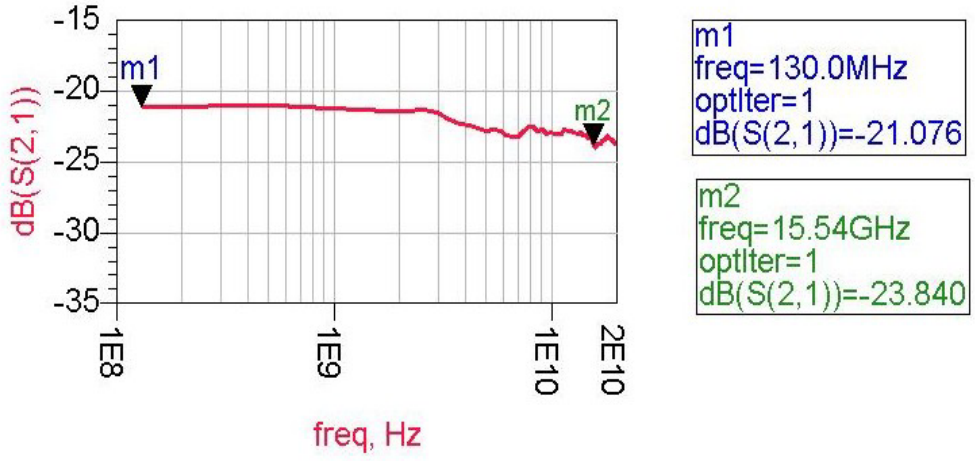

Figure 5.4.2.1. Optical to electrical (O/E) response or S21 of a thin film MSM PD (40 um/1 um /1 um) at 5V.

Data were gathered for each of the test structures at over 401 frequency points between 130 MHz and 20 GHz, and data were stored with the aid of computer data acquisition software and equipment. Fig. 5.4.2.1 shows a Optical to electrical (O/E) response or S21 of a thin film I-MSM PD.

Figure 5.4.2.2. S-parameters test setup: Lightwave component Analyzer (130MHz~20GHz), RF cables (40GHz), Cascade Microtech probe station, Ground-signal-ground (GSG) configuration microwave probes (40GHz), Lightwave probes with lensed single mode fiber (diameter: 9 um), GPIB data acquisition with PC, Laser cutter, HP BERT

5.4.3. Impulse Response Measurement

In the time domain, the impulse response of the DUT was measured. As a light source, a 500 fsec IMRA laser was used in conjunction with a 50 GHz sampling oscilloscope. The optical source was divided into two signals: one is a trigger signal into a slow photodetector and the other is a optical source to a DUT. The results of impulse and frequency response with respect to bias voltage are shown in Fig. 5.4.3.1.

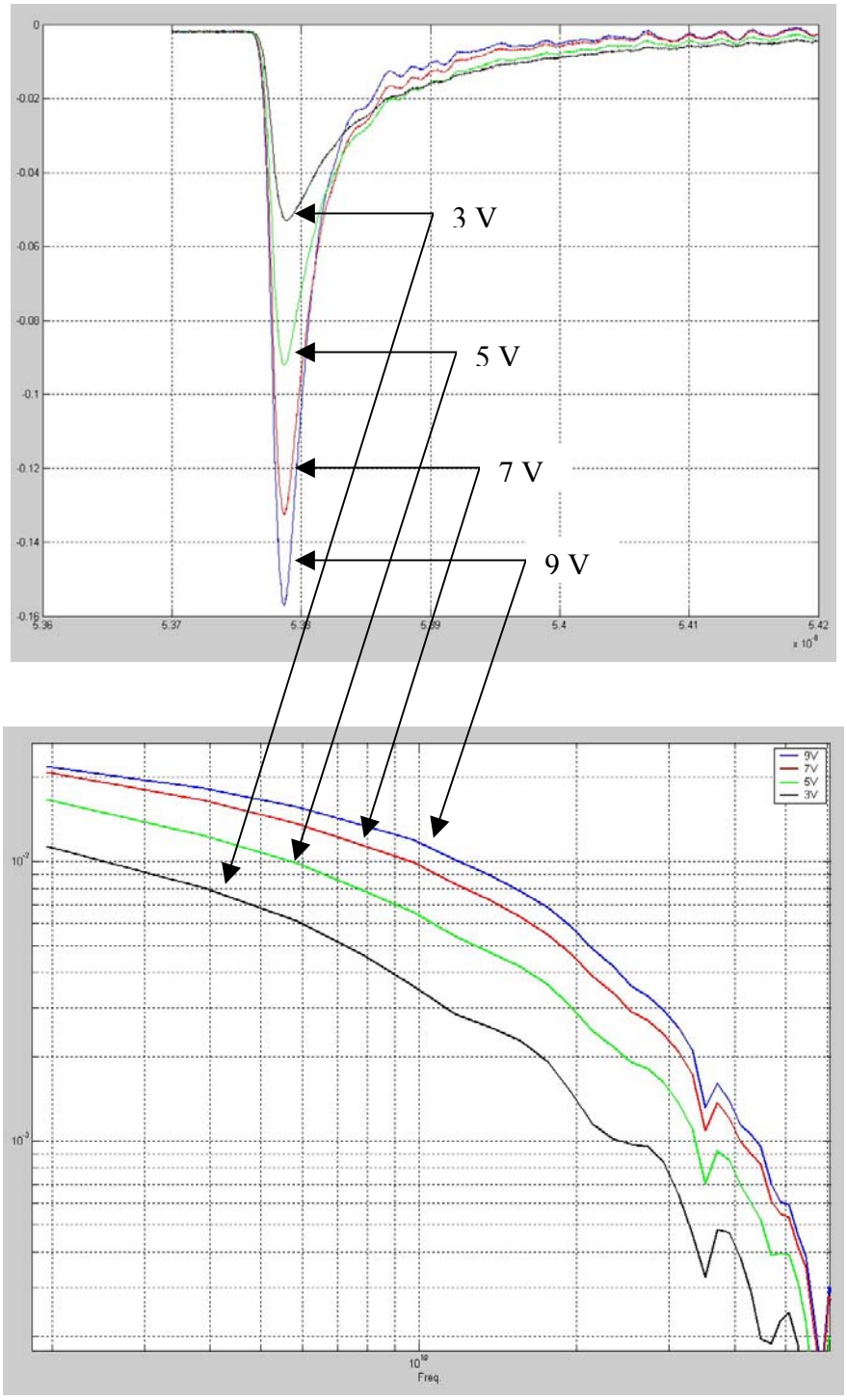

Figure 5.4.3.1. The impulse and frequency responses for 80/1/1 um MSM PD with respect to bias voltage.

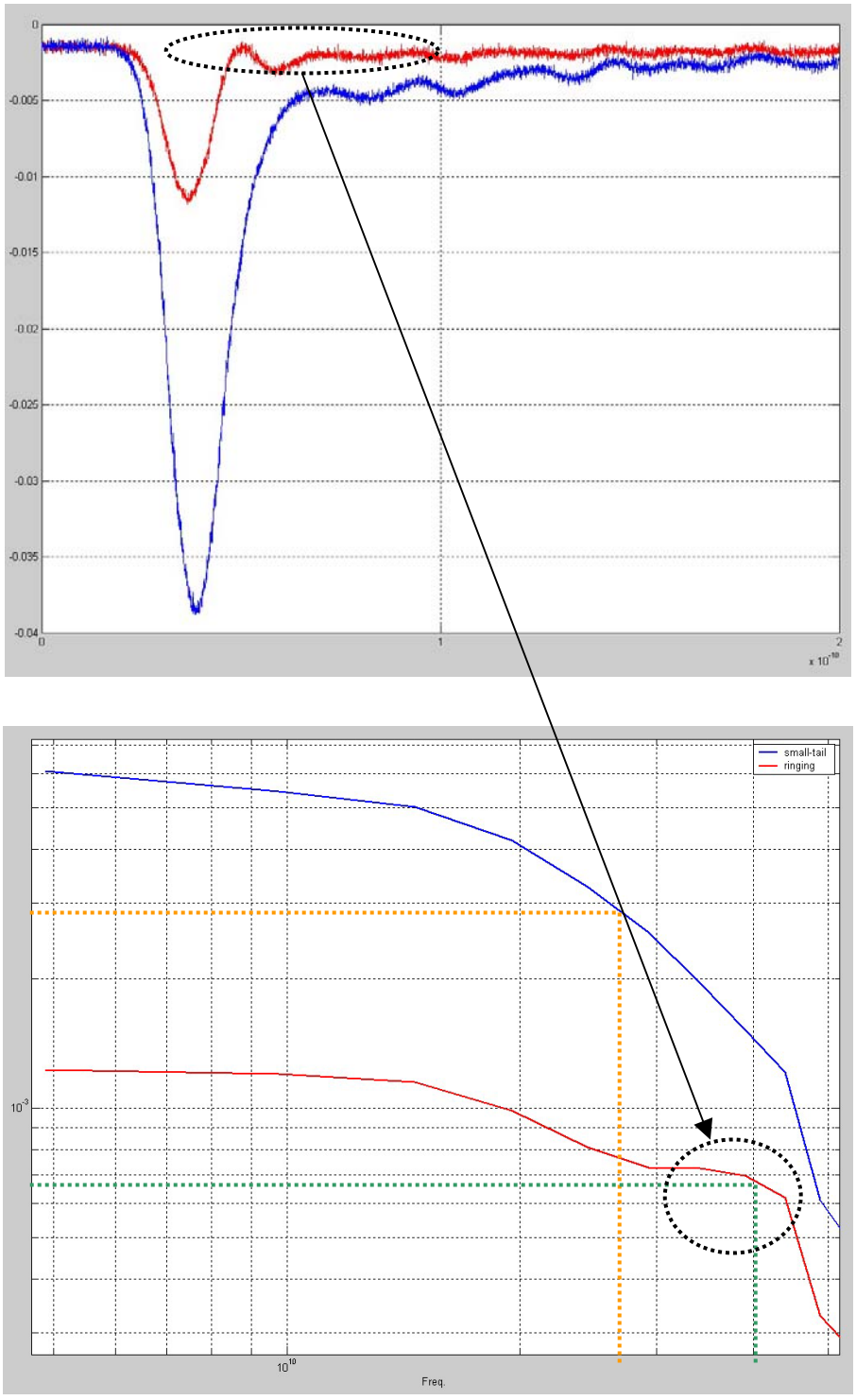

Figure 5.4.3.2. Two impulse responses: tail and ringing, and their frequency response.

There are two main cases: one is big tail without ringing and the other is small tail with ringing as shown in Fig. 5.4.3.2. The main causes of tail are electron hole pair (EHP) generations outside the detection area. Those EHPs are accumulated or trapped at defected place and cause capacitive component in the MSM photodetectors.

Long tail component in the impulse response causes big slope in the frequency response but ringing in the impulse response causes peaking in the frequency response. This peaking mainly due to inductance component in the MSM photodetectors and extends bandwidth as shown in Fig. 5.4.3.2.

5.5. Deembedding techniques

In the modeling process, parasitic effects in the measurement environment have a big impact on a DUT modeling and make characterization of the DUT difficult. These parasitic effects come from probe pads, interconnections, and substrate resistance. These influences of parasitics must be subtracted or deembedded from the measurements to generate the DUT model. Deembedding is a correction procedure that extracts actual DUT parameters from its measurement environment. Fig. 5.5.1 shows the deembedding plane and reference plane. As the size of the DUT shrinks, these parasitics have a significant impact on DUT modeling since the parasitic effects of probe pads and interconnections are comparable to DUT parameters [57]. Fig. 5.5.2 shows test structures for deembedding.

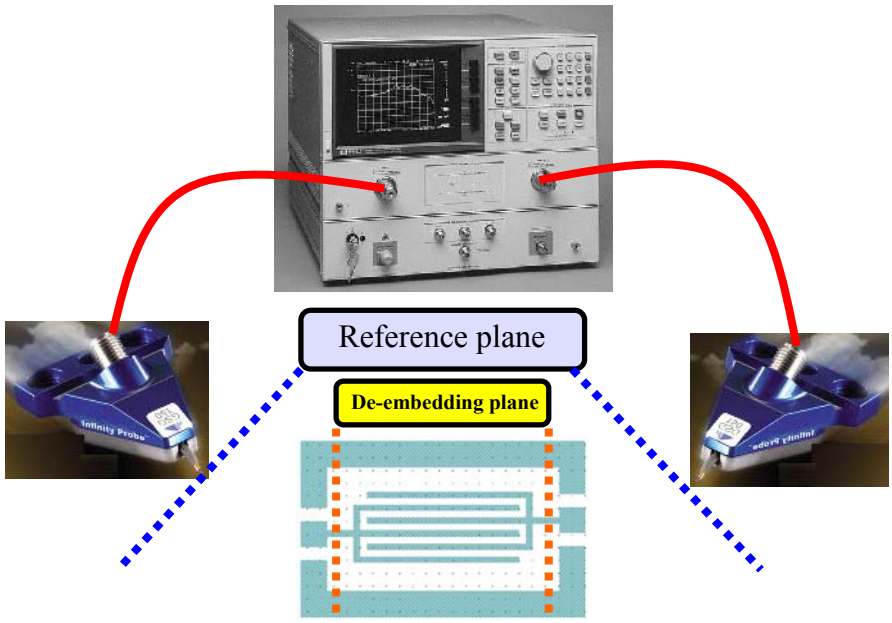

Figure 5.5.1. The reference plane and deembedding plane.

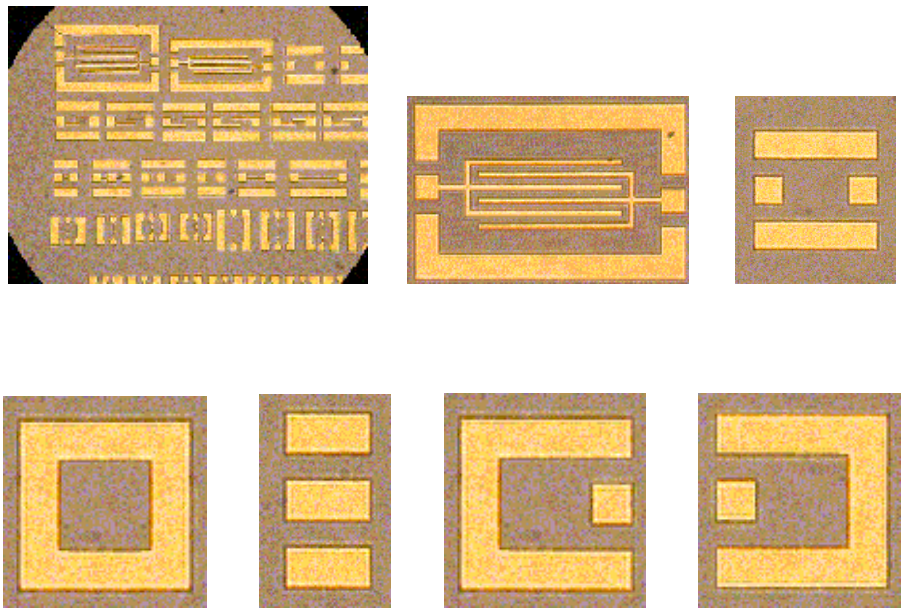

Figure 5.5.2. Test-bed, DUT, pad, short, thru, short1, and short2.

5.5.1. One-step Deembedding Method

The most dominant parasitics are in parallel with the DUT and can be modeled as capacitance with resistance. In this method two measurements are done to obtain DUT parameters: "Pad" and "DUT on pad." Figure 5.5.1.1 shows a two port network: "Pad" and "DUT on pad." Figure 5.5.1.2 shows comparison of y-parameters: "Pad," "DUT," and "DUT on pad." Deembedding procedure is described in detail below [57].

(1) S-parameters Measurement: "$[S_p]$" and "$[S_t]$" that are S-parameters of "Pad" and "Total (DUT on pad)", respectively.

(2) Changing to Y-parameters: "$[Y_p]$" and "$[Y_t]$."

(3) From Fig. 5.5.1.1: $$[Y_p]=\begin{bmatrix} y_{11p} & y_{12p} \\ y_{21p} & y_{22p} \end{bmatrix}=\begin{bmatrix} G1+G3 & -G3 \\ -G3 & G2+G3 \end{bmatrix}. \quad (5.5.1.1)$$

(4) Subtraction: $$[Y_{DUT}]=[Y_t]-[Y_p]. \quad (5.5.1.2)$$

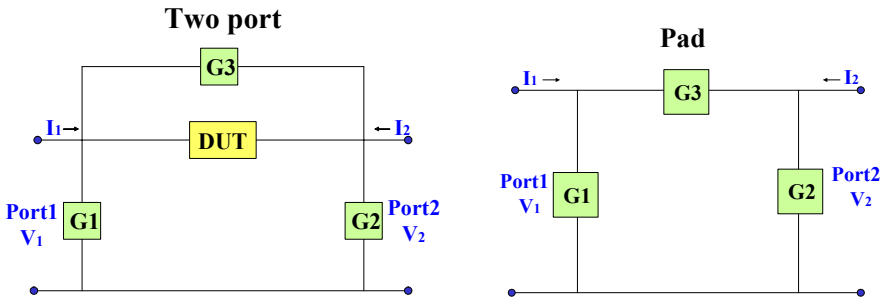

Figure 5.5.1.1. Two port network "DUT on pad" and "Pad."

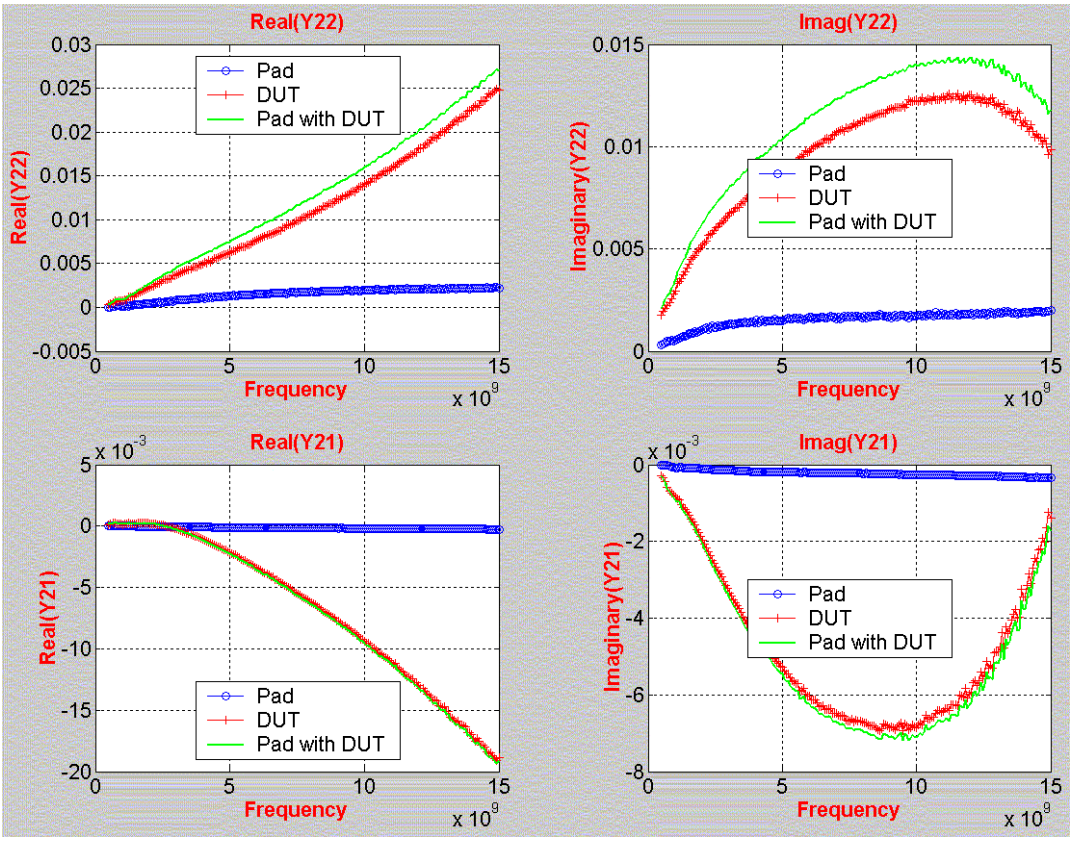

Figure 5.5.1.2. Y-parameters of "Pad," "DUT," and "DUT on pad."

5.5.2. Two-step Deembedding Method

The one-step deembedding procedure assumes that series parasitics are negligible compared to parallel parasitics but in case of low impedance and high transconductance devices, these series effect must be taken into account. In order to perform the two-step deembedding, one more dummy test structure is needed: "Short" which can determine interconnect line's behavior such as loss and phase shift. In this method three measurements are done to obtain DUT parameters: "Pad," "Short," and "DUT on pad."

Figure 5.5.2.1 shows two port T-network models. Deembedding procedure is described in detail below [58]:

(1) S-parameters Measurement: "$[S_p]$," "$[S_s]$," and "$[S_t]$" that are S-parameters of "Pad," "Short," and "Total (DUT on pad)," respectively.

(2) Changing to Y-parameters: "$[Y_p]$," "$[Y_s]$," and "$[Y_t]$"

$$[Y_p] = \begin{bmatrix} y_{11p} & y_{12p} \\ y_{21p} & y_{22p} \end{bmatrix} = \begin{bmatrix} G1+G3 & -G3 \\ -G3 & G2+G3 \end{bmatrix}. \tag{5.5.2.1}$$

(3) Subtraction 1: $\left([Y_s]-[Y_p]\right)^{-1} = \begin{bmatrix} H1 & 0 \\ 0 & H2 \end{bmatrix}$. (5.5.1.2)

(4) Subtraction 2: $[Y_{DUT}] = \left(\left([Y_t]-[Y_p]\right)^{-1} - \left([Y_s]-[Y_p]\right)^{-1}\right)^{-1}$. (5.5.1.3)

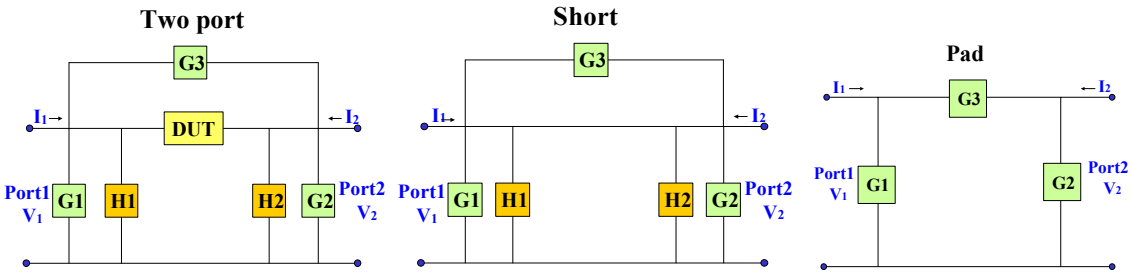

Figure 5.5.2.1. Two port network "DUT on pad," "Short," and "Pad."

5.5.3. Three-step Deembedding Method

The two-step deembedding technique is not a sufficient method for accurate modeling of DUT because it ignores the series interconnection between pad and DUT. These parasitics can be removed using "Thru" structure. In order to perform three-step deembedding procedure, four dummy test structures are needed: "Open," "Short1," "Short2," and "Thru." Figure 5.5.3.1 shows two-port network models.

This method includes three steps. First, subtracting the y-parameter of the open which is shunting the input and output ports. Second, subtracting the series z-parameters derived from measurement of the shorts and thru structures. Finally, subtracting the coupling capacitance between the input and output ports. De-embedding procedure is described in detail below [59-60]:

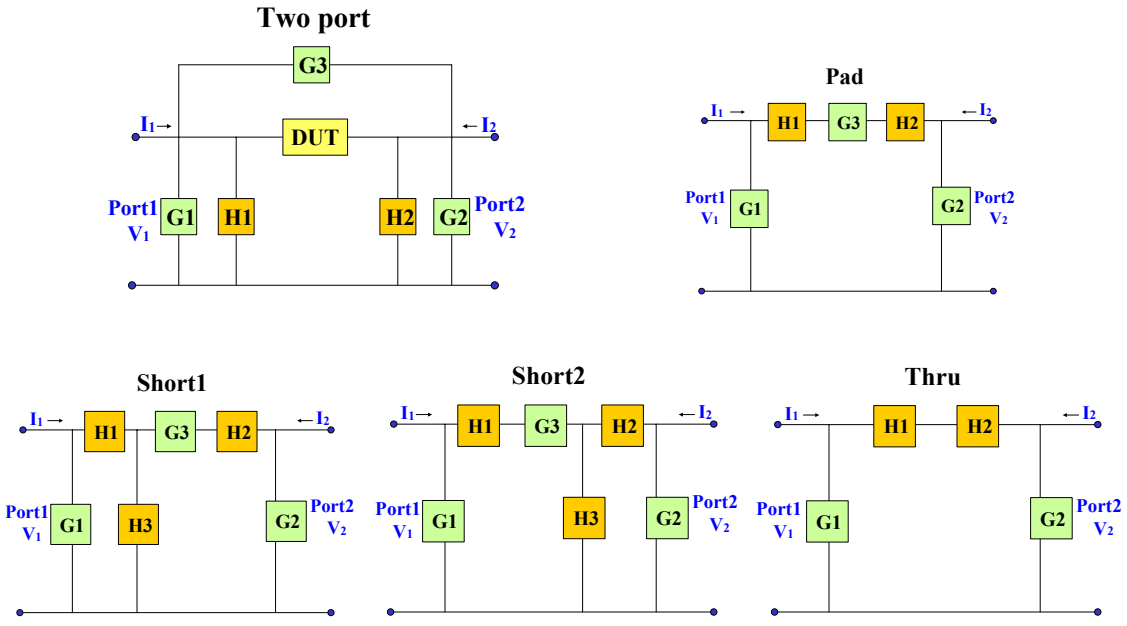

Figure 5.5.3.1. Two-port network: "DUT on pad," "Pad," and "Short1," "Short2," and "Thru."

(1) S-parameters measurement: "[S_p]," "[S_{s1}]," "[S_{s2}]," "[S_{th}]," and "[S_t]" that are S-parameters of "Pad," "Short1," "Short2," "Thru," and "Total, " respectively.

(2) Changing to Y-parameters: "[Y_p]," "[Y_{s1}]," "[Y_{s2}]," "[Y_{th}]," and "[Y_t]."

$$\left[Y_p\right]=\begin{bmatrix} y_{11p} & y_{12p} \\ y_{21p} & y_{22p} \end{bmatrix},\ \left[Y_{th}\right]=\begin{bmatrix} y_{11th} & y_{12th} \\ y_{21th} & y_{22th} \end{bmatrix}$$
$$\left[Y_{s1}\right]=\begin{bmatrix} y_{11s1} & y_{12s1} \\ y_{21s1} & y_{22s1} \end{bmatrix},\ \left[Y_{s2}\right]=\begin{bmatrix} y_{11s2} & y_{12s2} \\ y_{21s2} & y_{22s2} \end{bmatrix}. \tag{5.5.3.1}$$

(3) From "Pad":

$$\frac{-1}{y_{12p}} = H_1 + H_2 + \frac{1}{G_3} = \frac{-1}{y_{12th}} + \frac{1}{G_3} \Longrightarrow G_3 = \left(\frac{1}{y_{12th}} - \frac{1}{y_{12p}}\right)^{-1}$$
$$y_{11p} = G_1 + \frac{1}{H_1 + H_2 + \frac{1}{G_3}} = G_1 - y_{12p} \Longrightarrow G_1 = y_{11p} + y_{12p} \quad . \tag{5.5.3.2}$$
$$y_{22p} = G_2 + \frac{1}{H_1 + H_2 + \frac{1}{G_3}} = G_2 - y_{12p} \Longrightarrow G_2 = y_{22p} + y_{12p}$$

(4) From "Thru," "short1," and "Short2":

$$-y_{12th} = \frac{1}{H_1 + H_2} \quad , \ y_{11s1} = G_1 + \frac{1}{H_1 + H_3} \quad , \ y_{22s2} = G_2 + \frac{1}{H_2 + H_3}$$

$$H_1 + H_2 + H_3 = \frac{1}{2}\left(\frac{-1}{y_{12th}} + \frac{1}{y_{11s1} - G_1} + \frac{1}{y_{22s2} - G_2}\right) \tag{5.5.3.3}$$

$$H_1 = \frac{1}{2}\left(\frac{-1}{y_{12th}} + \frac{1}{y_{11s1} - G_1} - \frac{1}{y_{22s2} - G_2}\right)$$

$$H_2 = \frac{1}{2}\left(\frac{-1}{y_{12th}} - \frac{1}{y_{11s1} - G_1} + \frac{1}{y_{22s2} - G_2}\right)$$

$$H_3 = \frac{1}{2}\left(\frac{1}{y_{12th}} + \frac{1}{y_{11s1} - G_1} + \frac{1}{y_{22s2} - G_2}\right).$$

(5) From above results:

$$[Y_A] = [Y_{meas}] - \begin{bmatrix} G_1 & 0 \\ 0 & G_2 \end{bmatrix}, Y_A = \frac{1}{Z_A}$$

$$[Z_B] = [Z_A] - \begin{bmatrix} H_1 + H_3 & H_3 \\ H_3 & H_2 + H_3 \end{bmatrix}, Y_B = \frac{1}{Z_B} \qquad (5.5.3.4)$$

$$[Y_{DUT}] = [Y_B] - \begin{bmatrix} G_3 & -G_3 \\ -G_3 & G_3 \end{bmatrix}.$$

5.5.4. Cascade Deembedding Method

The connection between pad and DUT are cascade, so ABCD parameters can be applied to the deembedding procedure. One-port ABCD parameters of pad can be obtained from the measured data [61-62].

$$y_{11\_pad} = \frac{1}{Z_0}\frac{(1 - s_{11\_pad})}{(1 + s_{11\_pad})}, \begin{bmatrix} A_{pad} & B_{pad} \\ C_{pad} & D_{pad} \end{bmatrix} = \begin{bmatrix} 1 & 0 \\ y_{11\_pad} & 1 \end{bmatrix} \qquad (5.5.4.1)$$

The total ABCD parameters of pad and DUT can be easily determined from the measured s-parameters and can be expressed as:

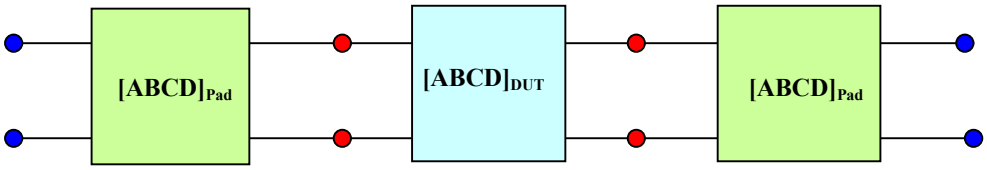

Figure 5.5.4.1. Two port network and cascade connection of pads and DUT.

$$A_{pad+DUT} = \frac{(1+s_{11\_pad+DUT})(1-s_{22\_pad+DUT}) + s_{12\_pad+DUT}s_{21\_pad+DUT}}{2s_{21\_pad+DUT}}$$

$$B_{pad+DUT} = Z_0 \frac{(1+s_{11\_pad+DUT})(1+s_{22\_pad+DUT}) - s_{12\_pad+DUT}s_{21\_pad+DUT}}{2s_{21\_pad+DUT}}$$

$$C_{pad+DUT} = \frac{1}{Z_0} \frac{(1-s_{11\_pad+DUT})(1-s_{22\_pad+DUT}) - s_{12\_pad+DUT}s_{21\_pad+DUT}}{2s_{21\_pad+DUT}} \quad (5.5.4.2)$$

$$D_{pad+DUT} = \frac{(1-s_{11\_pad+DUT})(1+s_{22\_pad+DUT}) + s_{12\_pad+DUT}s_{21\_pad+DUT}}{2s_{21\_pad+DUT}}.$$

The relationship of ABCD-parameters between the “pad,” “DUT,” and “Pad +DUT” can be expressed as:

$$\begin{bmatrix} A_{DUT} & B_{DUT} \\ C_{DUT} & D_{DUT} \end{bmatrix} = \begin{bmatrix} A_{pad} & B_{pad} \\ C_{pad} & D_{pad} \end{bmatrix}^{-1} \begin{bmatrix} A_{pad+DUT} & B_{pad+DUT} \\ C_{pad+DUT} & D_{pad+DUT} \end{bmatrix} \begin{bmatrix} A_{pad} & B_{pad} \\ C_{pad} & D_{pad} \end{bmatrix}^{-1}. \quad (5.5.4.3)$$

From the deembedded ABCD-parameters DUT parameters can be calculated by

$$s_{11\_DUT} = \frac{A_{DUT} + B_{DUT}/Z_0 - C_{DUT}Z_0 - D_{DUT}}{A_{DUT} + B_{DUT}/Z_0 + C_{DUT}Z_0 + D_{DUT}}$$

$$s_{12\_DUT} = \frac{2(A_{DUT}D_{DUT} - B_{DUT}C_{DUT})}{A_{DUT} + B_{DUT}/Z_0 + C_{DUT}Z_0 + D_{DUT}} \quad (5.5.4.4)$$

$$s_{21\_DUT} = \frac{2}{A_{DUT} + B_{DUT}/Z_0 + C_{DUT}Z_0 + D_{DUT}}$$

$$s_{22\_DUT} = \frac{-A_{DUT} + B_{DUT}/Z_0 - C_{DUT}Z_0 + D_{DUT}}{A_{DUT} + B_{DUT}/Z_0 + C_{DUT}Z_0 + D_{DUT}}.$$

5.5.5. One port deembedding technique

MSM PDs have an optical input port and electrical output port as shown in Fig. 5.5.5.1. In this section, a one port deembedding technique is used to deembed the parasitic effects of pad. These deembedded S-parameters will be used for the initial values guessing of model parameters. Figure 5.5.5.2 shows signal flow graph and three measurements: one port pad, two port pad, and DUT on pad. The DUT parameters can be extracted using signal flow graph and decomposition rules. The parasitic effect of the pad and extracted DUT Y-parameters are shown in Figure 5.5.5.3 [63-64].

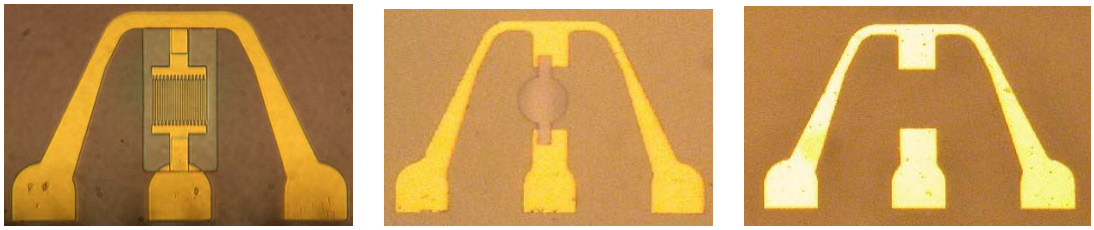

Figure 5.5.5.1. Microphotographs of an on-wafer square MSM PD (50/1/1 μm), an I-MSM PD (40/1/1 μm), and a probe pad.

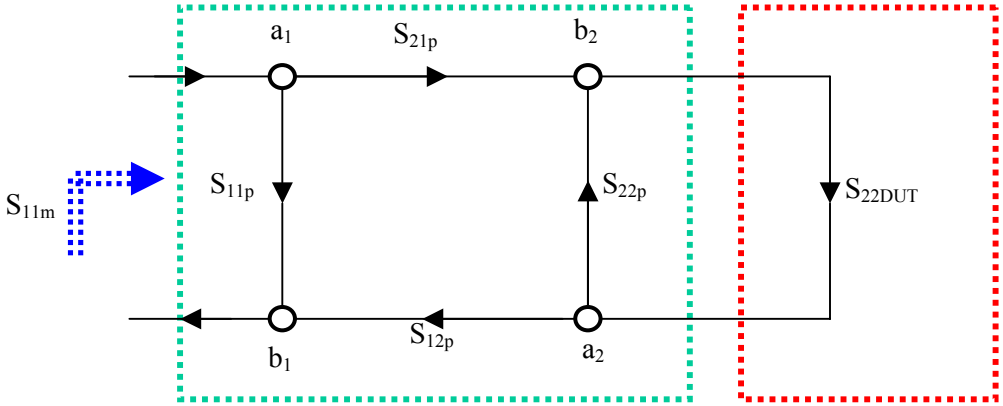

(a) Signal flow graph of one port measurement.

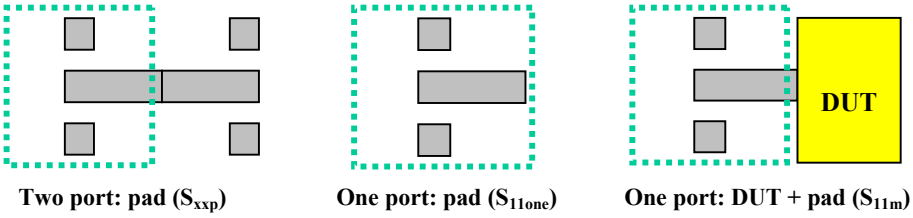

(b) Three measurements: one port pad, two port pad, and DUT on pad.

Figure 5.5.5.2. Signal flow graph and three measurements for one port deembedding.

$$S_{22DUT} = \frac{S_{11p} - S_{11m}}{(S_{11p}S_{22p} - S_{21p}S_{12p}) - S_{22p}S_{11m}} - S_{11one} \qquad (5.5.5.1)$$

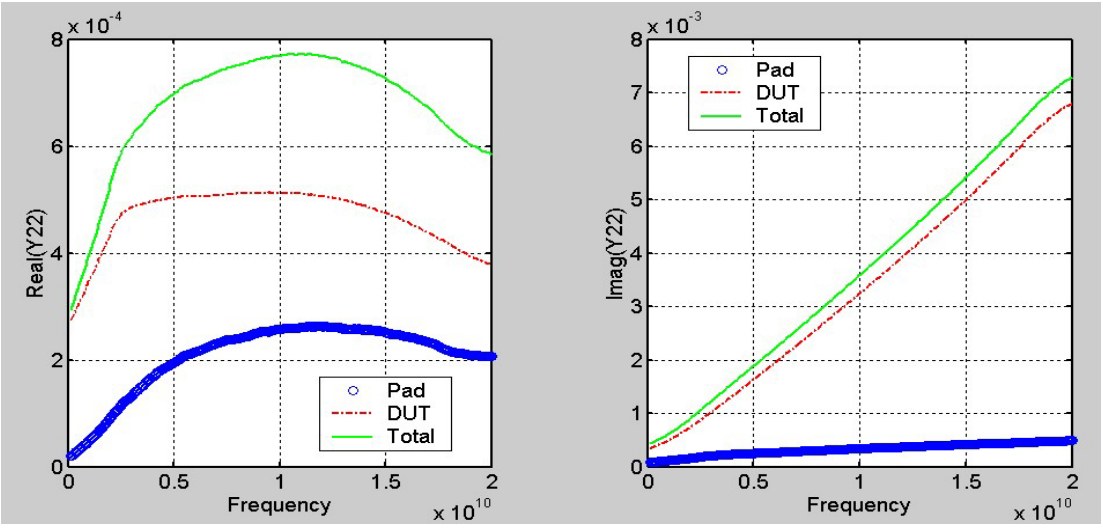

Figure 5.5.5.3. Y-parameters: pad, DUT, and total (DUT on pad).

CHAPTER VI

MSM PHOTODETECTOR MODELING

6.1. Introduction

Photodetectors (PDs) are an important active device in optoelectronic integrated circuits (OEICs). Especially, metal-semiconductor-metal photodiodes are attractive candidate due to their low capacitance per unit area compared to PIN photodetectors and the ease of monolithic integration with field effect transistors (FETs) for shorter haul interconnections where circuit (e.g. transimpedance amplifier) noise may be the dominant noise in optical receivers. Those characteristics are mainly determined by the physical structures of the MSM PDs such as finger width and spacing, detection area size, thickness of active material, bias voltage, light intensity, and wavelength [3-4]. Inverted-MSM PDs (I-MSM PDs), which are thin film MSM PDs with the fingers on the bottom of the device, have demonstrated higher responsivities compared to conventional MSM PDs while maintaining small capacitance per unit area, low dark current (~nA), and high speed.

A great deal of research has been done on the MSM PD modeling during the past decade and various modeling methods have been employed for accurate and fast modeling. However, the modeling of MSM PDs and I-MSM PDs for insertion into

conventional circuit simulators for integrated PD/TIA co-design has not been reported. Currently, this is not possible, as models of photodetectors that accurately reflect geometric changes to the device are not available in circuit simulator (e.g., HSPICE) format. The objective of research is to find an accurate, scalable, frequency-dependent, and wide-band equivalent circuit-level model of metal-semiconductor-metal photodetectors for co-optimization with preamplifier circuitry using the optimization routines in widely used simulators such as HSPICE and ADS. This approach circumvents the inconvenient, iterative interface between a photonic device simulator and a circuit design tool. The attractive feature of this technique is that it enables the designer to optimize optoelectronic devices and active devices simultaneously. Another feature of the proposed research is that it can also consider the parasitic effects of contacts and bonding pad in the circuit model [32].

6.2. Modeling Methodology

Modeling methodology of device usually falls into three categories: equation-based, measurement-based and electromagnetic full wave simulation-based methods. Ideally, an equation-based method is used because it is fast to simulate and allows variation of parameters to perform design. However, equation-based methods are usually unable to include processing effects, such as uneven metal deposition or roughness in width and surface of conductors, jagged edges, non-uniform dielectric thickness, processing fluctuations, and non-ideal material properties. Thus, by the time the model is

ready, the device process will have changed, making the model inappropriate. This leads to a continuing problem of obsolescence and inaccuracy with equation-based models.

Given a sufficiently accurate material database, finite element derived simulation methods can predict the behavior of many devices and structures. However, the simulations are usually very slow when compared to equation-based simulations. For example, the Avant Taurus-Medici was used for MSM photodetector simulations.

However, only unit cell can be simulated because of long simulation time (more than 5 hours for a simple unit cell with a SUN ultra 10 workstation that has 800 MHz CPU and 1024 M bytes memory) and unavailability of accurate material parameters. Those tools only can be used for trend prediction of structures not for accurate responses of device. Fig. 6.2.1 shows an impulse and frequency response of 1/2 um of finger width and spacing MSM PD unit cell. The reason of long simulation time is that finite element methods break down a large and complex structure into a huge number of simple elements by segmenting the structure and applying the relevant boundary conditions or external excitations to the appropriate elements. To characterize it, a basis function is applied on its boundaries, which is continuous within it and between adjacent elements. As the element sizes become smaller, more accurate results can be obtained. Usually, a large number of elements are needed for most nontrivial structures and for a three-dimensional structure, and the complexity of the problem increases dramatically. This result in enormous computer memory needs, high usage of CPU, and computation time even with the fastest workstations available today. This is a problem for complex devices or if statistical process fluctuations are important, as in these cases the simulation time

can exceed the fabrication time for devices, making simulations useless. This brings us to measurement-based methodology.

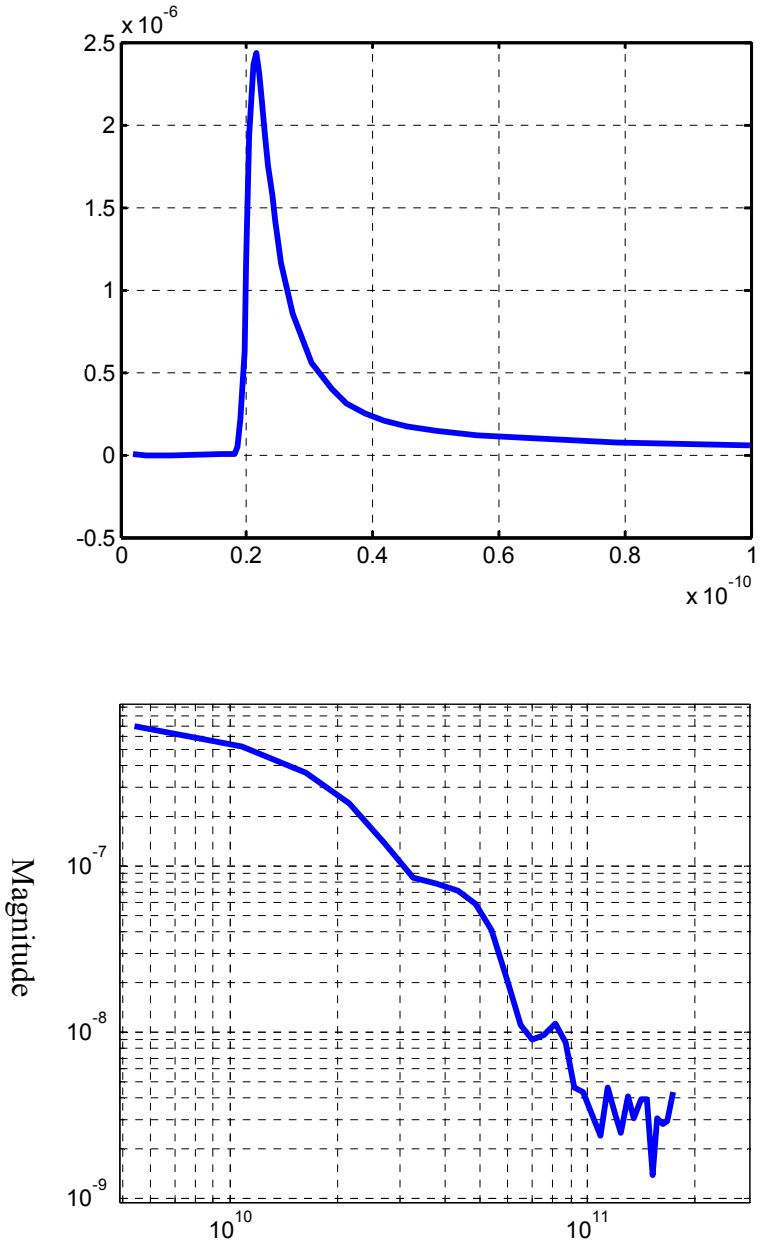

Figure 6.2.1. Simulated impulse and frequency response of unit cell using Avant Taurus-Medici.

In this case, a set of data is measured for a device and a set of equations is fitted to the data. Often, the equations are in the form of lumped elements or a circuit, built up from other equation-based model primitives, such as those available in circuit simulators like SPICE. This form of model is widely used in industry for optoelectronic and RF devices. The methodology overcomes the inaccuracy of the equation-based model by being measurement-based and overcomes the slow simulation time problem of finite-element methods by yielding compact models. In fact, users can incorporate statistical information in the models by repeatedly fabricating test structures and building many different models [4, 74].

A measurement-based modeling methodology is developed and demonstrated experimentally in this chapter that allows measurement of photodetectors at frequencies into the tens of GHz, yielding models that predict the behavior of different dimensioned photodetectors.

The fundamental idea of this modeling methodology is that each target structure can be partitioned into small pieces of geometrical elements or partial elements (PEs). If we can develop models of these partial elements and their interactions, models of complex structures that are constructed from these basic elements could be found by connecting together these partial elements. The equivalent circuits, measurement-based partial element equivalent circuit (M-PEEC), of the partial elements and their interactions are derived from test structures and measurements, and thus automatically take into account effects of processing fluctuations and non-ideal material properties that are hard to acquire through equation-based and numerical full wave electromagnetic methods.

This approach circumvents the inconvenient, iterative interface between a photonic device simulator and a circuit design tool. The attractive feature of this technique is that it enables the designer to optimize optoelectronic devices and active devices simultaneously using a standard circuit solver and the simulation can be done in short time, thus providing a major speedup over methods that do not utilize lumped elements. It overcomes the limit of the finite-element methods that solve problems using many pieces of elements and boundary conditions. The partial elements paradigm of this method, as well as the production of circuit models, make this method very well suited for codesign of devices with circuitry applications.

The starting point is primitive cells or partial elements (PEs), so accuracy of the whole modeling procedure is totally dependent on the accuracy of the measurement-based partial element equivalent circuit (M-PEEC) models. There are a number of ways to define these partial elements, but careful selection can result in relatively few partial elements even for a complex structure. If accurate models for each of the partial elements along with interaction information can be obtained, then any arbitrary structure comprised of those partial elements can be modeled accurately using the obtained M-PEEC models. Once the partial elements have been defined, the next step is to design and fabricate test structures to obtain data in order to characterize them. This is then followed by calibration and high-frequency measurement of the test structures. The measured data is then used to extract M-PEEC models of the test structures. The obtained equivalent circuit models of the partial elements and design rules can be used to build a library. After constructing a valid library, a designer can then use it to design and optimize a new

and different dimensioned device. Through a based design rule checking step, the design of the new device can be used in the codesign with circuitry.

6.3. Test Structure and Partial Element (PE)

The models of partial elements (PEs) can be extracted from the measured S-parameters of test structures. The whole set of predefined partial elements should be included in test structures that are designed and manufactured in the process of interest. Measurements are performed on these structures by use of a high-frequency S-parameters measurement. In general, any test structure will be comprised of several different partial elements. Using the measured data, optimization and extraction routines are performed to extract M-PEEC models for each of the embedded partial elements [4]. These partial elements and their associated models can be used to predict the behavior of other arbitrary geometry structures made in the same process as the test structures, if they are comprised of the modeled partial elements in a specified and correct manner. This method generates equivalent circuits of the devices, and the predictions are obtained simply through circuit simulation utilizing standard SPICE-like software. Figure 6.3.1 shows the test structure composed of several partial elements. An MSM PD consists of several interdigitated partial elements as shown in Fig. 6.3.2. The metal-semiconductor-metal photodetectors are composed of four partial elements such as pad, square, interdigitated partial elements.

Accurate equivalent circuit models of individual predefined partial elements can be obtained using measured s-parameters of the measurements. Figure 6.3.3 shows MSM PDs structures with different size for the verification of this method. In optical waveguide applications, the length of finger is fixed with respect to width of optical waveguide. The number of metal fingers only can be varied and affect optical coupling efficiency.

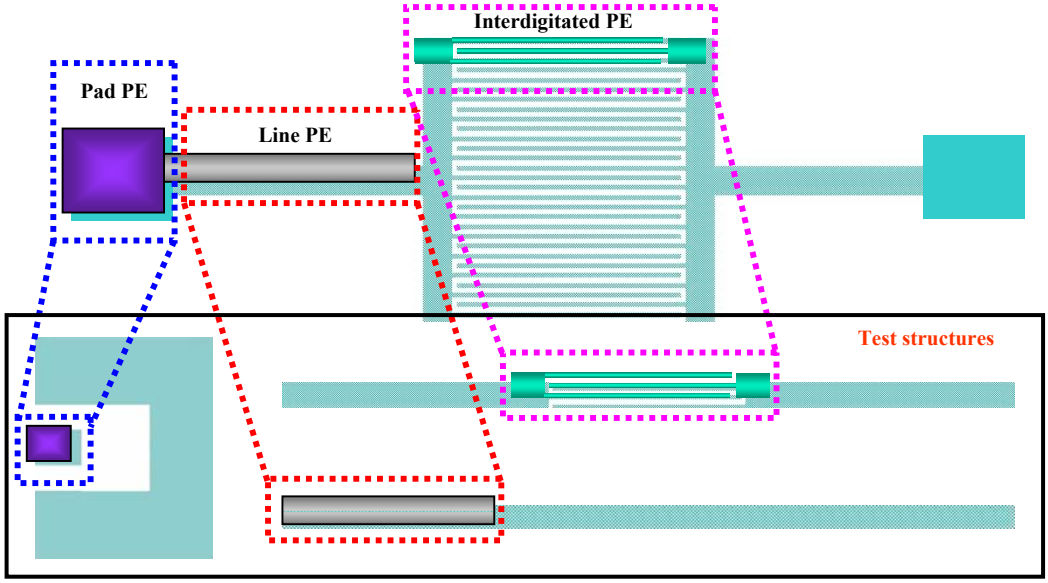

Figure 6.3.1. Three test structures and three partial elements: pad, square line, and interdigitated partial elements.

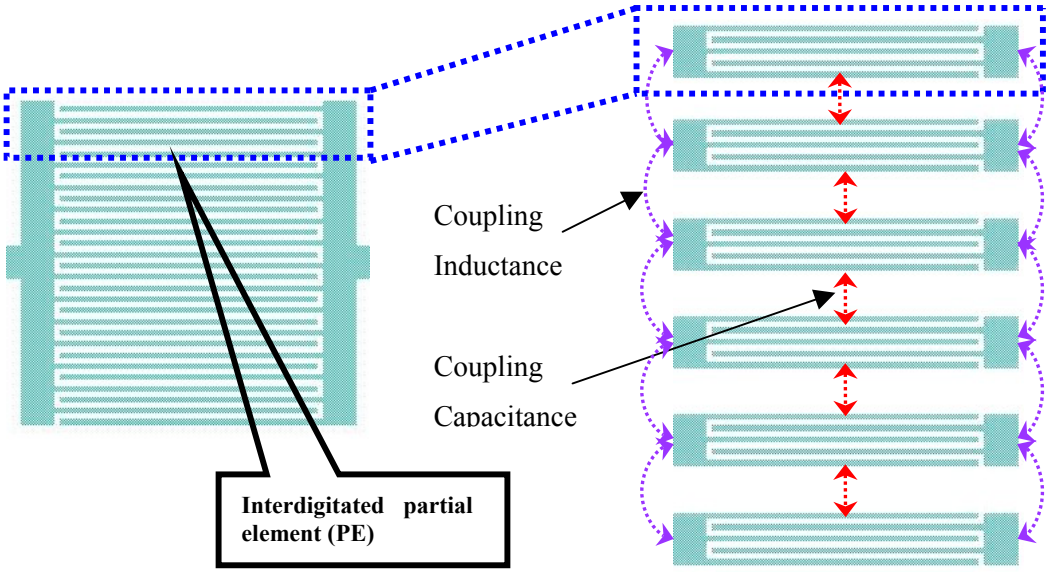

Figure 6.3.2. An MSM PD consists of six interdigitated PEs.

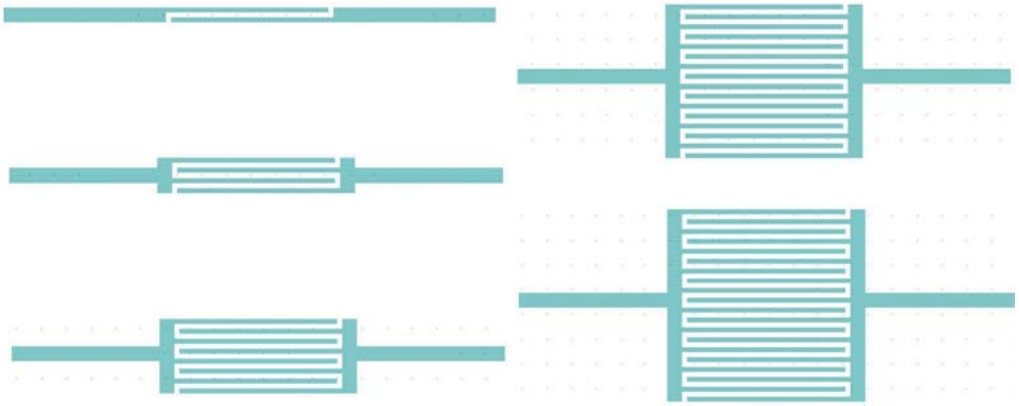

Figure 6.3.3. Scalable MSM PDs: 2,4,8,16,and 20 fingers.

6.4. Optimization and M-PEEC Extraction

The M-PEEC models are obtained by fitting circuit parameter values to the measured s-parameters of the test structures through an optimization procedure. In this procedure, the optimized parameters could diverge, depending on the initial values of the parameters and may deviate from measured s-parameters in case of local minimum points. To find the global minimum point, it is essential to find reasonable and representative estimated initial values of the parameters. For estimating initial values, DC I-V and C-V measurements usually have been used. However, these measurements are not suitable for estimation because the I-V measurement is usually done at high current level and the C-V measurement is done in the low-frequency range, which is not sensitive enough to the actual operation range of the DUT [73]. In this research, initial values are directly found from S-parameters through calculation of the initial parameter values using assumed simple equivalent circuit models.

First, "Pad M-PEEC" model is obtained using pad test structure in Fig. 6.4.1. This obtained pad M-PEEC model will be used for modeling of other M-PEEC models such as "Line M-PEEC" and "Interdigitated M-PEEC" models in the next modeling procedures. The second step is finding "Line M-PEEC" model using "Line" test structure in Fig. 6.4.2. This obtained line M-PEEC model will be used for the modeling of the "Interdigitated M-PEEC" model in the next modeling step. The last step is developing "Interdigitated M-PEEC" model using "Interdigitated" test structure in Fig. 6.4.3. A

summary of the generated parameter values of three M-PEEC models are presented in Table 6.4.1.

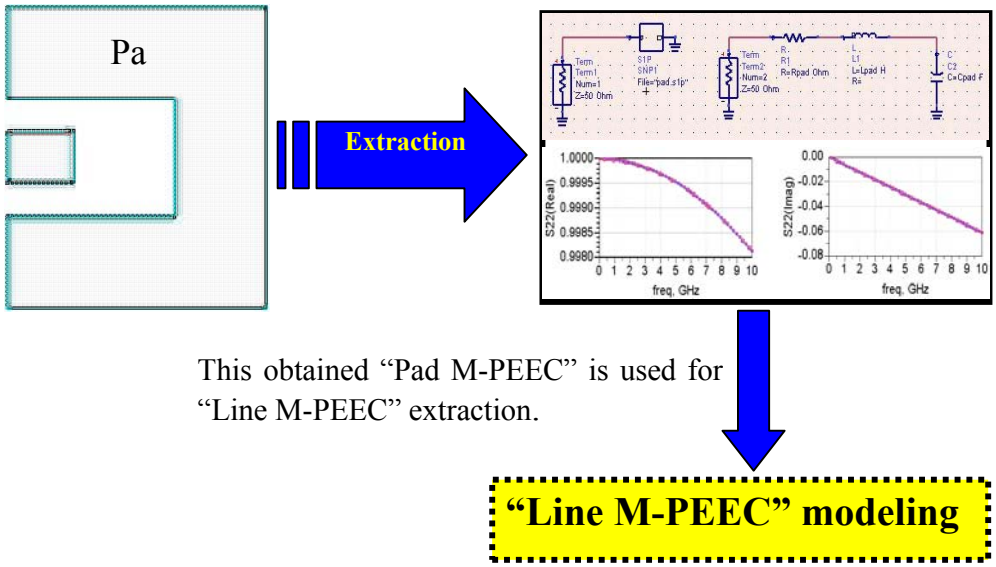

Figure 6.4.1. Step I: Pad M-PEEC model.

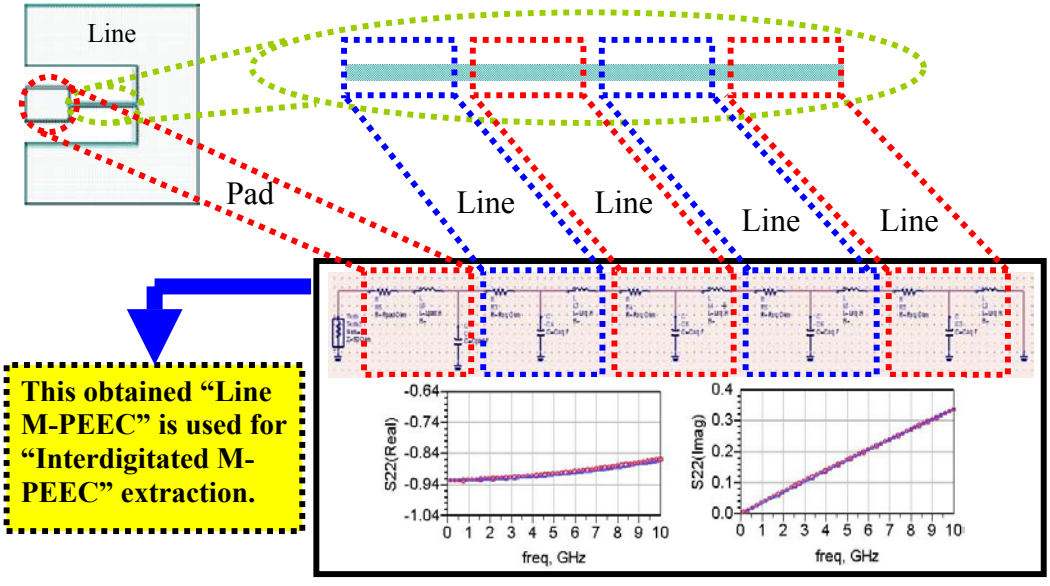

Figure 6.4.2. Step II: Line M-PEEC model.

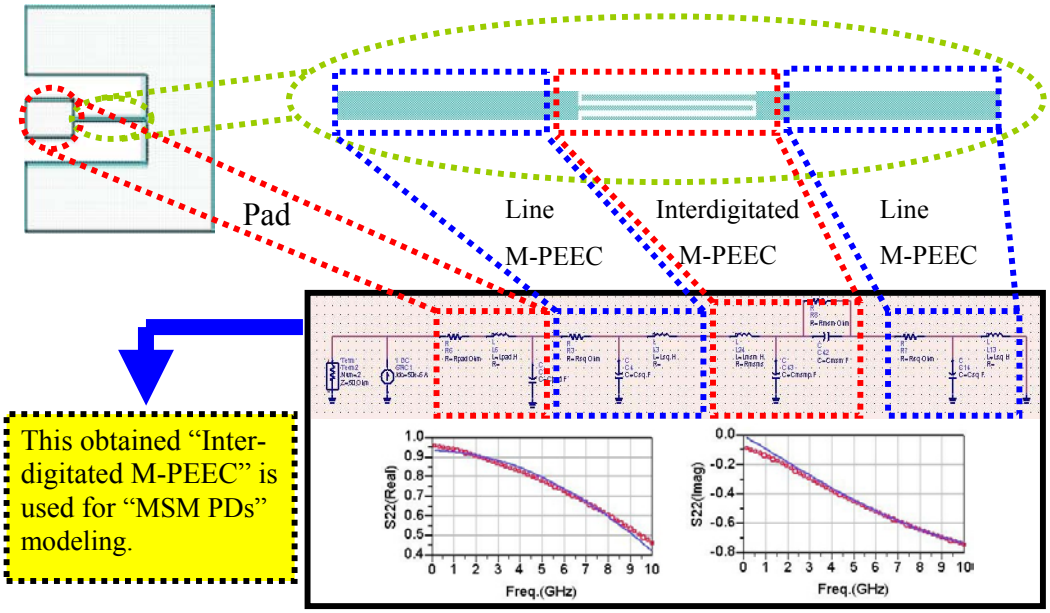

Figure 6.4.3. Step III: Interdigitated M-PEEC model.

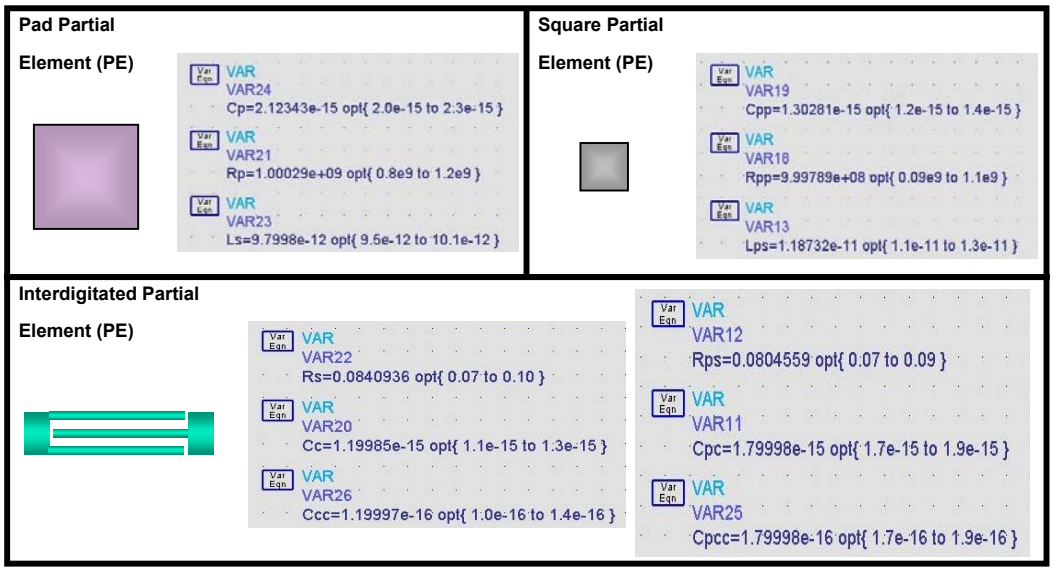

Figure 6.4.4. Parameter values of the three M-PEEC.

6.5. Results

In the previous section, the M-PEEC models are extracted for the all PEs: pad, square, and interdigitated partial elements. Those generated M-PEEC models can be used to predict the equivalent-circuit model of target MSM photodetectors that are comprised of those partial elements. Fig. 6.5.1 shows a MSM PD that is partitioned into several PEs and fabricated test structures are shown in Fig. 6.5.2. The final results are shown in Fig. 6.5.3 for the 40/1/1, 60/1/1, and 80/1/1 μm MSM photodetectors. Three S-parameters are compared: measured, M-PEEC, and equation-based models. For the equation-based models, only parasitic capacitance model is considered in the models.

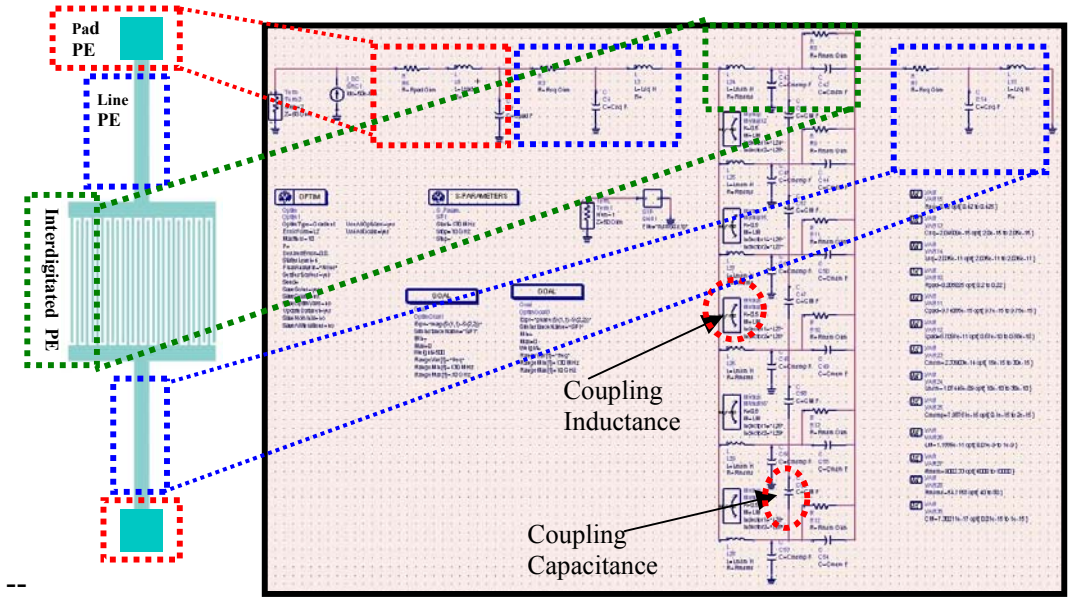

--

Figure 6.5.1. MSM PD that is comprised of three PEs: pad, line, and interdigitated partial elements.

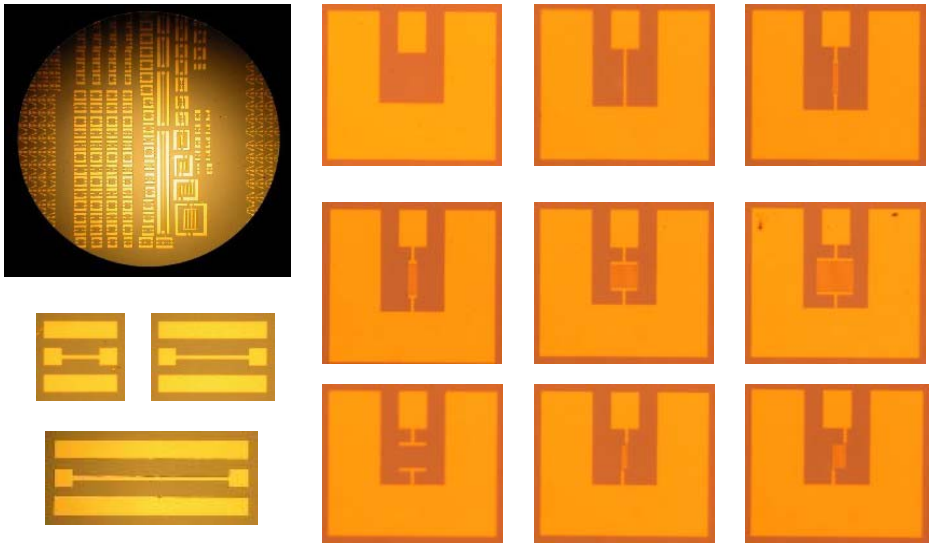

Figure 6.5.2. Photographs of the fabricated test structures.

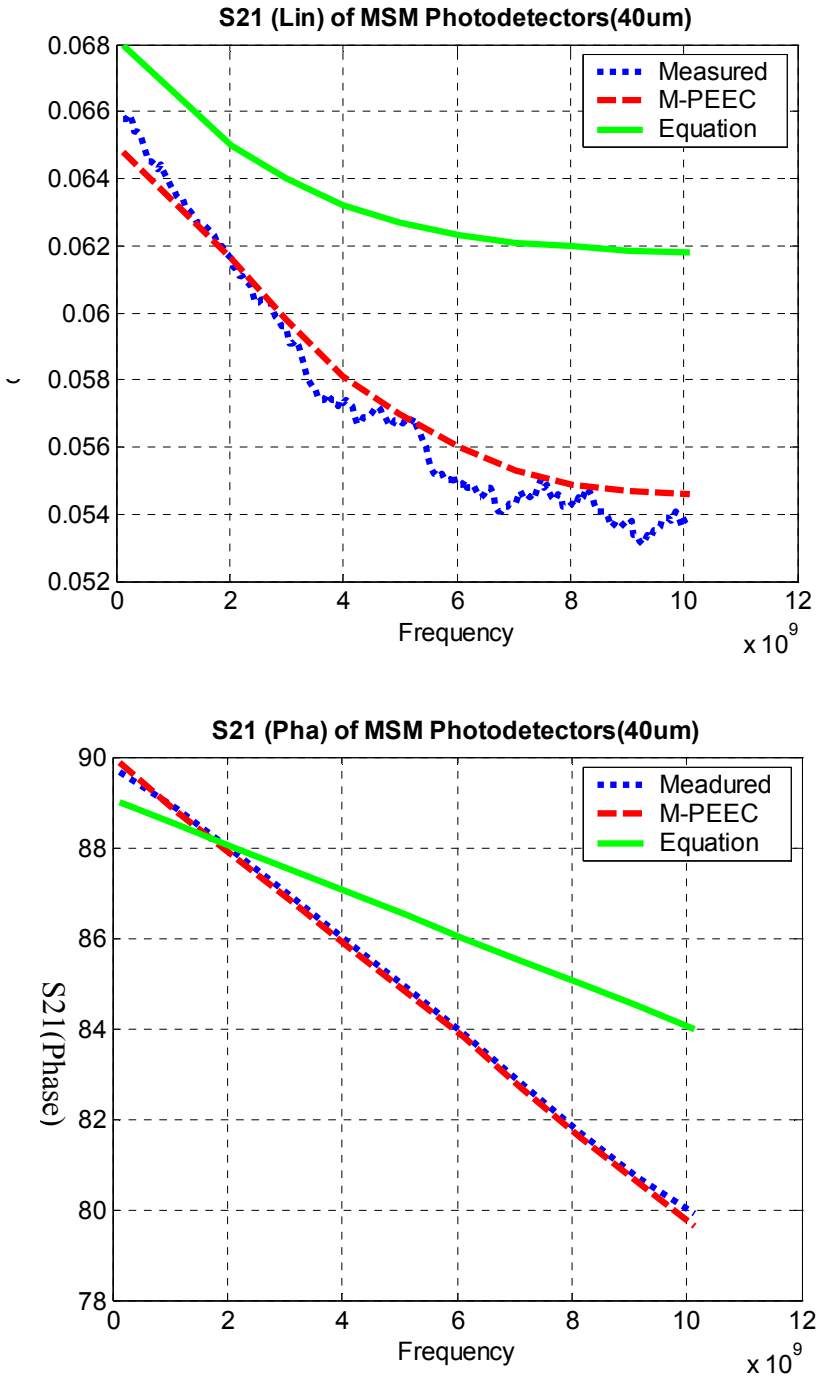

(a) S21 of 40um MSM PD at 5V: measured, M-PEEC, and equation-based models.

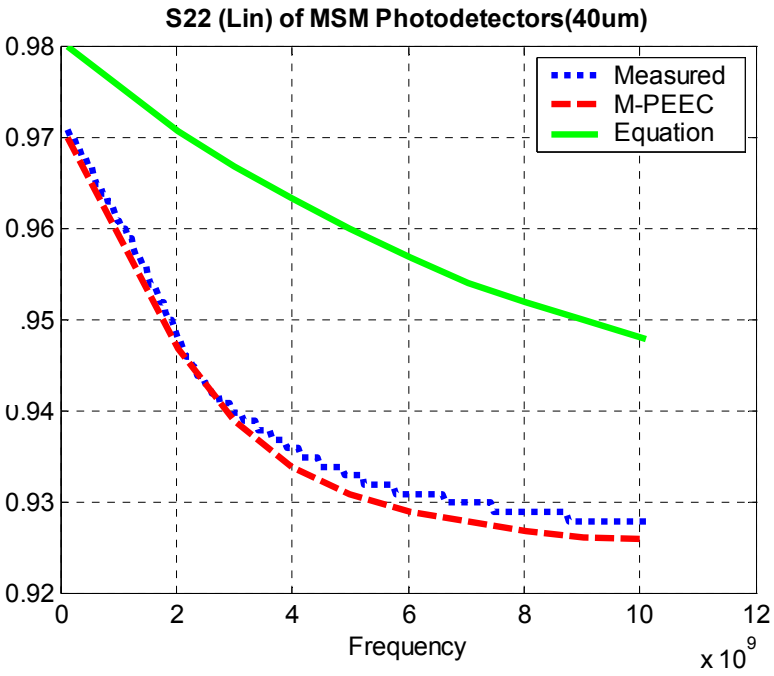

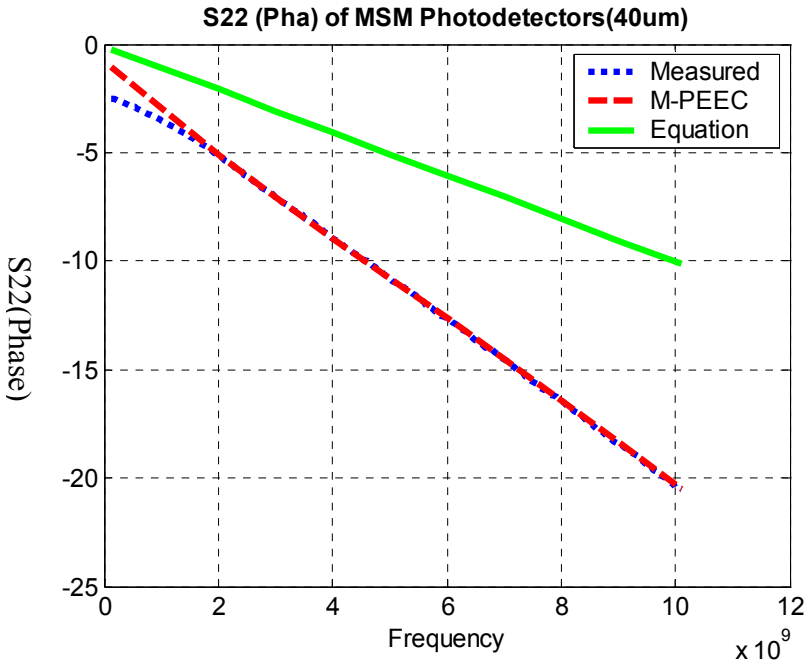

(b) S22 of 40um MSM PD at 5V: measured, M-PEEC, and equation-based models.

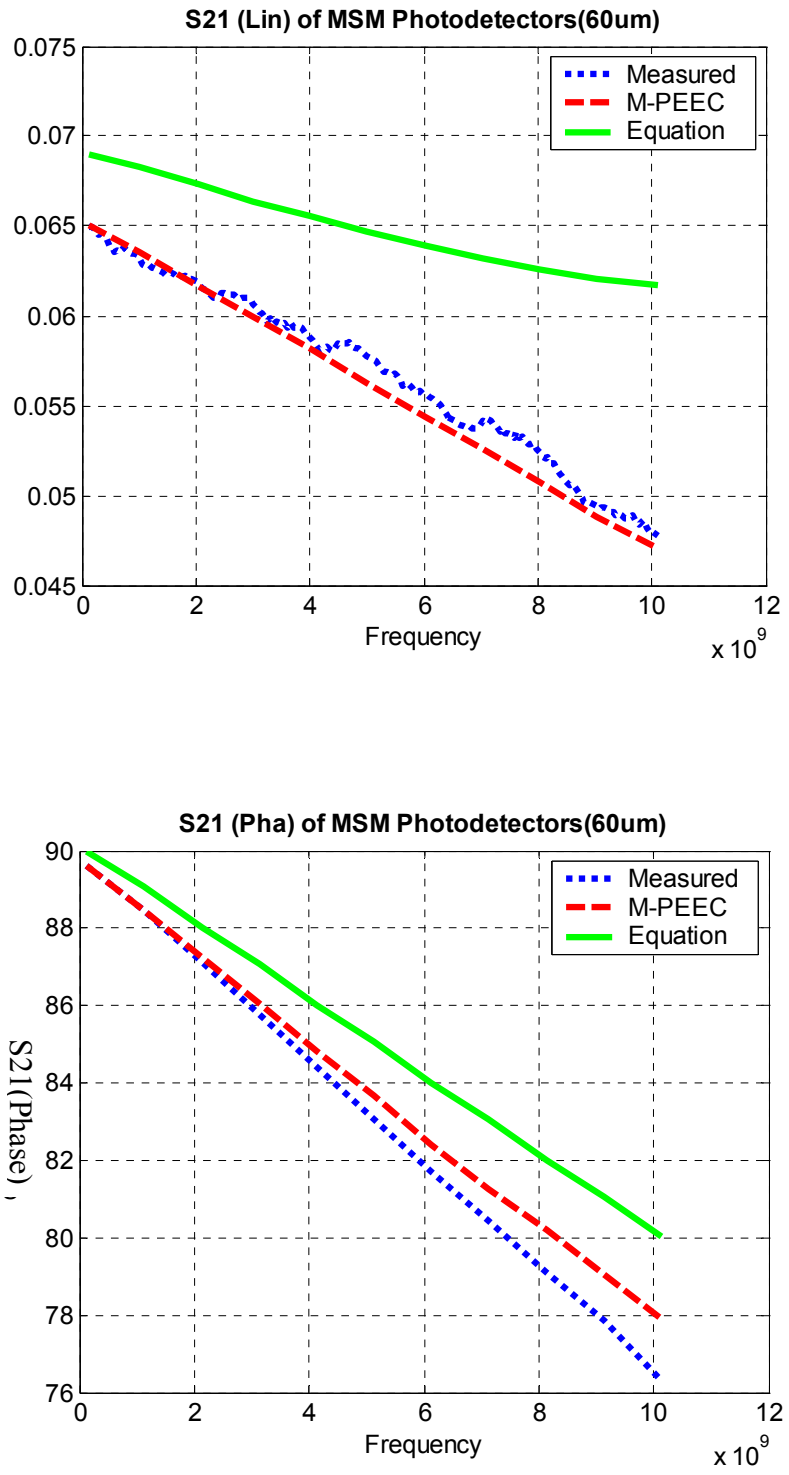

(c) S21 of 60um MSM PD at 5V: measured, M-PEEC, and equation-based models.

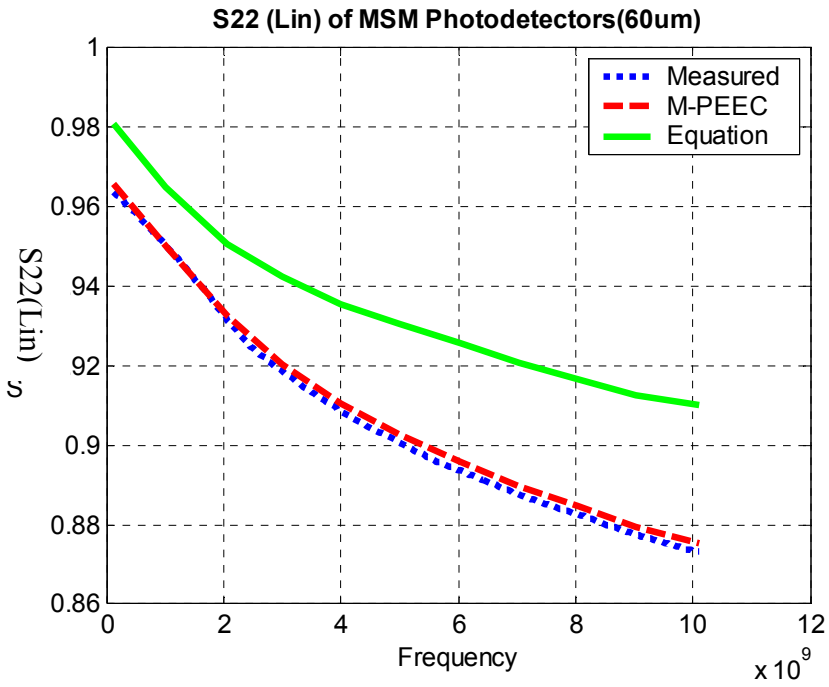

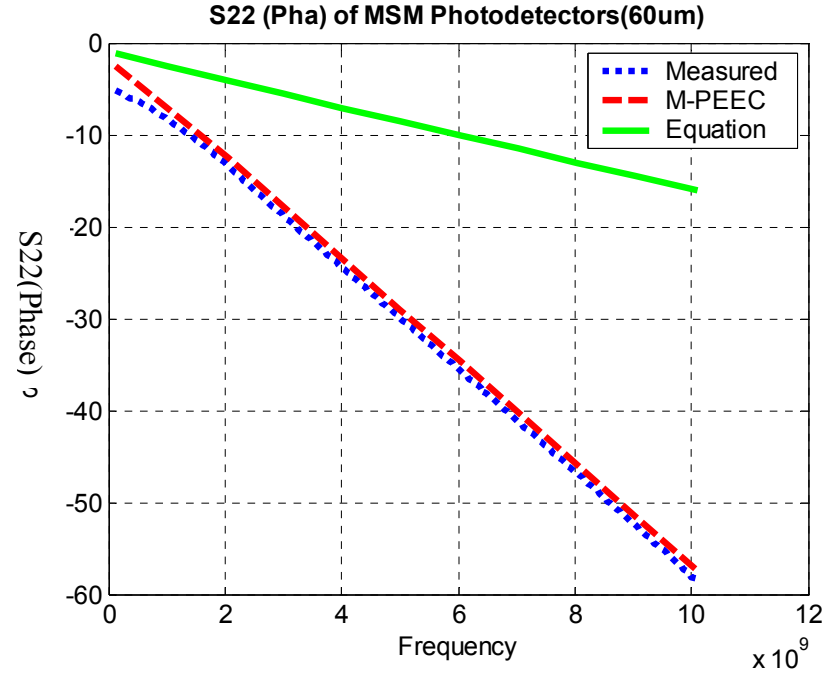

(d) S22 of 60um MSM PD at 5V: measured, M-PEEC, and equation-based models.

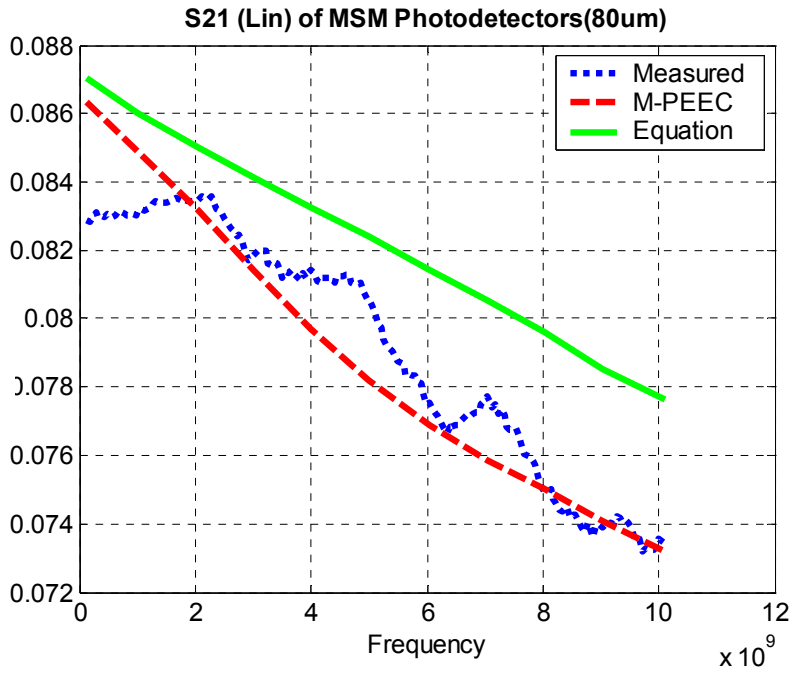

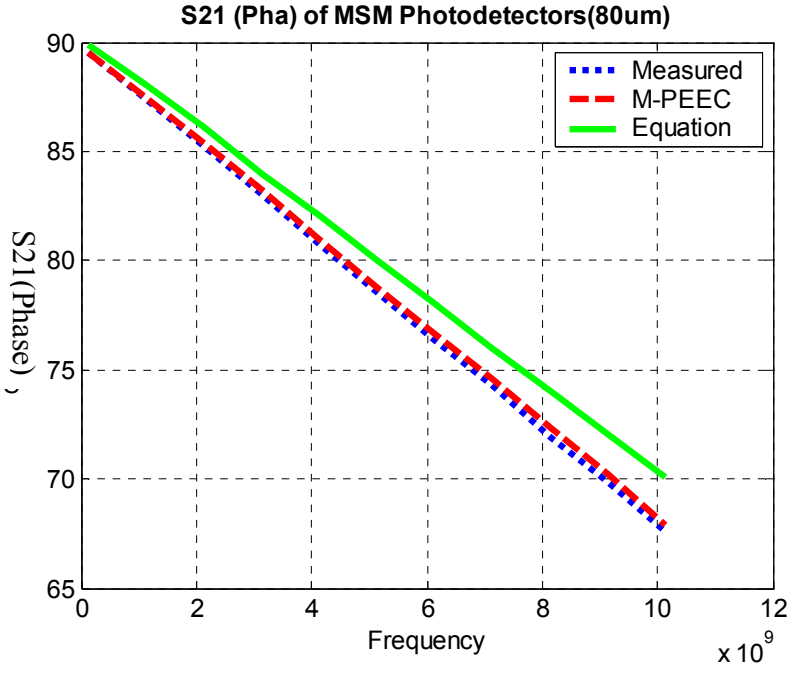

(e) S21 of 80um MSM PD at 5V: measured, M-PEEC, and equation-based models.

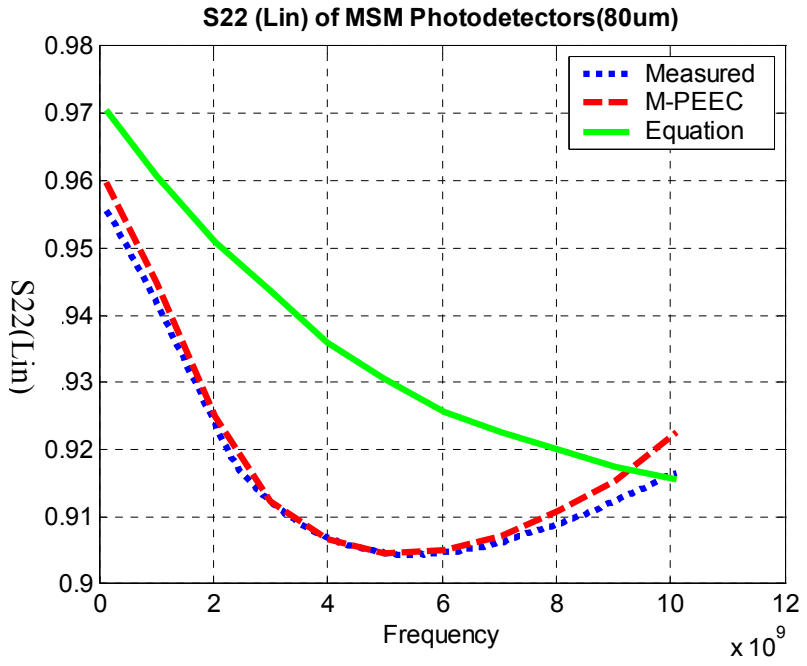

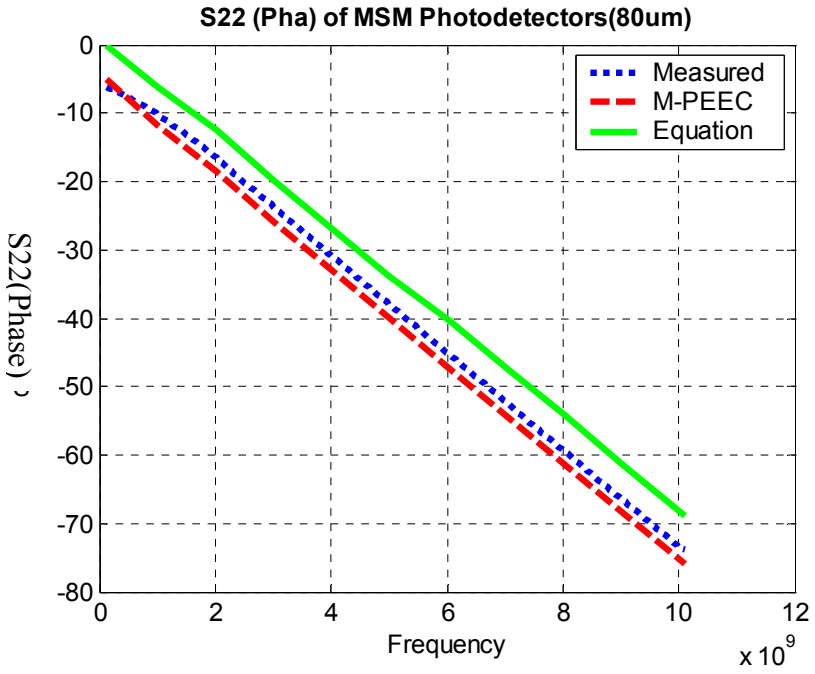

(f) S22 of 80μm MSM PD at 5V: measured, M-PEEC, and equation-based models.

Figure 6.5.3. S-parameters of MSM photodetectors

CHAPTER VII

SUMMARY AND CONCLUSIONS

6.1. Summary

In the second chapter, an overview of the various device and interconnect modeling methods has been presented and classified, and a comparison between methods and brief discussion have also been presented. Especially, the advantages of measurement-based modeling methods have been covered in detail. The origin and concept of partial element equivalent circuit (PEEC) model were introduced, and all equations were derived and verified to generate the parameter values of the each PEEC model by solving Maxwell's equations in this chapter.

In the third chapter, a novel and hybrid modeling method, measurement-based partial element equivalent circuit (M-PEEC) model, was proposed. The basic idea of the proposed modeling method is that any target structures can be subdivided into several key geometrical primitive cells, which is called partial elements (PEs). If equivalent-circuit models of each PE are known, the equivalent-circuit models of target structures that are composed of those PEs can be obtained. Detailed modeling procedures, concept of PE, and test structure were also presented in this chapter. A case study was presented

to demonstrate and verify the proposed modeling method. The M-PEEC model of a straight line was also compared to method of momentum (MoM) simulation in this case study.

In the fourth chapter, components of the front-end of the optical receiver has been covered. Especially, physical properties and main performance metrics of the metal-semiconductor-metal photodetector (MSM PD) and several design topology and their simulation results of the preamplifier were discussed in detail in this chapter. An improved and complete capacitance model of MSM photodetector was also proposed.

In the fifth chapter, fabrication procedures of each device, calibration methods, measurements, and deembedding techniques were covered in detail. Especially, on-wafer calibration and one port deembedding technique have been discussed and demonstrated for accurate measurement-based modeling.

Finally in the last chapter, an optical active device, MSM photodetector, was modeled using the proposed modeling method described earlier in this thesis. The entire procedure has been described in detail, including partial element and test structure development, equivalent circuit extraction, and model verification, with results presented at each stage

6.2. Conclusions

A measurement-based modeling methodology for the modeling of electrical and optical devices has been proposed and verified in this dissertation. The proposed modeling method uses test structures, measurement, predefined partial elements (PEs), and their measurement-based partial equivalent circuit (M-PEEC) models to accurately model target device under test (DUT). The method is hybrid because it uses accurate and scaleable partial element equivalent circuit (PEEC) model that is originated numerical-based method and it uses measurement that can take into account unexpected processing effects such as non-uniform material properties, uneven metal depositions, and processing fluctuations.

This method can be implemented conventional circuit simulation tools and simulation time is within an hour, which circumvents inconvenient interface between device design tools and circuit design tools. The output of this modeling method is SPICE-like circuit-level model, so those obtained models can be easily integrated into a modern circuit design EDA framework for co-designing, which will maximize the performance of a module or system.

The proposed method has been experimentally and theoretically verified for electrical passive devices and optical active devices. In all cases, good prediction results were obtained to model their electrical behaviors up to 20GHz.

APPENDIX A

A.1. S-parameters of Test Structures and MSM Photodetectors

A.1.1. S-parameters of Line

Frequency	S11(Magnitude)	S11(Phase)	S21(Magnitude)	S21(Phase)
6.27E+08	0.02637291	-45.50977	0.9682007	-2.149292
7.26E+08	0.02672386	-48.64452	0.9672241	-2.285156
8.25E+08	0.02709675	-51.82812	0.9661865	-2.421143
9.25E+08	0.02748871	-55.04296	0.9651184	-2.562622
1.02E+09	0.02791214	-58.35546	0.9640198	-2.709595
1.12E+09	0.0283308	-61.70507	0.9629211	-2.855103
1.22E+09	0.02876854	-65.10156	0.961731	-3.008911
1.32E+09	0.02920914	-68.55469	0.9606018	-3.160034
1.42E+09	0.02968407	-72.09374	0.9593201	-3.315186
1.52E+09	0.0301466	-75.64062	0.9579163	-3.468994
1.62E+09	0.03062248	-79.28905	0.956665	-3.625488
1.72E+09	0.03109169	-82.95702	0.9552917	-3.78479
1.82E+09	0.03158379	-86.66407	0.9538574	-3.953735
1.92E+09	0.03209305	-90.43749	0.9525146	-4.118652
2.02E+09	0.03256989	-94.23437	0.9511414	-4.30127
2.12E+09	0.03307152	-98.11718	0.9496155	-4.477051
2.22E+09	0.03360176	-101.9375	0.9480591	-4.654297
2.32E+09	0.03415871	-105.3594	0.9465027	-4.825928
2.42E+09	0.03473854	-108.5039	0.9450073	-4.986572
2.51E+09	0.03534889	-111.4375	0.9434814	-5.140381
2.61E+09	0.03595734	-114.1914	0.941925	-5.29541
2.71E+09	0.03654099	-116.7969	0.9404907	-5.439697
2.81E+09	0.03714752	-119.2031	0.9390564	-5.583984
2.91E+09	0.03779984	-121.5195	0.9375	-5.717041
3.01E+09	0.03848076	-123.7695	0.9362183	-5.858643
3.11E+09	0.03927422	-126.0859	0.9345398	-5.99585
3.21E+09	0.03994942	-128.4062	0.9331665	-6.126465
3.31E+09	0.04063034	-130.5	0.9317322	-6.270508
3.41E+09	0.0413723	-132.7578	0.9301453	-6.401123
3.51E+09	0.04205322	-134.9062	0.928772	-6.525879

3.61E+09	0.0426445	−136.9766	0.9272461	−6.644043
3.71E+09	0.04326439	−138.9531	0.9258118	−6.763672
3.81E+09	0.04385948	−140.8672	0.924408	−6.878906
3.91E+09	0.04444122	−142.8203	0.9230347	−6.984619
4E+09	0.04499245	−144.6484	0.9219971	−7.097168
4.1E+09	0.04553604	−146.4375	0.9206238	−7.194824
4.2E+09	0.04604912	−148.1641	0.9192505	−7.293701
4.3E+09	0.04659653	−149.8047	0.9181519	−7.404785
4.4E+09	0.04711342	−151.4141	0.9169922	−7.511963
4.5E+09	0.0476265	−152.9609	0.9157104	−7.61499
4.6E+09	0.0481472	−154.4765	0.9145508	−7.709717
4.7E+09	0.04866982	−155.9375	0.913269	−7.793457
4.8E+09	0.04919243	−157.3906	0.9120789	−7.891113
4.9E+09	0.04970169	−158.8203	0.9110718	−7.98999
5E+09	0.05017662	−160.2422	0.9101257	−8.084961
5.1E+09	0.05062485	−161.5859	0.908905	−8.176758
5.2E+09	0.0510788	−162.8984	0.9077148	−8.266113
5.3E+09	0.05154991	−164.1875	0.9067078	−8.36084
5.4E+09	0.05202293	−165.4687	0.9056702	−8.465332
5.49E+09	0.05247498	−166.6875	0.9046936	−8.554688
5.59E+09	0.05291939	−167.9219	0.9038696	−8.651855
5.69E+09	0.05337143	−169.0703	0.9028931	−8.744141
5.79E+09	0.05386162	−170.2031	0.9020081	−8.838867
5.89E+09	0.05432129	−171.3828	0.9010925	−8.920898
5.99E+09	0.05478096	−172.4766	0.900177	−9.010254
6.09E+09	0.05527687	−173.5547	0.8992615	−9.089844
6.19E+09	0.05578232	−174.5703	0.898468	−9.172363
6.29E+09	0.05623627	−175.625	0.8977356	−9.258789
6.39E+09	0.0567627	−176.6797	0.8969727	−9.345703
6.49E+09	0.05724907	−177.7578	0.8961487	−9.419434
6.59E+09	0.05773354	−178.8047	0.8954468	−9.503418
6.69E+09	0.0582428	−179.8047	0.8947144	−9.580078
6.79E+09	0.05875015	179.1641	0.8937988	−9.669434
6.89E+09	0.05917168	178.0859	0.8933105	−9.745117
6.99E+09	0.05965996	177.0703	0.8924866	−9.834473
7.08E+09	0.06007957	176.0781	0.8918457	−9.915527
7.18E+09	0.06051636	175.0781	0.8912354	−10.00732
7.28E+09	0.06095505	174.0937	0.890564	−10.08838
7.38E+09	0.06141472	173.0937	0.8899231	−10.16553
7.48E+09	0.06184959	172.2188	0.8893738	−10.24219
7.58E+09	0.06227684	171.2812	0.8886414	−10.33301

7.68E+09	0.06269836	170.3672	0.8879395	−10.41406
7.78E+09	0.06315231	169.4297	0.8874512	−10.48535
7.88E+09	0.06357956	168.4922	0.8868713	−10.57178
7.98E+09	0.06398392	167.6328	0.8862305	−10.65283
8.08E+09	0.06441498	166.8047	0.885498	−10.72021
8.18E+09	0.06484222	165.9844	0.8850098	−10.79834
8.28E+09	0.06529999	165.1094	0.8847351	−10.87793
8.38E+09	0.0657196	164.2344	0.8842163	−10.96191
8.48E+09	0.06612396	163.4063	0.883667	−11.04834
8.57E+09	0.06655884	162.5859	0.8830566	−11.12793
8.67E+09	0.06701279	161.7734	0.8824768	−11.21436
8.77E+09	0.06744385	160.9609	0.8820496	−11.30225
8.87E+09	0.0678978	160.1563	0.8815613	−11.37939
8.97E+09	0.06830215	159.3594	0.8810425	−11.46289
9.07E+09	0.06872177	158.5938	0.8804016	−11.5498
9.17E+09	0.06918716	157.8281	0.8800964	−11.63477
9.27E+09	0.06964111	157.0547	0.8797607	−11.71973
9.37E+09	0.07009125	156.2266	0.8793945	−11.79541
9.47E+09	0.07049179	155.4688	0.8789368	−11.875
9.57E+09	0.07089615	154.75	0.878418	−11.96045
9.67E+09	0.07135391	154.0313	0.8780212	−12.05615
9.77E+09	0.07183838	153.2969	0.877533	−12.14014
9.87E+09	0.07229614	152.5312	0.8770752	−12.22949
9.97E+09	0.07273102	151.8516	0.8767395	−12.32129
1.01E+10	0.07320023	151.1172	0.8764343	−12.41455
1.02E+10	0.07368469	150.3984	0.8759766	−12.49316
1.03E+10	0.0741539	149.6797	0.8755798	−12.57666
1.04E+10	0.07456589	148.9297	0.8751221	−12.66211
1.05E+10	0.07491302	148.2109	0.8748169	−12.74561
1.06E+10	0.07529831	147.5625	0.8743896	−12.8584
1.07E+10	0.07570267	146.9219	0.8740845	−12.95166
1.08E+10	0.07608032	146.1797	0.8738098	−13.03955
1.09E+10	0.07644272	145.5078	0.8734741	−13.12207
1.1E+10	0.07687759	144.9141	0.8730469	−13.2085
1.11E+10	0.07727051	144.2734	0.8728333	−13.29102
1.12E+10	0.07779694	143.6563	0.8724365	−13.37598
1.13E+10	0.07825851	143	0.8720703	−13.46387
1.14E+10	0.07871628	142.3828	0.8717957	−13.56006
1.15E+10	0.07911682	141.7813	0.87146	−13.65479
1.16E+10	0.07950211	141.2266	0.8711853	−13.74951
1.17E+10	0.07994461	140.6094	0.8707886	−13.84033

1.18E+10	0.08039474	139.9765	0.870697	−13.93066
1.19E+10	0.08072662	139.3516	0.8704224	−14.01758
1.2E+10	0.08111191	138.7656	0.8701477	−14.10791
1.21E+10	0.08154678	138.2109	0.8699036	−14.20264
1.22E+10	0.08198547	137.6172	0.8696594	−14.28662
1.23E+10	0.08243179	137.0312	0.8694763	−14.38672
1.24E+10	0.08282852	136.5234	0.8692322	−14.47217
1.24E+10	0.08321381	135.9766	0.8686829	−14.56543
1.25E+10	0.08361816	135.4453	0.8685303	−14.63135
1.26E+10	0.08410645	134.8906	0.8681641	−14.73828
1.27E+10	0.08455276	134.3125	0.8679504	−14.83594
1.28E+10	0.08498764	133.7891	0.8677673	−14.92529
1.29E+10	0.08530045	133.2109	0.8675537	−15.02393
1.3E+10	0.08573914	132.7109	0.867218	−15.11475
1.31E+10	0.08625412	132.1484	0.8670044	−15.19824
1.32E+10	0.08675385	131.5703	0.8668518	−15.28906
1.33E+10	0.0871315	131.0078	0.8664856	−15.38086
1.34E+10	0.08748245	130.5312	0.8660889	−15.47705
1.35E+10	0.08794785	130.039	0.8657532	−15.55957
1.36E+10	0.08843231	129.5391	0.8656006	−15.64355
1.37E+10	0.08884811	128.9531	0.8652954	−15.70947
1.38E+10	0.08916473	128.4219	0.8650818	−15.81104
1.39E+10	0.08950424	127.9258	0.8647461	−15.89453
1.4E+10	0.08990479	127.4219	0.8644409	−15.97559
1.41E+10	0.09040833	126.9258	0.8639832	−16.05469
1.42E+10	0.09089279	126.3945	0.8637085	−16.14453
1.43E+10	0.09124374	125.8633	0.8633423	−16.24121
1.44E+10	0.09166336	125.3906	0.862854	−16.32617
1.45E+10	0.09214401	124.9414	0.8623962	−16.40723
1.46E+10	0.0926857	124.4219	0.8620605	−16.49219
1.47E+10	0.09316635	123.8398	0.8615417	−16.58203
1.48E+10	0.09355164	123.3516	0.8612061	−16.67871
1.49E+10	0.09392548	122.8945	0.8608398	−16.76855
1.5E+10	0.09442139	122.4609	0.860321	−16.86133
1.51E+10	0.09494019	121.9805	0.8600159	−16.94433
1.52E+10	0.09528732	121.4805	0.8595886	−17.03516
1.53E+10	0.09555054	120.9883	0.8592834	−17.11719
1.54E+10	0.0958252	120.5703	0.8587952	−17.20898
1.55E+10	0.09630966	120.1328	0.8583374	−17.29004
1.56E+10	0.09681702	119.5547	0.8578186	−17.38477
1.57E+10	0.09724426	119.0273	0.8573914	−17.45605

1.58E+10	0.0975647	118.5508	0.8568115	−17.53906
1.59E+10	0.09808731	118.1094	0.8562927	−17.625
1.6E+10	0.09850693	117.7266	0.8559875	−17.70898
1.61E+10	0.09904099	117.2266	0.8554382	−17.79687
1.62E+10	0.0994072	116.7383	0.8549805	−17.8916
1.63E+10	0.09970093	116.2305	0.8544922	−17.96875
1.64E+10	0.09993744	115.8633	0.8540344	−18.05664
1.65E+10	0.1004601	115.4648	0.8537598	−18.13477
1.66E+10	0.1010246	115.043	0.853363	−18.23535
1.67E+10	0.1012726	114.5547	0.8531494	−18.29785
1.68E+10	0.1013985	114.2109	0.8526917	−18.36816
1.69E+10	0.1018372	113.7969	0.8520813	−18.45605
1.7E+10	0.1023712	113.4375	0.8516235	−18.53125
1.71E+10	0.1028595	112.957	0.8512573	−18.61133
1.72E+10	0.1031303	112.543	0.8506165	−18.68555
1.73E+10	0.1033707	112.1641	0.8500977	−18.76758
1.74E+10	0.1037903	111.8672	0.8495789	−18.84863
1.75E+10	0.1044159	111.4805	0.8492737	−18.93359
1.76E+10	0.1047783	111	0.8487854	−19.02344
1.77E+10	0.1050682	110.543	0.8482056	−19.10058
1.78E+10	0.1053085	110.2187	0.8476868	−19.19629
1.79E+10	0.1057739	109.9141	0.8471375	−19.26465
1.8E+10	0.1061707	109.5039	0.8465881	−19.34473
1.81E+10	0.1065369	109.0977	0.8460083	−19.42676
1.82E+10	0.1067543	108.7148	0.84552	−19.50781
1.83E+10	0.1069641	108.3594	0.8449707	−19.58203
1.84E+10	0.107296	108.0391	0.8444824	−19.65137
1.85E+10	0.1076317	107.6641	0.8441467	−19.72363
1.86E+10	0.1079063	107.3047	0.8437195	−19.79883
1.87E+10	0.1080894	106.9805	0.8432312	−19.85254
1.88E+10	0.1083069	106.707	0.8427734	−19.91504
1.89E+10	0.1085892	106.3984	0.8421936	−19.9707
1.9E+10	0.1089172	106.0703	0.8417664	−20.03125
1.91E+10	0.1091309	105.7187	0.8413391	−20.09082
1.92E+10	0.1092873	105.4453	0.8408508	−20.15527
1.93E+10	0.10952	105.1719	0.8404846	−20.20703
1.94E+10	0.1098518	104.9414	0.8399963	−20.26074
1.95E+10	0.1101646	104.6328	0.8395996	−20.30273
1.96E+10	0.1102943	104.3789	0.8392639	−20.3584
1.97E+10	0.1103973	104.1719	0.8389587	−20.39063
1.98E+10	0.1105309	104.0195	0.8385925	−20.44726

1.99E+10	0.1107826	103.8164	0.8383179	-20.49316
2E+10	0.1109085	103.6055	0.8379211	-20.54394

A.1.2. S-parameters of MSM Photodetector (60/1/1 μm)

Frequency	S11(Magnitude)	S11(Phase)	S21(Magnitude)	S21(Phase)
1.30E+08	7.28E-04	-1.64E+02	6.50E-02	2.43E+01
1.80E+08	7.29E-04	-1.71E+02	6.49E-02	1.83E+01
2.29E+08	7.23E-04	-1.77E+02	6.47E-02	1.20E+01
2.79E+08	7.18E-04	1.76E+02	6.45E-02	5.67E+00
3.29E+08	7.11E-04	1.68E+02	6.46E-02	-7.18E-01
3.78E+08	7.15E-04	1.60E+02	6.45E-02	-7.27E+00
4.28E+08	7.13E-04	1.49E+02	6.43E-02	-1.40E+01
4.78E+08	7.08E-04	1.38E+02	6.39E-02	-2.07E+01
5.27E+08	5.93E-04	1.27E+02	6.38E-02	-2.76E+01
5.77E+08	5.92E-04	1.18E+02	6.36E-02	-3.46E+01
6.27E+08	5.98E-04	1.10E+02	6.36E-02	-4.19E+01
6.76E+08	6.05E-04	1.02E+02	6.36E-02	-4.92E+01
7.26E+08	6.11E-04	9.37E+01	6.38E-02	-5.68E+01
7.76E+08	6.27E-04	8.48E+01	6.36E-02	-6.46E+01
8.25E+08	6.35E-04	7.79E+01	6.35E-02	-7.23E+01
8.75E+08	6.41E-04	6.95E+01	6.35E-02	-8.03E+01
9.25E+08	6.44E-04	6.24E+01	6.35E-02	-8.85E+01
9.74E+08	6.48E-04	5.66E+01	6.34E-02	-9.67E+01
1.02E+09	6.62E-04	5.13E+01	6.32E-02	-1.05E+02
1.07E+09	6.67E-04	4.42E+01	6.29E-02	-1.14E+02
1.12E+09	6.62E-04	3.90E+01	6.28E-02	-1.22E+02
1.17E+09	6.69E-04	3.44E+01	6.28E-02	-1.31E+02
1.22E+09	6.79E-04	3.03E+01	6.27E-02	-1.40E+02
1.27E+09	6.87E-04	2.49E+01	6.27E-02	-1.49E+02
1.32E+09	6.86E-04	1.86E+01	6.26E-02	-1.58E+02
1.37E+09	6.88E-04	1.16E+01	6.25E-02	-1.68E+02
1.42E+09	6.98E-04	6.72E+00	6.24E-02	-1.78E+02
1.47E+09	7.01E-04	1.93E+00	6.23E-02	1.73E+02
1.52E+09	7.00E-04	-6.48E-01	6.24E-02	1.63E+02
1.57E+09	7.01E-04	-2.91E+00	6.24E-02	1.53E+02

1.62E+09	7.01E-04	-6.99E+00	6.23E-02	1.43E+02
1.67E+09	7.01E-04	-1.06E+01	6.22E-02	1.33E+02
1.72E+09	7.07E-04	-1.38E+01	6.23E-02	1.22E+02
1.77E+09	7.11E-04	-1.69E+01	6.22E-02	1.12E+02
1.82E+09	7.13E-04	-2.11E+01	6.22E-02	1.01E+02
1.87E+09	7.12E-04	-2.31E+01	6.21E-02	8.99E+01
1.92E+09	7.13E-04	-2.48E+01	6.20E-02	7.90E+01
1.97E+09	7.22E-04	-2.76E+01	6.20E-02	6.79E+01
2.02E+09	7.20E-04	-3.12E+01	6.19E-02	5.65E+01
2.07E+09	7.28E-04	-3.36E+01	6.17E-02	4.51E+01
2.12E+09	7.26E-04	-3.55E+01	6.15E-02	3.35E+01
2.17E+09	7.26E-04	-3.89E+01	6.15E-02	2.16E+01
2.22E+09	7.17E-04	-4.52E+01	6.13E-02	9.70E+00
2.27E+09	7.17E-04	-5.04E+01	6.11E-02	-2.12E+00
2.32E+09	7.14E-04	-5.64E+01	6.10E-02	-1.40E+01
2.37E+09	7.19E-04	-6.45E+01	6.10E-02	-2.59E+01
2.42E+09	7.21E-04	-7.54E+01	6.11E-02	-3.77E+01
2.46E+09	7.31E-04	-8.66E+01	6.13E-02	-4.95E+01
2.51E+09	7.31E-04	-9.49E+01	6.13E-02	-6.13E+01
2.56E+09	7.28E-04	-1.01E+02	6.12E-02	-7.31E+01
2.61E+09	7.34E-04	-1.05E+02	6.12E-02	-8.49E+01
2.66E+09	7.33E-04	-1.07E+02	6.11E-02	-9.67E+01
2.71E+09	7.17E-04	-1.08E+02	6.10E-02	-1.08E+02
2.76E+09	7.11E-04	-1.10E+02	6.09E-02	-1.20E+02
2.81E+09	7.07E-04	-1.10E+02	6.10E-02	-1.32E+02
2.86E+09	7.13E-04	-1.09E+02	6.10E-02	-1.44E+02
2.91E+09	7.29E-04	-1.08E+02	6.10E-02	-1.56E+02
2.96E+09	7.31E-04	-1.04E+02	6.08E-02	-1.67E+02
3.01E+09	7.34E-04	-1.01E+02	6.06E-02	-1.79E+02
3.06E+09	7.44E-04	-9.63E+01	6.05E-02	1.69E+02
3.11E+09	7.51E-04	-8.83E+01	6.02E-02	1.57E+02
3.16E+09	7.42E-04	-7.86E+01	6.01E-02	1.45E+02
3.21E+09	7.51E-04	-6.51E+01	5.99E-02	1.34E+02
3.26E+09	7.45E-04	-5.13E+01	5.97E-02	1.22E+02
3.31E+09	7.42E-04	-3.79E+01	5.99E-02	1.10E+02
3.36E+09	7.52E-04	-2.27E+01	5.95E-02	9.81E+01
3.41E+09	7.63E-04	-6.70E+00	5.97E-02	8.65E+01
3.46E+09	7.67E-04	8.66E+00	5.96E-02	7.48E+01
3.51E+09	7.67E-04	2.50E+01	5.95E-02	6.30E+01

3.56E+09	7.75E-04	4.11E+01	5.96E-02	5.14E+01
3.61E+09	7.87E-04	5.67E+01	5.93E-02	3.97E+01
3.66E+09	7.88E-04	7.38E+01	5.96E-02	2.80E+01
3.71E+09	7.89E-04	8.82E+01	5.93E-02	1.63E+01
3.76E+09	7.75E-04	1.00E+02	5.93E-02	4.80E+00
3.81E+09	7.65E-04	1.13E+02	5.94E-02	-7.09E+00
3.86E+09	7.63E-04	1.30E+02	5.93E-02	-1.88E+01
3.91E+09	7.64E-04	1.48E+02	5.91E-02	-3.06E+01
3.95E+09	7.63E-04	1.67E+02	5.91E-02	-4.24E+01
4.00E+09	7.71E-04	-1.73E+02	5.88E-02	-5.41E+01
4.05E+09	7.72E-04	-1.50E+02	5.86E-02	-6.58E+01
4.10E+09	7.64E-04	-1.28E+02	5.84E-02	-7.76E+01
4.15E+09	7.68E-04	-1.08E+02	5.81E-02	-8.94E+01
4.20E+09	7.67E-04	-8.84E+01	5.81E-02	-1.01E+02
4.25E+09	7.72E-04	-6.94E+01	5.82E-02	-1.13E+02
4.30E+09	7.83E-04	-4.96E+01	5.83E-02	-1.24E+02
4.35E+09	7.89E-04	-3.11E+01	5.81E-02	-1.36E+02
4.40E+09	7.94E-04	-1.37E+01	5.80E-02	-1.48E+02
4.45E+09	7.88E-04	6.65E+00	5.82E-02	-1.60E+02
4.50E+09	7.85E-04	2.97E+01	5.85E-02	-1.72E+02
4.55E+09	7.87E-04	5.24E+01	5.84E-02	1.76E+02
4.60E+09	7.93E-04	7.28E+01	5.85E-02	1.64E+02
4.65E+09	7.89E-04	9.31E+01	5.84E-02	1.53E+02
4.70E+09	7.83E-04	1.12E+02	5.86E-02	1.41E+02
4.75E+09	7.78E-04	1.33E+02	5.83E-02	1.29E+02
4.80E+09	7.68E-04	1.55E+02	5.82E-02	1.17E+02
4.85E+09	7.57E-04	1.73E+02	5.82E-02	1.05E+02
4.90E+09	7.48E-04	-1.68E+02	5.80E-02	9.33E+01
4.95E+09	7.50E-04	-1.50E+02	5.79E-02	8.14E+01
5.00E+09	7.49E-04	-1.34E+02	5.78E-02	6.95E+01
5.05E+09	7.39E-04	-1.17E+02	5.77E-02	5.77E+01
5.10E+09	7.31E-04	-9.80E+01	5.76E-02	4.60E+01
5.15E+09	7.42E-04	-7.96E+01	5.75E-02	3.43E+01
5.20E+09	7.41E-04	-6.05E+01	5.72E-02	2.25E+01
5.25E+09	7.38E-04	-4.31E+01	5.71E-02	1.08E+01
5.30E+09	7.31E-04	-2.42E+01	5.69E-02	-8.43E-01
5.35E+09	7.34E-04	-2.90E+00	5.69E-02	-1.25E+01
5.40E+09	7.31E-04	1.91E+01	5.68E-02	-2.42E+01
5.45E+09	7.22E-04	3.81E+01	5.67E-02	-3.57E+01

5.49E+09	7.20E-04	5.57E+01	5.68E-02	-4.77E+01
5.54E+09	7.33E-04	7.06E+01	5.66E-02	-5.97E+01
5.59E+09	7.32E-04	8.72E+01	5.64E-02	-7.15E+01
5.64E+09	7.29E-04	1.06E+02	5.61E-02	-8.34E+01
5.69E+09	7.35E-04	1.22E+02	5.63E-02	-9.52E+01
5.74E+09	7.33E-04	1.36E+02	5.62E-02	-1.07E+02
5.79E+09	7.28E-04	1.53E+02	5.60E-02	-1.19E+02
5.84E+09	7.29E-04	1.70E+02	5.57E-02	-1.30E+02
5.89E+09	7.34E-04	-1.74E+02	5.58E-02	-1.42E+02
5.94E+09	7.43E-04	-1.59E+02	5.58E-02	-1.53E+02
5.99E+09	7.32E-04	-1.41E+02	5.57E-02	-1.65E+02
6.04E+09	7.39E-04	-1.24E+02	5.56E-02	-1.77E+02
6.09E+09	7.37E-04	-1.08E+02	5.55E-02	1.72E+02
6.14E+09	7.43E-04	-9.21E+01	5.54E-02	1.60E+02
6.19E+09	7.43E-04	-7.56E+01	5.53E-02	1.49E+02
6.24E+09	7.40E-04	-5.90E+01	5.52E-02	1.37E+02
6.29E+09	7.41E-04	-4.36E+01	5.50E-02	1.25E+02
6.34E+09	7.50E-04	-2.97E+01	5.48E-02	1.13E+02
6.39E+09	7.49E-04	-1.43E+01	5.45E-02	1.02E+02
6.44E+09	7.54E-04	1.76E+00	5.44E-02	9.00E+01
6.49E+09	7.45E-04	1.94E+01	5.42E-02	7.85E+01
6.54E+09	7.44E-04	3.64E+01	5.42E-02	6.70E+01
6.59E+09	7.43E-04	5.20E+01	5.40E-02	5.51E+01
6.64E+09	7.48E-04	6.40E+01	5.39E-02	4.32E+01
6.69E+09	7.50E-04	7.53E+01	5.39E-02	3.17E+01
6.74E+09	7.72E-04	8.28E+01	5.38E-02	1.98E+01
6.79E+09	7.82E-04	9.14E+01	5.39E-02	8.18E+00
6.84E+09	7.75E-04	9.84E+01	5.38E-02	-3.59E+00
6.89E+09	7.65E-04	1.05E+02	5.37E-02	-1.54E+01
6.94E+09	7.64E-04	1.09E+02	5.37E-02	-2.70E+01
6.99E+09	7.67E-04	1.15E+02	5.39E-02	-3.88E+01
7.03E+09	7.59E-04	1.23E+02	5.42E-02	-5.08E+01
7.08E+09	7.57E-04	1.28E+02	5.41E-02	-6.25E+01
7.13E+09	7.45E-04	1.32E+02	5.42E-02	-7.43E+01
7.18E+09	7.50E-04	1.35E+02	5.41E-02	-8.60E+01
7.23E+09	7.47E-04	1.36E+02	5.39E-02	-9.78E+01
7.28E+09	7.47E-04	1.40E+02	5.39E-02	-1.09E+02
7.33E+09	7.54E-04	1.47E+02	5.36E-02	-1.21E+02
7.38E+09	7.48E-04	1.52E+02	5.37E-02	-1.33E+02

7.43E+09	7.36E-04	1.59E+02	5.34E-02	-1.45E+02
7.48E+09	7.43E-04	1.66E+02	5.34E-02	-1.57E+02
7.53E+09	7.47E-04	1.75E+02	5.34E-02	-1.69E+02
7.58E+09	7.43E-04	-1.76E+02	5.32E-02	1.79E+02
7.63E+09	7.33E-04	-1.66E+02	5.35E-02	1.68E+02
7.68E+09	7.44E-04	-1.58E+02	5.32E-02	1.56E+02
7.73E+09	7.45E-04	-1.51E+02	5.33E-02	1.43E+02
7.78E+09	7.46E-04	-1.43E+02	5.30E-02	1.31E+02
7.83E+09	7.53E-04	-1.33E+02	5.29E-02	1.20E+02
7.88E+09	7.50E-04	-1.24E+02	5.28E-02	1.08E+02
7.93E+09	7.46E-04	-1.18E+02	5.29E-02	9.60E+01
7.98E+09	7.49E-04	-1.13E+02	5.26E-02	8.45E+01
8.03E+09	7.51E-04	-1.13E+02	5.24E-02	7.28E+01
8.08E+09	7.46E-04	-1.15E+02	5.22E-02	6.10E+01
8.13E+09	7.58E-04	-1.15E+02	5.21E-02	4.92E+01
8.18E+09	7.60E-04	-1.16E+02	5.21E-02	3.76E+01
8.23E+09	7.52E-04	-1.14E+02	5.18E-02	2.57E+01
8.28E+09	7.53E-04	-1.17E+02	5.18E-02	1.40E+01
8.33E+09	7.45E-04	-1.20E+02	5.14E-02	2.15E+00
8.38E+09	7.40E-04	-1.22E+02	5.11E-02	-9.32E+00
8.43E+09	7.23E-04	-1.24E+02	5.11E-02	-2.10E+01
8.48E+09	7.17E-04	-1.27E+02	5.08E-02	-3.26E+01
8.53E+09	7.30E-04	-1.31E+02	5.06E-02	-4.41E+01
8.57E+09	7.28E-04	-1.37E+02	5.05E-02	-5.58E+01
8.62E+09	7.23E-04	-1.39E+02	5.07E-02	-6.72E+01
8.67E+09	7.30E-04	-1.41E+02	5.04E-02	-7.90E+01
8.72E+09	7.32E-04	-1.41E+02	5.02E-02	-9.09E+01
8.77E+09	7.42E-04	-1.42E+02	4.99E-02	-1.02E+02
8.82E+09	7.33E-04	-1.44E+02	4.96E-02	-1.14E+02
8.87E+09	7.39E-04	-1.42E+02	4.95E-02	-1.26E+02
8.92E+09	7.37E-04	-1.40E+02	4.96E-02	-1.38E+02
8.97E+09	7.39E-04	-1.39E+02	4.95E-02	-1.49E+02
9.02E+09	7.34E-04	-1.36E+02	4.94E-02	-1.61E+02
9.07E+09	7.48E-04	-1.36E+02	4.93E-02	-1.72E+02
9.12E+09	7.58E-04	-1.39E+02	4.94E-02	1.76E+02
9.17E+09	7.55E-04	-1.42E+02	4.93E-02	1.64E+02
9.22E+09	7.56E-04	-1.46E+02	4.92E-02	1.52E+02
9.27E+09	7.52E-04	-1.50E+02	4.91E-02	1.40E+02
9.32E+09	7.55E-04	-1.53E+02	4.90E-02	1.28E+02

9.37E+09	7.58E-04	-1.57E+02	4.89E-02	1.16E+02
9.42E+09	7.57E-04	-1.60E+02	4.90E-02	1.04E+02
9.47E+09	7.63E-04	-1.62E+02	4.89E-02	9.23E+01
9.52E+09	7.60E-04	-1.63E+02	4.87E-02	8.08E+01
9.57E+09	7.53E-04	-1.63E+02	4.87E-02	6.92E+01
9.62E+09	7.58E-04	-1.68E+02	4.88E-02	5.74E+01
9.67E+09	7.63E-04	-1.70E+02	4.89E-02	4.56E+01
9.72E+09	7.58E-04	-1.72E+02	4.86E-02	3.39E+01
9.77E+09	7.53E-04	-1.74E+02	4.84E-02	2.21E+01
9.82E+09	7.54E-04	-1.80E+02	4.86E-02	1.03E+01
9.87E+09	7.60E-04	1.74E+02	4.87E-02	-1.68E+00
9.92E+09	7.64E-04	1.66E+02	4.82E-02	-1.35E+01
9.97E+09	7.54E-04	1.60E+02	4.80E-02	-2.52E+01
1.00E+10	7.59E-04	1.52E+02	4.80E-02	-3.74E+01
1.01E+10	7.62E-04	1.43E+02	4.78E-02	-4.90E+01
1.01E+10	7.61E-04	1.36E+02	4.78E-02	-6.11E+01
1.02E+10	7.54E-04	1.28E+02	4.80E-02	-7.29E+01
1.02E+10	7.67E-04	1.24E+02	4.80E-02	-8.48E+01
1.03E+10	7.68E-04	1.18E+02	4.79E-02	-9.63E+01
1.03E+10	7.71E-04	1.16E+02	4.78E-02	-1.08E+02
1.04E+10	7.68E-04	1.14E+02	4.78E-02	-1.20E+02
1.04E+10	7.71E-04	1.11E+02	4.79E-02	-1.32E+02
1.05E+10	7.61E-04	1.11E+02	4.77E-02	-1.44E+02
1.05E+10	7.65E-04	1.11E+02	4.73E-02	-1.56E+02
1.06E+10	7.65E-04	1.10E+02	4.69E-02	-1.67E+02
1.06E+10	7.62E-04	1.09E+02	4.68E-02	-1.79E+02
1.07E+10	7.48E-04	1.13E+02	4.66E-02	1.69E+02
1.07E+10	7.45E-04	1.15E+02	4.65E-02	1.58E+02
1.08E+10	7.27E-04	1.20E+02	4.64E-02	1.46E+02
1.08E+10	7.38E-04	1.27E+02	4.60E-02	1.34E+02
1.09E+10	7.41E-04	1.34E+02	4.56E-02	1.23E+02
1.09E+10	7.54E-04	1.43E+02	4.55E-02	1.11E+02
1.10E+10	7.43E-04	1.54E+02	4.53E-02	9.93E+01
1.10E+10	7.41E-04	1.65E+02	4.49E-02	8.74E+01
1.11E+10	7.45E-04	1.74E+02	4.45E-02	7.60E+01
1.11E+10	7.48E-04	-1.75E+02	4.49E-02	6.43E+01
1.12E+10	7.53E-04	-1.64E+02	4.47E-02	5.26E+01
1.12E+10	7.60E-04	-1.52E+02	4.45E-02	4.12E+01
1.13E+10	7.54E-04	-1.39E+02	4.46E-02	2.98E+01

1.13E+10	7.66E-04	-1.30E+02	4.43E-02	1.76E+01
1.14E+10	7.50E-04	-1.22E+02	4.47E-02	6.01E+00
1.14E+10	7.50E-04	-1.16E+02	4.46E-02	-5.19E+00
1.15E+10	7.66E-04	-1.12E+02	4.46E-02	-1.69E+01
1.15E+10	7.68E-04	-1.09E+02	4.44E-02	-2.84E+01
1.16E+10	7.57E-04	-1.08E+02	4.43E-02	-4.00E+01
1.16E+10	7.54E-04	-1.05E+02	4.44E-02	-5.18E+01
1.17E+10	7.50E-04	-1.02E+02	4.40E-02	-6.38E+01
1.17E+10	7.56E-04	-9.88E+01	4.41E-02	-7.47E+01
1.18E+10	7.51E-04	-9.32E+01	4.42E-02	-8.66E+01
1.18E+10	7.62E-04	-8.58E+01	4.41E-02	-9.85E+01
1.19E+10	7.58E-04	-8.07E+01	4.40E-02	-1.10E+02
1.19E+10	7.56E-04	-7.53E+01	4.40E-02	-1.22E+02
1.20E+10	7.62E-04	-6.76E+01	4.39E-02	-1.34E+02
1.20E+10	7.60E-04	-5.82E+01	4.37E-02	-1.46E+02
1.21E+10	7.56E-04	-4.57E+01	4.40E-02	-1.58E+02
1.21E+10	7.54E-04	-3.54E+01	4.42E-02	-1.70E+02
1.22E+10	7.51E-04	-2.48E+01	4.41E-02	1.78E+02
1.22E+10	7.39E-04	-1.42E+01	4.38E-02	1.66E+02
1.23E+10	7.49E-04	-4.57E+00	4.36E-02	1.55E+02
1.23E+10	7.54E-04	7.91E+00	4.34E-02	1.43E+02
1.24E+10	7.51E-04	2.21E+01	4.36E-02	1.31E+02
1.24E+10	7.51E-04	3.72E+01	4.37E-02	1.19E+02
1.24E+10	7.71E-04	5.22E+01	4.37E-02	1.08E+02
1.25E+10	7.69E-04	6.53E+01	4.35E-02	9.60E+01
1.25E+10	7.70E-04	8.03E+01	4.35E-02	8.40E+01
1.26E+10	7.70E-04	9.42E+01	4.37E-02	7.23E+01
1.26E+10	7.73E-04	1.07E+02	4.35E-02	6.01E+01
1.27E+10	7.63E-04	1.18E+02	4.34E-02	4.87E+01
1.27E+10	7.73E-04	1.30E+02	4.34E-02	3.73E+01
1.28E+10	7.64E-04	1.40E+02	4.37E-02	2.53E+01
1.28E+10	7.66E-04	1.50E+02	4.37E-02	1.39E+01
1.29E+10	7.63E-04	1.57E+02	4.36E-02	2.24E+00
1.29E+10	7.67E-04	1.63E+02	4.32E-02	-9.15E+00
1.30E+10	7.58E-04	1.69E+02	4.31E-02	-2.13E+01
1.30E+10	7.65E-04	1.72E+02	4.32E-02	-3.31E+01
1.31E+10	7.49E-04	1.77E+02	4.35E-02	-4.50E+01
1.31E+10	7.56E-04	-1.77E+02	4.32E-02	-5.71E+01
1.32E+10	7.58E-04	-1.70E+02	4.30E-02	-6.85E+01

1.32E+10	7.56E-04	-1.63E+02	4.28E-02	-8.04E+01
1.33E+10	7.49E-04	-1.56E+02	4.31E-02	-9.22E+01
1.33E+10	7.42E-04	-1.52E+02	4.32E-02	-1.04E+02
1.34E+10	7.44E-04	-1.51E+02	4.32E-02	-1.16E+02
1.34E+10	7.43E-04	-1.50E+02	4.32E-02	-1.27E+02
1.35E+10	7.38E-04	-1.50E+02	4.31E-02	-1.39E+02
1.35E+10	7.43E-04	-1.48E+02	4.30E-02	-1.50E+02
1.36E+10	7.40E-04	-1.44E+02	4.26E-02	-1.62E+02
1.36E+10	7.43E-04	-1.40E+02	4.23E-02	-1.74E+02
1.37E+10	7.42E-04	-1.38E+02	4.19E-02	1.75E+02
1.37E+10	7.42E-04	-1.35E+02	4.20E-02	1.63E+02
1.38E+10	7.53E-04	-1.27E+02	4.17E-02	1.51E+02
1.38E+10	7.57E-04	-1.17E+02	4.16E-02	1.39E+02
1.39E+10	7.51E-04	-1.04E+02	4.15E-02	1.27E+02
1.39E+10	7.54E-04	-9.06E+01	4.17E-02	1.15E+02
1.40E+10	7.59E-04	-7.80E+01	4.17E-02	1.03E+02
1.40E+10	7.55E-04	-6.42E+01	4.16E-02	9.15E+01
1.41E+10	7.54E-04	-4.72E+01	4.18E-02	7.96E+01
1.41E+10	7.50E-04	-2.87E+01	4.17E-02	6.80E+01
1.42E+10	7.51E-04	-1.11E+01	4.13E-02	5.65E+01
1.42E+10	7.47E-04	6.88E+00	4.14E-02	4.48E+01
1.43E+10	7.51E-04	2.76E+01	4.15E-02	3.32E+01
1.43E+10	7.46E-04	4.69E+01	4.14E-02	2.12E+01
1.44E+10	7.42E-04	6.80E+01	4.16E-02	9.81E+00
1.44E+10	7.41E-04	9.03E+01	4.15E-02	-1.97E+00
1.45E+10	7.48E-04	1.13E+02	4.15E-02	-1.38E+01
1.45E+10	7.48E-04	1.34E+02	4.15E-02	-2.56E+01
1.46E+10	7.48E-04	1.55E+02	4.13E-02	-3.72E+01
1.46E+10	7.54E-04	1.77E+02	4.10E-02	-4.89E+01
1.47E+10	7.55E-04	-1.61E+02	4.08E-02	-6.05E+01
1.47E+10	7.63E-04	-1.41E+02	4.06E-02	-7.25E+01
1.48E+10	7.60E-04	-1.21E+02	4.06E-02	-8.43E+01
1.48E+10	7.42E-04	-1.04E+02	4.05E-02	-9.63E+01
1.49E+10	7.43E-04	-8.42E+01	4.04E-02	-1.08E+02
1.49E+10	7.41E-04	-6.47E+01	4.02E-02	-1.20E+02
1.50E+10	7.48E-04	-4.66E+01	4.00E-02	-1.32E+02
1.50E+10	7.46E-04	-3.18E+01	3.99E-02	-1.44E+02
1.51E+10	7.51E-04	-1.69E+01	3.96E-02	-1.57E+02
1.51E+10	7.46E-04	-2.77E+00	3.92E-02	-1.69E+02

1.52E+10	7.42E-04	1.18E+01	3.91E-02	1.79E+02
1.52E+10	7.36E-04	2.55E+01	3.94E-02	1.67E+02
1.53E+10	7.45E-04	3.64E+01	3.91E-02	1.55E+02
1.53E+10	7.37E-04	4.88E+01	3.89E-02	1.43E+02
1.54E+10	7.40E-04	5.98E+01	3.85E-02	1.32E+02
1.54E+10	7.44E-04	7.29E+01	3.84E-02	1.20E+02
1.55E+10	7.36E-04	8.38E+01	3.85E-02	1.08E+02
1.55E+10	7.26E-04	9.88E+01	3.85E-02	9.61E+01
1.56E+10	7.27E-04	1.15E+02	3.84E-02	8.48E+01
1.56E+10	7.24E-04	1.29E+02	3.82E-02	7.33E+01
1.57E+10	7.27E-04	1.40E+02	3.82E-02	6.16E+01
1.57E+10	7.14E-04	1.51E+02	3.79E-02	4.95E+01
1.58E+10	7.19E-04	1.60E+02	3.79E-02	3.84E+01
1.58E+10	7.16E-04	1.72E+02	3.77E-02	2.78E+01
1.59E+10	7.21E-04	-1.76E+02	3.76E-02	1.57E+01
1.59E+10	7.29E-04	-1.67E+02	3.75E-02	4.29E+00
1.60E+10	7.35E-04	-1.59E+02	3.74E-02	-7.22E+00
1.60E+10	7.38E-04	-1.52E+02	3.76E-02	-1.81E+01
1.61E+10	7.35E-04	-1.45E+02	3.71E-02	-3.01E+01
1.61E+10	7.46E-04	-1.38E+02	3.70E-02	-4.18E+01
1.62E+10	7.46E-04	-1.31E+02	3.71E-02	-5.34E+01
1.62E+10	7.54E-04	-1.25E+02	3.72E-02	-6.51E+01
1.63E+10	7.44E-04	-1.20E+02	3.74E-02	-7.69E+01
1.63E+10	7.38E-04	-1.19E+02	3.73E-02	-8.76E+01
1.64E+10	7.44E-04	-1.18E+02	3.73E-02	-9.94E+01
1.64E+10	7.47E-04	-1.20E+02	3.68E-02	-1.11E+02
1.65E+10	7.31E-04	-1.20E+02	3.69E-02	-1.23E+02
1.65E+10	7.39E-04	-1.20E+02	3.69E-02	-1.34E+02
1.66E+10	7.24E-04	-1.22E+02	3.70E-02	-1.46E+02
1.66E+10	7.20E-04	-1.22E+02	3.68E-02	-1.58E+02
1.67E+10	7.21E-04	-1.22E+02	3.66E-02	-1.70E+02
1.67E+10	7.22E-04	-1.25E+02	3.64E-02	1.78E+02
1.68E+10	7.16E-04	-1.32E+02	3.61E-02	1.67E+02
1.68E+10	7.14E-04	-1.36E+02	3.59E-02	1.55E+02
1.69E+10	7.17E-04	-1.42E+02	3.60E-02	1.43E+02
1.69E+10	7.28E-04	-1.46E+02	3.59E-02	1.32E+02
1.70E+10	7.46E-04	-1.49E+02	3.60E-02	1.20E+02
1.70E+10	7.47E-04	-1.51E+02	3.62E-02	1.09E+02
1.71E+10	7.47E-04	-1.51E+02	3.59E-02	9.70E+01

1.71E+10	7.48E-04	-1.49E+02	3.55E-02	8.53E+01
1.72E+10	7.36E-04	-1.48E+02	3.56E-02	7.38E+01
1.72E+10	7.33E-04	-1.50E+02	3.59E-02	6.22E+01
1.73E+10	7.30E-04	-1.52E+02	3.60E-02	5.07E+01
1.73E+10	7.41E-04	-1.55E+02	3.59E-02	3.92E+01
1.74E+10	7.48E-04	-1.55E+02	3.57E-02	2.76E+01
1.74E+10	7.48E-04	-1.54E+02	3.55E-02	1.57E+01
1.75E+10	7.47E-04	-1.54E+02	3.55E-02	3.98E+00
1.75E+10	7.42E-04	-1.55E+02	3.56E-02	-7.80E+00
1.76E+10	7.43E-04	-1.59E+02	3.59E-02	-2.02E+01
1.76E+10	7.43E-04	-1.65E+02	3.59E-02	-3.23E+01
1.77E+10	7.41E-04	-1.69E+02	3.58E-02	-4.43E+01
1.77E+10	7.40E-04	-1.74E+02	3.59E-02	-5.62E+01
1.78E+10	7.45E-04	-1.78E+02	3.60E-02	-6.81E+01
1.78E+10	7.35E-04	1.77E+02	3.60E-02	-7.99E+01
1.79E+10	7.38E-04	1.71E+02	3.58E-02	-9.18E+01
1.79E+10	7.34E-04	1.62E+02	3.55E-02	-1.04E+02
1.80E+10	7.33E-04	1.54E+02	3.56E-02	-1.15E+02
1.80E+10	7.26E-04	1.43E+02	3.54E-02	-1.27E+02
1.81E+10	7.25E-04	1.32E+02	3.52E-02	-1.38E+02
1.81E+10	7.16E-04	1.19E+02	3.50E-02	-1.50E+02
1.82E+10	7.16E-04	1.05E+02	3.50E-02	-1.62E+02
1.82E+10	7.15E-04	8.97E+01	3.49E-02	-1.73E+02
1.83E+10	7.06E-04	7.28E+01	3.46E-02	1.76E+02
1.83E+10	6.96E-04	5.45E+01	3.43E-02	1.64E+02
1.84E+10	6.95E-04	3.57E+01	3.43E-02	1.54E+02
1.84E+10	6.92E-04	1.67E+01	3.38E-02	1.43E+02
1.85E+10	6.87E-04	-3.14E+00	3.37E-02	1.32E+02
1.85E+10	6.82E-04	-2.45E+01	3.35E-02	1.22E+02
1.86E+10	6.81E-04	-4.49E+01	3.36E-02	1.11E+02
1.86E+10	6.76E-04	-6.55E+01	3.39E-02	1.01E+02
1.87E+10	6.69E-04	-8.81E+01	3.39E-02	9.08E+01
1.87E+10	6.66E-04	-1.12E+02	3.40E-02	8.08E+01
1.88E+10	6.54E-04	-1.34E+02	3.38E-02	7.10E+01
1.88E+10	6.52E-04	-1.57E+02	3.38E-02	6.10E+01
1.89E+10	6.51E-04	-1.78E+02	3.38E-02	5.19E+01
1.89E+10	6.50E-04	1.58E+02	3.39E-02	4.24E+01
1.90E+10	6.40E-04	1.35E+02	3.38E-02	3.35E+01
1.90E+10	6.30E-04	1.12E+02	3.38E-02	2.44E+01

1.91E+10	6.28E-04	9.08E+01	3.38E-02	1.64E+01
1.91E+10	6.18E-04	7.12E+01	3.39E-02	8.04E+00
1.92E+10	6.15E-04	5.16E+01	3.38E-02	-8.10E-02
1.92E+10	6.14E-04	3.11E+01	3.38E-02	-8.30E+00
1.93E+10	6.11E-04	9.32E+00	3.35E-02	-1.62E+01
1.93E+10	6.02E-04	-1.17E+01	3.37E-02	-2.42E+01
1.94E+10	5.98E-04	-3.26E+01	3.37E-02	-3.23E+01
1.94E+10	5.94E-04	-5.21E+01	3.37E-02	-4.04E+01
1.95E+10	5.83E-04	-7.25E+01	3.37E-02	-4.84E+01
1.95E+10	5.77E-04	-9.11E+01	3.34E-02	-5.62E+01
1.96E+10	5.76E-04	-1.12E+02	3.33E-02	-6.35E+01
1.96E+10	5.76E-04	-1.34E+02	3.33E-02	-7.13E+01
1.97E+10	5.77E-04	-1.55E+02	3.32E-02	-7.85E+01
1.97E+10	5.70E-04	-1.75E+02	3.32E-02	-8.55E+01
1.98E+10	5.65E-04	1.66E+02	3.32E-02	-9.24E+01
1.98E+10	5.55E-04	1.48E+02	3.29E-02	-9.95E+01
1.99E+10	5.48E-04	1.28E+02	3.30E-02	-1.07E+02
1.99E+10	5.39E-04	1.06E+02	3.28E-02	-1.13E+02
2.00E+10	5.33E-04	8.60E+01	3.27E-02	-1.20E+02
2.00E+10	5.23E-04	6.61E+01	3.25E-02	-1.26E+02

A.2. ADS Optimizer Settings

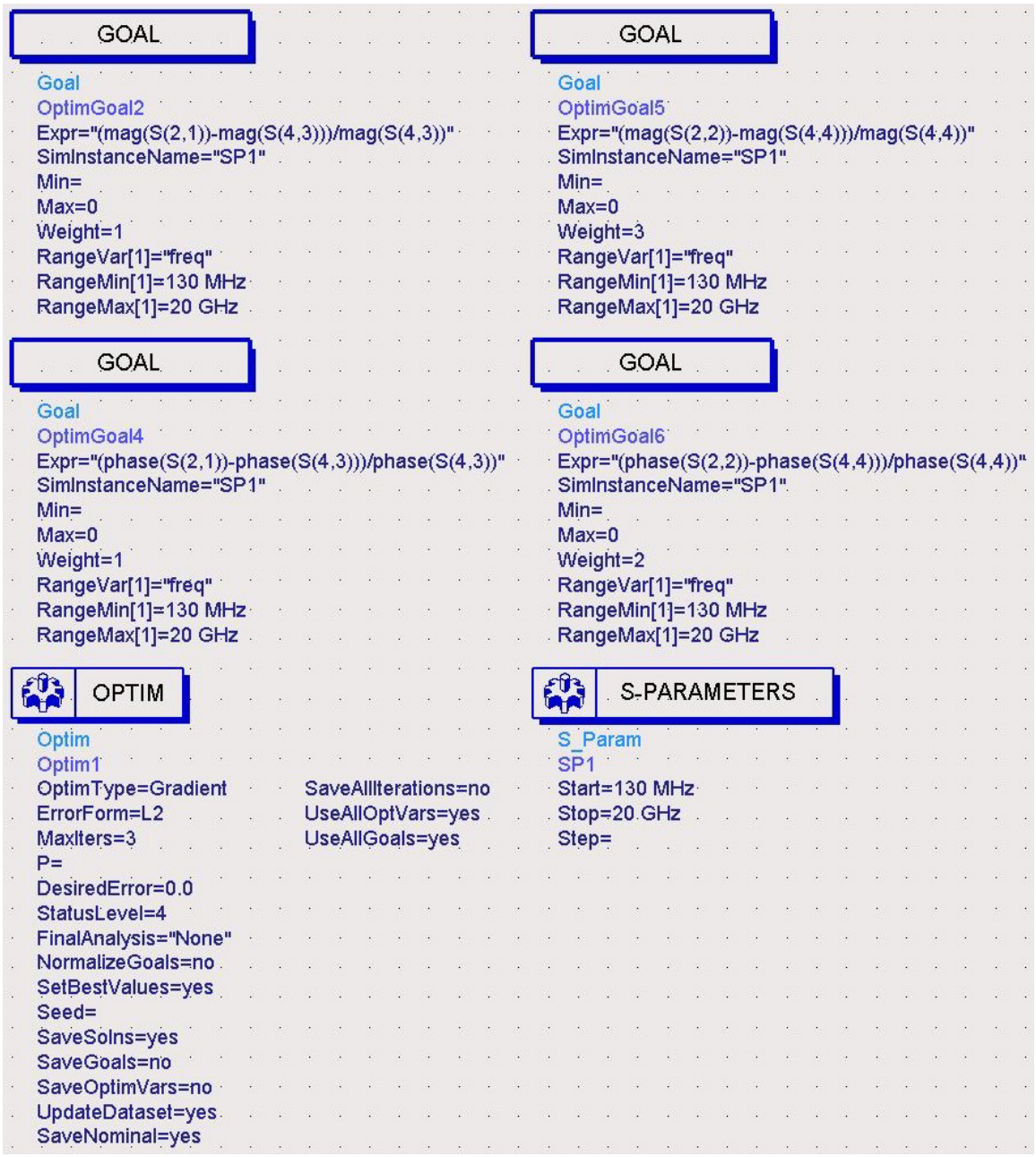

REFERENCES

[1] S. B. Alexander and SPIE, "Optical Communication Receiver Design," The Society of Photo-Optical Instrumentation Engineers, 1997.

[2] S. Donati, "Devices, Circuits, and Applications," Prentice Hall, 2000.

[3] S. Kasap, "Optoelectronics and Photonics: Principles and Practices," Prentice Hall, 2000.

[4] R. Poddar, E. Moon, M. A. Brooke, and N. M. Jokerst, "Accurate, rapid, high frequency empirically based predictive modeling of arbitrary geometry planar resistive passive devices," *IEEE Trans. Components, Packaging, and Manufacturing Technology,* Vol. 21 Issue: 2 (1998), pp. 177 –183.

[5] J.W. Shi, C.K. Sun, "Theory and design of a tapered line distributed photodetector," Journal of Lightwave Technology, vol. 20, no.11, pp. 1942 -1950, 2002.

[6] E. Sano, "Two-dimensional ensemble Monte Carlo calculation of pulse responses of submicrometer GaAs metal-semiconductor-metal photodetectors," IEEE Transactions on Electron Devices, vol. 38, no. 9, pp. 2075 -2081, 1991.

[7] J.S. Wang, C.C. Teng, J.R. Middleton, M. Feng, "Process integration and optimization of GaAs MESFET and MSM based opto-electronics integrated circuit (OEIC) using statistical experimental design techniques," IEEE/CPMT International Electronics Manufacturing Technology Symposium, pp. 471 –479, Oct. 1995.

[8] P. Bhattacharya, "Semiconductor Optoelectronic Devices" Prentice Hall, 1997.

[9] M. Ito, O. Wada, "Low dark current GaAs metal-semiconductor-metal (MSM) photodiodes using Wsixcontacts*," IEEE Journal of Quantum Electronics*, vol. 22, no.7, pp. 1073- 1077,1986.

[10] S.V. Averine, Y.C. Chan, Y.L. Lam, O. Bondarenko, R. Sachot, "Ultrafast heterobarrier MSM-photodiode structures," Proceedings Conference on Optoelectronic and Microelectronic Materials and Devices, pp. 137 –140, 2000.

[11] A. Xiang, W. Wohlmuth, P. Fay, S.M. Kang, I. Adesida, "Modeling InGaAs MSM photodetector for circuit-level simulation," Journal of Lightwave Technology, vol. 14, no.5, pp. 7115 -723, 1996.

[12] T.O. Korner, "Combined optical and electric simulation of metal-semiconductor-metal photodetectors," IEE Proceeding of Optoelectronics, vol.147, no. 2, pp. 89 –95,

2000.

[13] J. Burm, K.I. Litvin, G.H. Martin, W.J. Schaff, L.F. Eastman, "Monolithic

millimeter wave optical receivers," IEEE Transactions on Microwave Theory and Techniques, vol. 44, no. 11, pp. 1984 –1989, 1996.

[14] Y.C. Lim, R.A. Moore, "Properties of Alternately Charged Coplanar Parallel Strips by Conformal Mappings," IEEE Transactions on Electron Devices, vol. 15, no. 3, pp. 173-180, 1968.

[15] L.W. Cahill, E. Stumpf, "Analysis of high speed interdigitated MSM photodetectors," IEEE Lasers and Electro-Optics Society Annual Meeting, pp.217-218, 1993.

[16] J.W. Chen, D.K. Kim, M.B. Das, "Transit-time limited high-frequency response characteristics of MSM photodetectors," IEEE Transactions on Electron Devices, vol. 43, no.11,pp.1838–1843,1996.

[17] E.H. Bottcher, D. Kuhl, F. Hieronymi, E. Droge, T. Wolf, D. Bimberg, "Ultrafast semiinsulating InP:Fe-InGaAs:Fe-InP:Fe MSM photodetectors: modeling and performance," IEEE Journal of Quantum Electronics, vol. 28, no. 10, pp. 2343 –2357, 1992.

[18] B.J. Van Zeghbroeck, "Analysis of picosecond and subpicosecond MSM photodiodes with very low bias voltage," IEEE Transactions on Electron Devices, vol. 35, no. 12, pp.2433, 1988.

[19] J.B.D. Soole, H. Schumacher, "Transit-time limited frequency response of InGaAs MSM photodetectors," IEEE Transactions on Electron Devices, vol. 37, no. 11, pp. 2285 -2291, 1990.

[20] A.F. Salem, K.F. Brennan, "Theoretical study of the response of InGaAs metal-semiconductor-metal photodetectors," IEEE Journal of Quantum Electronics, vol. 31, no. 5, pp. 944-953, 1995.

[21] S. Kollakowski, H. Krautle, C. Lemm, E.H. Bottcher, D. Bimberg, "Waveguide-integrated InP/InGaAs/InAlGaAs MSM photodetectors," International Conference on Indium Phosphide and Related Materials, pp. 223-225, 1996.

[22] M.B. Das, "Optoelectronic detectors and receivers: speed and sensitivity limits," Conference on Optoelectronic and Microelectronic Materials Devices, pp. 15-22, 1999.

[23] H.H. Wehmann, G.P. Tang, R. Klockenbrink, A. Schlachetzki, "Dark-current analysis of InGaAs-MSM-photodetectors on silicon substrates," IEEE Transactions on Electron Devices, vol. 43, no. 9, pp. 1505 -1509, 1996.

[24] M. Djebari, G. Kompa, A. Stolze, "A Simplified Physics-based Quasi-static MSM Photodiode Model," 27th European Microwave Conference and Exhibition, pp. 324 –327, 1997.

[25] W.C. Koscielniak, J.L. Pelouard, R.M. Kolbas, M.A. Littlejohn, "Dark current characteristics of GaAs metal-semiconductor-metal (MSM) photodetectors," IEEE Transactions on Electron Devices, vol. 37, no. 7, pp. 1623 -1629, 1990.

[26] M. Vrazel, J.J. Chang, M. Brooke, N.M. Jokerst, G. Dagnali, A. Brown, "Alignment tolerant hybrid photoreceivers using inverted MSMs," Digest of the LEOS Summer Topical Meetings, pp. I23 -I24, 2000.

[27] W.C. Koscielniak, J.L. Pelouard, M.A. Littlejohn, "Intrinsic and extrinsic response of GaAs metal-semiconductor-metal photodetectors," IEEE Photonics Technology Letters, vol. 2, no. 2, pp.125-127, 1990.

[28] A.W. Sarto, B.J. Van Zeghbroeck, "Photocurrents in a metal-semiconductor-metal photodetector," IEEE Journal of Quantum Electronics, vol. 33, no. 12, pp. 2188 –2194, 1997.

[29] Lee, Myunghee, "A quasi-monolithic optical receiver using a standard digital CMOS technology," Ph.D. Thesis, School of Electrical and Computer Engineering, Georgia Institute of Technology, 1996.

[30] R.J. Baker, H.W. Li, D.E. Boyce, "CMOS Circuit design, Layout, and Simulation" IEEE Press, 2000.

[31] C. P. Yue and S. S. Wong, "On-chip spiral inductors with patterned ground shields for Si-based RF IC's," in *1997 Symp. VLSI Circuits Dig. Tech. Papers*, 1997, pp. 85–86.

[32] S. S. Mohan and T. H. Lee, "A 2.125 Gbaud 1.6 kw transimpedance preamplifier in 0.5 mm CMOS," in *Custom Integrated circuits Conf. Dig. Tech. Papers*, May 1999, pp. 513–516.

[33] S. S. Mohan, M.D.M. Hershenson, S.P. Boyd, T.H. Lee, "Bandwidth Extension in CMOS with Optimized On-chip Inductors," IEEE Journal of Solid-State Circuits, vol.35, no. 3, pp. 346-355, 2000.

[34] Alan Mickelson, " Optoelectronic Packaging John Wiley & Sons, 1997.

[35] S. E. Miller and I. P. Kaminow, Optical fiber telecommunications II, Academic Press, 1988.

[36] D. J. H. Maclean, "Optical Line Systems" John Wiley & Sons, 1996.

[37] B. Wilson, Z. Ghassemlloy, and I. Darwazeh, Analogue Optical Fibre Communication, IEE Press, U.K., 1995.

[38] Y. Suematsu and K. Iga, "Introduction to Optical Fiber Communication" John Wiley & Sons, 1982.

[39] P. E. Green, Jr., Fiber Optic Networks, pp. 273-277, Prentice-Hall, Englewood Cliffs, N.J., 1993.

[40] J. P. Powers, "An Introduction to fiber optic systems" 2nd Edition, McGraw-Hill Companies Inc. 1997.

[41] Y. Suematsu and K. Iga, "Introduction to Optical Fiber Communication" John Wiley & Sons, 1982.

[42] D.E. Carlton, K.R. Gleason, E.W. Strid, ”Microwave Wafer Probing,” Cascade Microtech, Technical Feature, 1985.

[43] “ A Guide to Better Vector Network Analyzer Calibration for Probe-Tip Measurements” Cascade Microtech, Technical Brief.

[44] “On-wafer Vector Network Analyzer Calibration and Measurements,” Cascade Microtech, Application Note.

[45] A. Fraser, R. Gleason, E.W. Stride, “GHz On-wafer Probing Calibration Methods,” IEEE Bipolar Circuit and Technology Meeting, pp.154-157, 1988.

[46] A. Dehe, H. Klingbeil, C. Weil, ”Membrane Supported Coplanar Wave guides,” Institute für Hochfrequenztechnik TUD 55, pp. 55-58, 1997.

[47] K. Naishadham, “On-board Probing of Broadband RF Amplifiers Using CPW Interconnects,” IEEE RFICS, pp. 129-132, 2001.

[48] W. R. Eisenstadt, O. Bell, “ High-Frequency Characterization and Modeling of Polysilicon and Diffusion Lines,” IEEE Custom Integrated Circuits Conference, pp. 51-54, 1991.

[49] M. Nishimoto, M. Hamai, J. Laskar, R. Lai, “On-wafer Calibration Techniques and Applications at V-band,” IEEE Microwave and Guided Wave Letters, vol. 4, no. 11, pp.370-372, 1994.

[50] A. Pham, J. Laskar, G. Zhou, B. hutchinson, “Development of a Surface Mountable Plastic Package Characterization Technique,” ARFTG Conference, pp.147-149, 1996.

[51] C. Chun, A.V. Pham, J. Laskar, B. Hutchison, “Development of Microwave Package Models Utilizing On-wafer Characterization Techniques,”, IEEE Trans. MTT, vol. 45, no. 10, pp.1948-1954, 1997.

[52] J. Pia, W. Struble, F. Colomb, “On-wafer Calibration Techniques for Measurement of Microwave Circuits and Devices on Thin Substrates, ”IEEE MTT-S. Digest, pp.1045-1048, 1995.

[53] A. Davison, E. Strid, K. Jones, “Achieving Greater On-wafer S-parameter Accuracy with the LRM Calibration Technique,” Cascade Microtech, Application Note.

[54] D. F. Williams, R. B. Marks, “LRM Probe-Tip Calibrations using Nonideal Standards,” IEEE Trans. MTT vol. 43, pp.466-469, Feb. 1995.

[55] E. F. Calendar, ”Measurement-Based Modeling of Microwave Transistor Package and Test-Fixture for Device S-parameter Deembedding,” *Proc 37th Midwest Symposium on Circuits and Systems*, 1994, pp. 1227 –1230.

[56] Pozar, D. M. *et al*, Microwave Engineering, Wiley (New York, 1998), pp. 206-213.

[57] P. J. van Wijnen, H. R. Claessen, and E. A. Wolsheimer, “A new straightforward calibration and correction procedure for ‘on wafer’ high frequency S -parameter

measurements (45 MHz–18 GHz)," *IEEE Bipolar Circuits Technology Meetin*g, 1987, pp. 70–73.

[58] M. C. A. M. Koolen, J. A. M. Geelen, and M. P. J. G. Versleijen, "An improved de-embedding technique for on-wafer high-frequency characterization," *IEEE Bipolar Circuits Techno. Meetin*g, 1991, pp. 188–191.

[59] H. Chow and D. Burk, "A three step method for the de-embedding of high frequency S -parameter measurements," *IEEE Trans. Electron Device*s, Vol. 38, No. 6 (1991), pp. 1371–1375.

[60] E. P. Vandamme, D. M. M.-P. Schreurs, and C. V. Dinther, "Improved Three-Step De-Embedding Method to Accurately Account for the Influence of Pad Parasitics in Silicon On-Wafer RF Test-Structures," *IEEE Trans. Electron Device*s, Vol. 48, No. 4 (2001), pp. 737–742.

[61] S. Lee, B. R. Ryum, and S. W. Kang, "A new parameter extraction technique for small-signal equivalent circuit of polysilicon emitter bipolar transistors," *IEEE Trans. Electron Device*s, Vol. 41, No. 2 (1994), pp. 233–238.

[62] W. Ryu, S.H. Baik, H. Kim, J. Kim, M. S., and J. Kim, "Embedded Microstrip interconnection Lines for Gigahertz Digital Circuits," *IEEE Trans. Advanced Packing*, Vol. 23, No. 3 (2000), pp. 495–503.

[63] C. H. Chen and M. J. Deen, "A General Noise and -Parameter Deembedding procedure for On-Wafer High-Frequency Noise Measurements of MOSFETs," *IEEE Trans. Microwave Theory and Techniques*, Vol. 49, No. 5 (2001), pp. 1004–1005.

[64] L. Schimpf, B. Benna, and D. Proetel, "A new approach to characterize substrate losses of on-chip inductors," *Proc International Conference on Microelectronic Test Structures*, 2001, pp. 115 –118.

[65] J. B. D. Soole, H. Schumacher, H.P. LeBlanc, R. Bhat, M.A. Koza, "High performance $In_{0.52}Al_{0.48}As/In_{0.53}$ $Ga_{0.47}As$ metal-semiconductor-metal photodetectors," International Electron Devices Meeting, pp. 713-716, 1989.

[66] P. Fay, M. Arafa, W.A. Wohlmuth, C. Caneau, S. Chandrasekhar, I. Adesida, "Design, fabrication, and performance of high-speed monolithically integrated InAlAs/InGaAs/InP MSM/HEMT photoreceivers," Journal of Lightwave Technology, vol. 15, no. 10, pp. 1871 –1879, 1997.

[67] Bruce Carter, "A Current Feedback Op-Amp Circuit Collection," Texas Instruments, Application Report, SLOA066, Aug. 2001.

[68] Bonnie baker, " Tuning in Amplifiers," Burr-Brown, Application Bulletin, AB-105 1996.

[69] T. Miracco, G. Brehm, W. Reinisch, "Companies Collaborate to Streamline MMIC Design and Development," Applied Microwave & Wireless, pp. 60-67, June 2002.

[70] J. M. Castilo, A.D. Sanchez, "A BiCMOS Transimpedance Amplifier for High Frequency Communication Systems," ELECTRO pp. 297-300, 2001.

[71] T. Wang, B. Ehreman, "Compensate Transimpedance Amplifiers Intuitively," Burr Brown, Application Bulletin, AB-050, 1993.

[72] A. A. Abidi, "On the choice of optimum FET size in wide-band transimpedance amplifiers," *J. Lightwave Techno.*, vol. 6, pp. 64–66, Jan. 1988.

[73] C. H. Chen, and M. J. Deen, "A general procedure for high-frequency noise parameter de-embedding of MOSFETs by taking the capacitive effects of metal interconnections into account ," *Proc International Conference on Microelectronic Test Structures*, 2001, pp. 109 –114.

[74] L. A. Carastro, R. Poddar, E. Moon, M. A. Brooke, and N. M. Jokerst, "Passive device modeling methodology using nonlinear optimization," *Proc International Symposium on Circuits and Systems*, 1999, pp. 53 –56.

[75] A. E. Ruehli and A. C. Cangellaris, "Progress in the Methodologies for the Electrical Modeling of Interconnects and Electronic Packages," Proceeding of the IEEE, vol. 89, no. 5, 2001, pp.740-771.

[76] M. E. Verbeek, "Partial Element Equivalent Circuit (PEEC) Models for On-chip Passives and Interconnects," pp.1-21.

[78] H. Heeb and A. E. Ruehli, "Three-dimensional Interconnect Analysis using Partial Element Equivalent Circuits," IEEE Transactions on Circuits and Systems, vol. 39, no. 11, 1992, pp.974-982.

[79] A. E. Ruehli, "Equivalent Circuit Models for Three-dimensional Multiconductor Systems," IEEE Transactions on Microwave Theory and Techniques, vol. 22, no. 3, 1974, pp. 216-221.

[80] D. G. Swanson, "Simulating EM Fields," IEEE Spectrum Nov. 1991, pp.34-37.

[81] G. Antonini and A. E. Ruehli, "Fast Multiple and Multifunction PEEC Methods," IEEE Transactions on Mobile Computing, vol. 2, no. 4, 2003, pp. 288-298.

[82] J. Cullum, A. E. Ruehli, and T. Zhang, "A Method for Reduced-order Modeling and Simulation of Large Interconnect Circuits and its Application to PEEC Models with Retardation," IEEE Transactions on Circuits and Systems, vol. 47, no. 4, 2000, pp. 261-273.

[83] A. E. Ruehli, "Circuit Models for Three-dimensional Geometries Including Dielectrics," IEEE Transactions on Microwave Theory and Techniques, vol. 40, no. 7, 1992, pp. 1507-1516.

[84] National Semiconductor Corp., "Partial Element Equivalent Circuit Model Simulation for Designing RF Wireless Communication Products with Embedded Passive Components."

[85] L. He, N. Chang, S. Lin, and O. S. Nakagawa, “An Efficient Inductance Modeling for On-chip Interconnects,” IEEE Custom Integrated Circuits Conference, 1999, pp. 457-460.

[86] J. C. Rautio, “Synthesis of Lumped Models from N-port Scattering Parameter Data,” IEEE Transactions on Microwave Theory and Techniques, vol. 42, no. 3, 1994, pp. 535-537.

[87] M. Kamon, N.Marques, M. Silveria, and J. white, “Generating Reduced Order Models via PEEC for Capturing Skin and Proximity Effects.”

[88] B. Young, ”Wide-band 2N-port S-parameter Extraction from N-port Data,” IEEE Transactions on Microwave Theory and Techniques, vol. 46, no. 9, 1998, pp. 1324-1327.

[89] C. C. Huang, B. Chia, A. Sarfaraz, and M. J. Fox, “Extraction of Accurate Package Models from VNA measurements,” IEEE/CPMT International Electronics Manufacturing Technology Symposium, 2000, pp. 55-59.

[90] P. L. Werner, R. Mittra, and D. H. Werner, “Extraction of SPICE-type Equivalent Circuits of Microwave Components and Discontinuities using the Genetic Algorithm Optimization Technique,” IEEE Transactions on Advanced Packing, vol. 23, no. 1, pp. 55-61.

[91] P. L. Werner, R. Mittra, and D. H. Werner, “Extraction Equivalent Circuits for Microstrip Components and Discontinuities using the Genetic Algorithm,” IEEE Microwave and Guided Wave letters, vol. 8, no. 10, pp. 333-335.

[92] P. L. Werner, and R. Mittra, “A New Technique for the Extraction SPICE-type Equivalent Circuits from Computed S-parameters of Microstrip Components and Discontinuities,” IEEE, 1997, pp. 70-73.